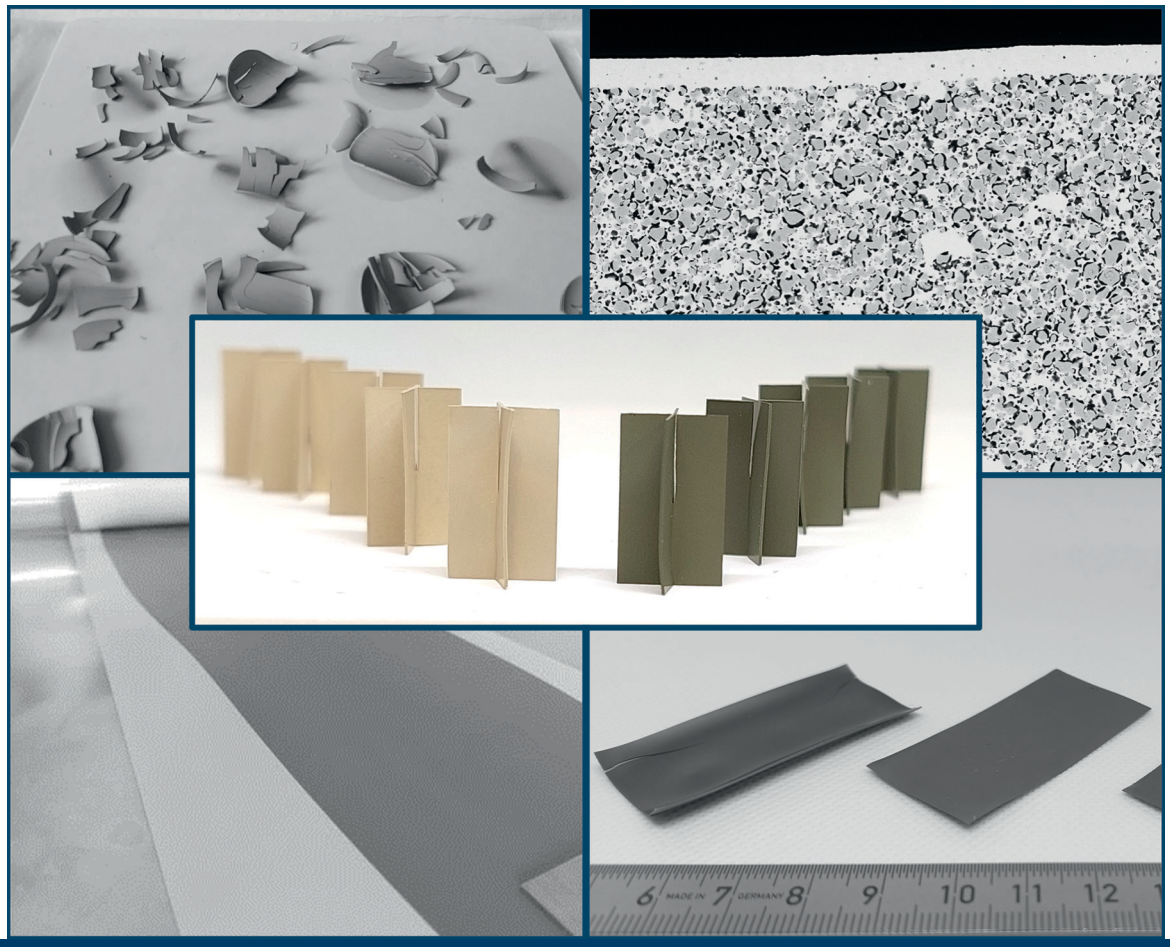

Process Optimization and Scale-Up for $Ba(Zr,Ce,Y)O_{3-\delta}$-Based Proton-Conducting Electrolysis Half-Cells

Laura-Alena Schäfer

Energie & Umwelt / Energy & Environment
Band / Volume 716
ISBN 978-3-95806-941-1

Mitglied der Helmholtz-Gemeinschaft

JÜLICH
Forschungszentrum

Schriften des Forschungszentrums Jülich
Reihe Energie & Umwelt / Energy & Environment Band / Volume 716

Forschungszentrum Jülich GmbH
Institute of Energy Materials and Devices (IMD)
Werkstoffsynthese und Herstellungsverfahren (IMD-2)

Process Optimization and Scale-Up for $Ba(Zr,Ce,Y)O_{3-\delta}$-Based Proton-Conducting Electrolysis Half-Cells

Laura-Alena Schäfer

Schriften des Forschungszentrums Jülich
Reihe Energie & Umwelt / Energy & Environment Band / Volume 716

ISSN 1866-1793 ISBN 978-3-95806-941-1

Bibliografische Information der Deutschen Nationalbibliothek.
Die Deutsche Nationalbibliothek verzeichnet diese Publikation in der
Deutschen Nationalbibliografie; detaillierte Bibliografische Daten
sind im Internet über http://dnb.d-nb.de abrufbar.

Herausgeber und Vertrieb:	Forschungszentrum Jülich GmbH Zentralbibliothek, Verlag 52425 Jülich Tel.: +49 2461 61-5368 Fax: +49 2461 61-6103 zb-publikation@fz-juelich.de www.fz-juelich.de/zb
Umschlaggestaltung:	Grafische Medien, Forschungszentrum Jülich GmbH
Druck:	Grafische Medien, Forschungszentrum Jülich GmbH
Copyright:	Forschungszentrum Jülich 2026

Schriften des Forschungszentrums Jülich
Reihe Energie & Umwelt / Energy & Environment, Band / Volume 716

D 82 (Diss. RWTH Aachen University, 2025)

ISSN 1866-1793
ISBN 978-3-95806-940-4 (Print)
ISBN 978-3-95806-941-1 (E-Book)

Vollständig frei verfügbar über das Publikationsportal des Forschungszentrums Jülich (JuSER)
unter www.fz-juelich.de/zb/openaccess.

i. Abstract

Proton-conducting electrolysis cells (PCECs) are critical to sustainable energy technologies, as they enable the production of undiluted hydrogen that can be readily compressed and stored. These cells are essential for establishing a hydrogen economy. However, their fabrication presents significant challenges compared to more established technologies, such as oxygen ion conducting solid-oxide cells, necessitating advancements in both material and process technologies.

They are more challenging to develop because the material system on which proton-conducting cells are based—solid solutions of Y, Yb-substituted barium cerate and barium zirconate (BZCY)—is chemically more complex than the Y-stabilized ZrO_2 used for oxygen ion conduction. This complexity arises from the less-characterized fundamental properties of these materials, which still pose significant questions regarding basic processing and material behavior. To ensure the PCECs potential is realized, scalable manufacturing processes adapted to this material system are needed to transition laboratory-scale innovations into industrially relevant applications.

This thesis focuses on enhancing robustness, scalability, and reliability in the manufacturing of proton-conducting electrolysis half-cells, based on BZCY-721 electrolytes on a Ni/BZCY-721 cermet as hydrogen electrode and mechanical support. Central objectives include improving the success rate of sintered half-cells, refining the quality of green bodies through optimized slurry composition and tape casting, mitigating warpage, and gaining a deeper understanding of material sintering behavior. Several challenges were addressed, such as batch-to-batch variations in powder properties, the destabilizing effects of methyl ethyl ketone (MEK) as a solvent, and the refractory nature of Zr-rich BZCY materials. Tailored solutions were implemented to achieve dense, flat, and crack-free half-cells (sizes ranging between d = 20 mm and 2.5 × 5 cm^2) along with optimized sintering setups to improve layer density and structural integrity.

Significant achievements were made during this work. At the outset, the fabrication process yielded no usable cells, with issues such as warpage, cracking, and insufficient density. By the end of the research, green body defects were reduced to approximately 10 % through improvements in slurry preparation, tape casting, and cutting techniques. Post-sintering success rates increased up to 80 %. Additionally, a deeper understanding of the sintering behavior of individual layers provided insights into mismatches between hydrogen electrodes and electrolytes, as well as heating rate-dependent sintering mechanisms. These findings facilitated the mitigation of warpage which then eliminated the need for post-sintering flattening or laser cutting steps.

The scalable methods developed in this thesis enable the production of reproducible cells, which are essential for systematic investigations into material dependencies and performance characteristics. This reproducibility supports crucial research into degradation mechanisms, long-term stability, and full-stack testing, advancing the practical application of proton-conducting electrolysis cells. Furthermore, shrinkage rate measurements revealed a complex chain of sintering mechanisms, likely contributing to the limited processability of these cells. Future research should focus on elucidating these mechanisms in greater detail and adapting

sintering schedules accordingly. On the application side, scalable production processes ensure that future studies into performance under various operational atmospheres and the optimization of steam electrode materials can be conducted with consistent and comparable cell quality.

A noteworthy aspect of this thesis is the conscious decision to document failed experiments. This approach provides valuable insights for future researchers, helping to avoid similar pitfalls and refine their processes. By addressing both fundamental material challenges and practical production issues, this thesis represents a significant step forward in the development of scalable and robust production methods for proton-conducting electrolysis cells, bringing the field closer to integration into real-world energy systems.

ii. Kurzfassung

Protonenleitende Elektrolysezellen (PCECs) spielen eine Schlüsselrolle in nachhaltigen Energietechnologien, da sie die Produktion von reinem Wasserstoff ermöglichen, der sich ohne weiteren Aufbereitungsschritt komprimieren und speichern lässt. Diese Zellen sind essenziell für die Etablierung einer erfolgreichen Wasserstoffwirtschaft. Ihre Herstellung stellt jedoch im Vergleich zu etablierten Technologien wie Sauerstoffionenleitenden Festoxidelektrolysezellen (SOECs) größere Herausforderungen dar, da sowohl Material- als auch Verfahrenstechnologien weiterentwickelt werden müssen.

Die Materialsysteme protonenleitender Zellen, basierend auf Y/Yb-substituierten Bariumceraten und Bariumzirconaten (BZCY), sind chemisch komplexer als Y-stabilisiertes Zirkoniumdioxid (YSZ), das für Sauerstoffionenleitung verwendet wird. Diese Komplexität ergibt sich aus den weniger gut charakterisierten grundlegenden Eigenschaften dieser Materialien, die weiterhin Fragen zu Prozessen und Materialverhalten aufwerfen. Um das Potenzial von PCECs auszuschöpfen, müssen skalierbare Herstellungsverfahren für den Übergang von Laborentwicklungen zu industriell relevanten Anwendungen angepasst werden.

Die Dissertation konzentriert sich auf die Verbesserung von Prozessrobustheit, Skalierbarkeit und Zuverlässigkeit bei der Herstellung von protonenleitenden Elektrolyse-Halbzellen. Diese basieren auf BZCY-721-Elektrolyten und einem Ni/BZCY-721-Cermet als Wasserstoffelektrode und mechanische Stütze. Ziel ist es, die Erfolgsrate gesinterter Halbzellen zu erhöhen, die Qualität der Grünlinge durch optimierte Schlicker-Zusammensetzungen und Foliengussverfahren zu verbessern, Krümmung zu minimieren und ein besseres Verständnis des Sinterverhaltens zu gewinnen. Am Anfang der Forschung führten Herstellungsprozesse zu unbrauchbaren Zellen mit Problemen wie Verformung, Rissen und geringer Dichte. Durch Verbesserungen in der Schlicker-Vorbereitung, dem Folienguss und den Schnitttechniken konnten Grünling-Defekte auf ca. 10 % reduziert werden. Nach dem Sintern stieg die Erfolgsrate auf bis zu 80 %. Vertiefte Untersuchungen des Sinterverhaltens lieferten Erkenntnisse über das Sinterverhalten von Elektroden und Elektrolyten sowie deren Mechanismen, wodurch Verformungen verringert und Nachbearbeitungsschritte eliminiert wurden.

Die entwickelten skalierbaren Methoden ermöglichen reproduzierbare Zellen, die systematische Untersuchungen zu Materialabhängigkeiten und Leistungseigenschaften unterstützen. Dadurch werden wichtige Forschungen zu Degradationsmechanismen, Langzeitstabilität und Stacktests gefördert. Zukünftige Studien sollten den Fokus auf Sintermechanismen und die Optimierung von Elektrodenmaterialien legen. Eine bewusste Dokumentation von Fehlversuchen liefert zukünftigen Forschern wertvolle Einblicke, um ähnliche Fehler zu vermeiden. Mit der Lösung grundlegender Material- und Produktionsprobleme markiert diese Arbeit einen signifikanten Schritt hin zu skalierbaren und robusten Produktionsmethoden für PCECs und deren Integration in reale Energiesysteme.

iii. Contents

iv. List of Abbreviations

ABO_3	Perovskite Crystal Structure
BCY	$BaCe_{1-x}Y_{1-x}O_{3-\delta}$
BZCY-622	$Ba_{1.015}Zr_{0.625}Ce_{0.2}Y_{0.175}O_{3-\delta}$
BZCY-721	$BaZr_{0.7}Ce_{0.2}Y_{0.1}O_{3-\delta}$
BZCYYb-4411	$BaZr_{0.4}Ce_{0.4}Y_{0.1}Yb_{0.1}O_{3-\delta}$
BZY	$BaZr_{1-x}Y_{1-x}O_{3-\delta}$
BZY20	$BaZr_{0.8}Y_{0.2}O_{3-\delta}$
El	Electrolyte Layer
HE	Hydrogen Electrode
HER	Hydrogen Evolution Reaction
IMD-2	Institute of Energy Materials and Devices-2
MEK	Methyl Ethyl Ketone
OER	Oxygen Evolution Reaction
OFW	Ozawa-Flynn-Wall Method
PCC	Proton-Conducting Cell
PCEC/PCFC	Proton-Conducting Electrolysis/Fuel Cell
PEM	Proton Exchange Membrane
PSD	Particle Size Distribution
SE	Steam Electrode
SEM	Scanning Electron Microscopy
SMR	Steam Methane Reforming
SOC	Solid Oxide Cell
SOEC/SOFC	Solid Oxide Electrolysis/Fuel Cell
SSR(S)	Solid State Reaction/Reactive (Sintering)
Su	Hydrogen Electrode - Support Layer
TEM	Transmission Electron Microscopy
TRL	Technological Readiness Level
XRD	X-Ray Diffraction
YSZ	Yttrium stabilized Zirconia

1 Introduction and Motivation

Our society needs to reach a point where it is both economical and technologically feasible to produce and utilize green hydrogen across various settings, such as chemical energy storage or as fuel for maritime, aeronautical, and ground vehicles. Among the options available, proton-conducting electrolysis cells emerge as promising candidates. The demand for advanced energy technologies necessitates the development of Proton-Conducting Electrolysis Cells (PCECs) due to their potential for efficient and environmentally friendly energy conversion and storage. [1] However, their current Technological Readiness Level (TRL) is low, indicating a need for significant advancements in their manufacturing processes, especially in scaling up preparation procedures. [2]

Drawing from the rich experience gained in oxygen ion conducting Solid Oxide Cell (SOC) research, there is great potential for transferring knowledge and methodologies to PCEC development. Despite this potential, challenges persist in material and cell preparation due to the nature of the involved materials, demanding precise scalable manufacturing processes for quality, reproducibility and reliability. Issues like barium volatility during sintering and high sintering temperatures pose significant hurdles > 1600 °C. [3]

Recent efforts have shown promise in producing PCECs on a larger scale through scalable manufacturing methods. [4,5] However, these methods have not yet been fully upscaled for (near)-industrial production, which is essential for practical applications and commercialization. Currently, the number of measurable samples remains a small fraction of the total produced, underscoring the need for more efficient and reproducible manufacturing procedures.

To enable comprehensive cell investigations and ensure reliable performance data, it is crucial to produce comparable samples. This comparability is essential for long-term testing, degradation studies, and performance evaluations under varying atmospheric conditions. The primary objective of this thesis is to develop and detail the procedures necessary to scale up the preparation of PCEC half-cells, both in terms of sample size and quantity. Achieving TRLs sufficient for large-scale PCEC production requires solving several problems, with warpage during sintering identified as a significant challenge. [4,5] Therefore, this thesis will place particular focus on mitigating warpage and analyzing sintering behavior to enhance cell quality.

The overarching goal of this thesis is to lay the groundwork for future developments aimed at increasing the production yield of PCEC samples. The target is a hydrogen electrode-supported half-cell design, for which the initial process closely follows the work done at the IMD-2 within the ProtoMem project. [6] In this project, a process was developed for a BZCY-based half-cell of slightly different stoichiometry and refined, focusing on performance optimization of cells with a diameter of around 20 mm, which was showed promise for some larger cells up to 10 × 10 cm².

This thesis includes:

1. **Theory**: Introducing the theoretical backgrounds that underpin PCEC technology and its manufacturing challenges.

2. **Processing development**: Detailing the advancements in the preparation procedures to enable scalable production, with a strong emphasis on warpage mitigation and sintering behavior analysis.
3. **Conclusion and further steps**: Summarizing the findings and proposing future directions for continued research and development.

By addressing these objectives, this thesis seeks to contribute to the advancement of PCEC technology, facilitating its transition from laboratory-scale research to practical, large-scale applications. The analysis of the literature on PCECs underscores the importance of addressing manufacturing challenges to enable the widespread adoption of this promising energy technology.

The complexity of this work does not lie in discovering or describing new physical phenomena. Instead, it arises from the interdependence of all processing parameters. Compounding this challenge is the fact that the investigated material lacks comprehensive characterization. Initially, there was an underestimation of how already known and optimized processes from standard methods like Y-substituted ZrO_2 (YSZ) and YSZ + NiO could be transferred. The necessary adaptations exceeded expectations.

Chapters are organized according to the manufacturing steps rather than a chronological order of experiments, providing an overview for future researchers working with similar procedures or materials. The main section of this thesis is, therefore, ordered as such: Powder Processing and Pellet Preparation, Slurry Preparation and Tape casting, Lamination and Cutting, Binder Burnout and Sintering. Firstly, the initial process used at the beginning of the PhD work is detailed. Secondly, each process is analyzed with regards to possible upscaling challenges - both upscaling in the sense of larger samples as well as the number of samples produced - and reliability with regards to repeatability and reproducibility of the process. The next section addresses the various steps undertaken to mediate problems and optimize the process. Each section ends with the description of the final procedure, including further optimization potential.

2 Theoretical Background and State-of-the-Art

This chapter explores the theoretical background related to green hydrogen generation methods that are both environmentally friendly and cost-effective. A key focus is on Proton-Conducting Electrochemical Cells (PCECs), which show great promise for efficient energy conversion. The concept of PCECs is introduced, covering material systems and conduction mechanisms. Understanding these basics is crucial for appreciating how PCECs could revolutionize hydrogen production. Additionally, the various preparation technologies used to create PCECs are discussed, highlighting the challenges and advancements in scaling up these processes. A crucial part of this investigation is the study of warpage during the sintering process, which is a common issue in the production of flat ceramics and multilayer assemblies. Understanding and mitigating warpage is essential for ensuring the structural integrity and performance of PCECs. Characterization techniques, important for evaluating the properties of PCECs, are also examined.

By exploring these theoretical aspects, including the phenomena of warpage during sintering, a solid understanding of PCEC technology is built. This foundation is crucial for the subsequent discussions on processing development and future research directions.

2.1 Role of Hydrogen in the Future Energy Landscape

2.1.1 Hydrogen as Energy Carrier of the Future

Climate change related to the use of fossil fuel as primary energy source forces countries worldwide to act and implement strategies for the decarbonization of industries and energy supplies. One major step in the fossil-fuel-free future is the shift towards alternative methods of electricity production such as solar power or wind energy. [7] The disadvantage of these renewable energy sources results from their natural fluctuations in availability based on weather and time of day or year. A complete reliance on these kinds of intermittent energy supplies must be countered by employing strategies to store surplus energy. [8] One method of storing this energy for later use is the method of Power-To-Gas which signifies the conversion of electrical energy to chemical energy in form of gas production. These gases can be pure hydrogen or other hydrogen carriers. [9]

Another component of decarbonization is the greater integration of different energy systems and sector coupling to increase flexibility. This encompasses the heating, electrical energy, and chemical energy supplies. Hydrogen can serve as an energy vector linking different parts of the integrated energy grid of the future. [10] During times of energy surplus, the electrical energy can be used in electrolyzers to produce hydrogen or ammonia, which in turn can be transformed later e.g., to co-generate electricity and heat for private households by using fuel cells. [7]

The third component of the full decarbonization requires a complete transformation of all applications that use fossil fuels as a source of energy. This includes e.g., the steel, ceramics and glass industry, chemical plants as well as the transportation sector (automotive, maritime and aviation). Depending on the use case, the hydrogen needs to be of higher or lesser purity or highly compressed (e.g., chemical production plants or mobility). [11] The switch to an energy system largely using hydrogen is planned to take place until 2050. [12]

Hydrogen's role in the global decarbonization will change over the years to come. At the moment, the most immediate effect of the switch from fossil fuels to hydrogen will be seen in the reduction of emitted greenhouse gases. The true potential of hydrogen, however, will only manifest when the hydrogen used is made from renewable energies, the so called "green" H_2. [7] Figure 2-1 pictures the amount of CO_2 equivalent gases per kWh H_2 associated with each hydrogen generation method.

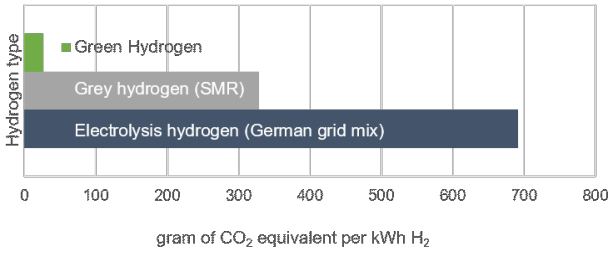

Figure 2-1: Amount of CO_2 equivalent gasses needed for the production of 1 kWh worth of H_2 using different methods (SMR: Steam Methane Reforming). [7]

2.1.2 Diversification in Hydrogen Production Technologies

Crucial for the success of the hydrogen strategy is to make the green hydrogen production more economical. In this regard, electrolyzers must be seen not only on a cell or stack level but also include the periphery ("balance-of-plant") adding to the costs of the complete system. To lower the investment costs for the high-temperature electrolyzer, it is beneficial to have lower operating temperatures. These allow the use of cheaper and more conventional construction materials e.g., stack housing or piping made from conventional steel. [10] Two additional cost factors are, firstly, the required compressors to increase the gas pressure for storage or transport. [8] Secondly, depending on the chosen type of electrolyzers the produced hydrogen gas is either pure or diluted with reactants or byproducts. This leads to the need of an additional gas separation step. [13]

For a greater range of applications, there are many different production routes to generate hydrogen. These methods differ not only in their operating conditions but also in the resulting hydrogen quality, such as water content, impurities, or pressure. Likewise, hydrogen consumers require different hydrogen qualities depending on the respective application and operating conditions. For example, hydrogen used to fuel cars needs to be compressed to 350-700 bar and of high purity (99.97 %) because the limited storage capacity inside a vehicle and the requirements for PEM-fuel cells (PEM: Proton Exchange Membrane). [14] On the other hand, there are industrial processes that can use hydrogen instead of the currently used fossil fuels. Industrial processes creating large amounts of waste heat can be coupled with electrolyzers that require a high temperature to operate thereby saving additional energy. [13] Therefore many technologies working at different operating conditions might be viable by making use of synergies or coupling of electrolysis and other processes.

Finally, there is the question of scalability. If the number of produced electrolyzers increases in the predicted and hoped for way, technologies that profit from scalability effects will become dominant. One example here is the production of multi-layer electrochemical cells that can be produced by tape casting, a scalable and highly integrated manufacturing technology.

2.1.3 Electrochemical Cells for Water Electrolysis

One major group of processes use electrochemical cells to split water/steam into hydrogen and oxygen and then an external power source "pumps" either the oxygen or hydrogen ions to the other side of an electrolyte separating the two species. The three major types are shown in Figure 2-2.

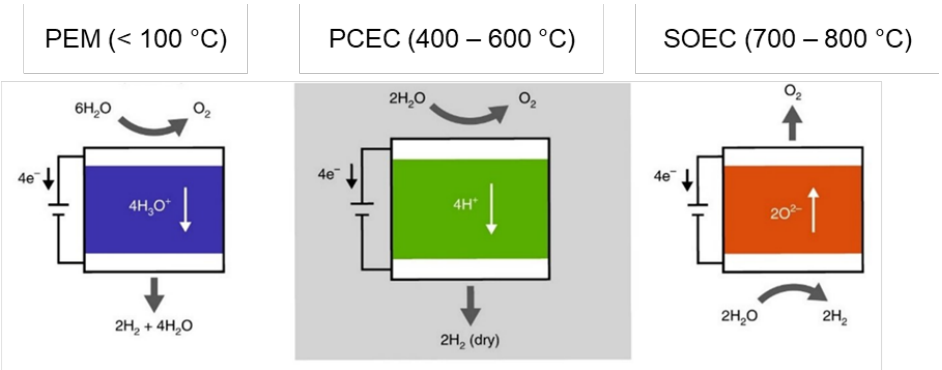

Figure 2-2: Different types of electrochemical cells for steam electrolysis after Vøllestad et al. [13]

The blue diagram depicts a PEM electrolyzer that operates below 100 °C. The orange diagram on the right generalizes the principle of a conventional solid oxide electrolysis cell operating at temperatures between 600 °C and 800 °C. The green diagram shows the newer technology based on proton-conducting ceramic electrolytes operating at intermediately elevated temperatures of 400 °C to 600 °C, which this thesis will focus on. The principle of operation in this case consists of the following, according to the overall reaction in eq. (1): steam supplied to the steam electrode side splits electrochemically to oxygen and protons. The protons migrate through the dense electrolyte layer to the hydrogen electrode side, where the protons combine with electrons to form H_2, which is the desired product. Due to the ambiguity of the terms anode and cathode in fuel and electrolysis operating modes, the naming convention in this work will be the following: The electrode on the steam inlet side will be called steam electrode (SE). This is the cell side where the oxidation reaction takes place, eq. (2). The electrode on the outlet side of the H_2 is called hydrogen electrode (HE) at which the reduction reaction takes place, eq. (3).

$$H_2O \rightarrow H_2 + \frac{1}{2}O_2 \tag{1}$$

Electrode reactions:

SE
$$H_2O \rightarrow 2H^+ + \frac{1}{2}O_2 + 2e^- \tag{2}$$

HE
$$2H^+ + 2e^- \rightarrow H_2 \tag{3}$$

Proton-conducting fuel/electrolysis cells are a type of solid oxide fuel/electrolysis cell and therefore closely related to conventional SOCs regarding set-up and general working principle, see Figure 2-3. The nomenclature of the different SOCs is at times ambiguous. This work will follow the convention of calling proton-conducting electrolysis SOCs PCEC. [15] Both follow the same general setup of two reaction chambers separated by a solid oxide ceramic electrolyte.

The electrolytes used in PCECs are solid proton-conducting oxide ceramics whereas conventional SOCs use oxygen ion-conducting ceramics. From a technology perspective, much of the knowledge regarding e.g., manufacturing methods and material selection criteria can be transferred from conventional SOECs to PCECs.

This seemingly small difference in working principle, as depicted in the figure below, leads to two major advantages for the PCEC. Firstly, the proton travels more readily through the lattice due to its size. This conduction process has a lower activation energy than that of the oxygen ions thus making operations at lower temperatures possible. Lower operating temperatures are generally related to a decrease in degradation mechanisms and allow the usage of more conventional building materials such as conventional steel. [11] Secondly, in contrast to the PEM and SOEC based electrolyzers, the PCEC-generated H_2 is undiluted by any supplied steam, i.e., clean, dry, and ready to compress, thus decreasing the costs of investment.

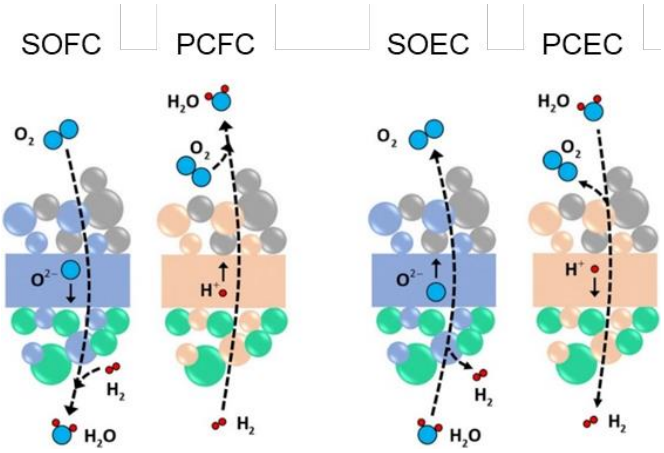

Figure 2-3: Difference between SOFC vs. PCFC and SOEC vs. PCEC. [16]

2.2 Proton-Conduction Mechanisms in Perovskites

The crystal structures that exhibit proton-conduction at the moderate temperatures are often of the perovskite type with general formula ABO_3, e.g., $BaZrO_3$ or $BaCeO_3$. For proton-conduction, the pristine structures are partially substituted with B-site cations. [17] B-site substitution in e.g., $BaZrO_3$ or $BaCeO_3$ with aliovalent elements such as Y or Yb lead to the formation of oxygen vacancies to balance the local charge. As opposed to oxygen vacancies allowing the migration of oxygen through the crystal lattice of oxygen conducting solids, the oxygen vacancies in proton-conducting materials mostly enhance the proton uptake by the material, its so-called hydration ability, thus being directly proportional to its proton concentration and proton conduction.

Literature suggests different mechanisms for the hydrogen transport such as the migration of OH^-. However, the most likely and now accepted mechanism is the Grotthuss mechanism as explained as follows. [18] Atmospheric H_2O dissociates to a H^+ and an OH-group at the surface supported by the catalytic activity of the steam electrode material, i.e., each water molecule produces two protonic defects. Here the protons either transfer both to a lattice oxygen or only one proton goes to a lattice oxygen while the remaining OH-group fills an oxygen vacancy.

This mechanism is the reason the hydration ability is enhanced by the presence of oxygen vacancies. The proton is now associated with a lattice oxygen. The protons move around the oxygen through rotational diffusion. When the proton by chance comes closer to a second oxygen than the first it was associated with, the proton will transfer to the second oxygen. Figure 2-4 shows the path of a proton (red) around its associated oxygen (blue) and the subsequent jump to the next oxygen. [17]

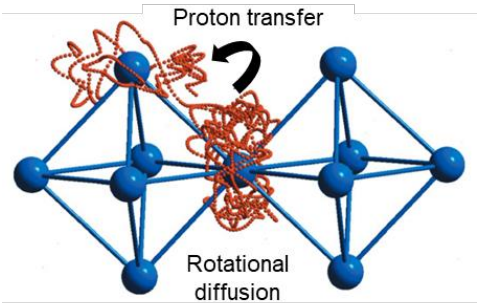

Figure 2-4: Proton transfer model illustrated on a unit cell level, oxygen positions in blue, proton migration path in red after Münch et al. [17,19]

The choice of A-site cation influences the conductivity by changing the distortion of the perovskite structure in a more or less favorable manner. Figure 2-5 shows the difference in the perovskite structures using Ba or Sr as the A-site cation. For both species, the perovskite structure is distorted resulting in two differently susceptible oxygen positions. However, the positioning of these two types of oxygen facilitates the proton transfer from oxygen to another in the $BaCeO_3$ case, because the transfer occurs between two equivalent oxygen ions. In contrast, the $SrCeO_3$ structure requires the proton to be transferred between the two different types of oxygens as pictured in Figure 2-5. [17,20]

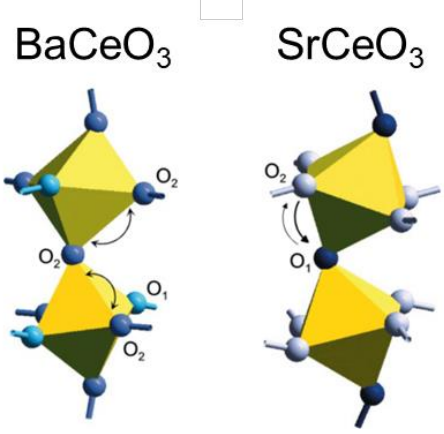

Figure 2-5: Path of protons along associated oxygen atoms for two cerates, O1 and O2 referring to two different types of oxygen positions in the structure after Münch et al. [17,20]

The proton conduction in the electrodes follows the same principles as very often the electrolyte material is used in electrodes as well.

2.3 Defect Chemical Background of an Operating PCEC

During operation of the PCEC, the materials come into contact with different atmospheres as depicted in Figure 2-3. At the most basic level, one can distinguish between electrolyte and electrode reactions. On the one hand, the electrolyte reactions are mostly related to proton lattice diffusion as well as interface diffusion at the grain boundaries. On the other hand, the electrode reactions include additionally to the above-mentioned diffusional mechanisms also charge transfer at the electrolyte-electrode and electrolyte-electrode-environment interfaces.

$$\sigma = z\,F\,c_{H+}\mu_{H+} \tag{4}$$

In all these reactions, bulk proton conduction of the material expressed by eq. (4) (where z is the elementary charge, F the Faraday constant, c_{H+} and μ_{H+} are the proton concentration and mobility, respectively) plays an important role. It is therefore particularly important to have a formalism to coherently describe the reactions using the Kröger-Vink-nomenclature.

The first relevant defect equation (eq. (5)) describes the mechanism of proton uptake and the following formation of a protonic defect $OH_O^{\bullet}$, hence directly related to proton concentration c_{H+} from the formula above. Here, gaseous $H_2O_{(g)}$ at the steam side in the PCEC schematic of Figure 2-3, reacts with a lattice oxygen O_O^x and an oxygen vacancy $V_O^{\bullet\bullet}$ to form two protonic defects. This is called material hydration by an acid-base reaction. [21,22]

$$H_2O_{(g)} + O_O^x + V_O^{\bullet\bullet} \leftrightharpoons 2OH_O^{\bullet} \tag{5}$$

For materials with a low redox activity this is supposedly the only way of taking up protons. [23] The second mechanism is called hydrogenation. In the form as described in eq. (6), the process does not require oxygen vacancies. This uptake of a proton by a lattice oxygen through redox-reaction takes place in humid oxidizing environments. This process only occurs in materials that are redox active. [24]

$$H_2O_{(g)} + 2O_O^x + 2h^{\bullet} \leftrightharpoons 2OH_O^{\bullet} + \frac{1}{2}O_2 \tag{6}$$

However, this equation is the combination of the following eq. (7), describing the reaction of oxygen uptake in oxidizing environments and eq. (5) for proton uptake in humid atmospheres.

$$\frac{1}{2}O_{2(g)} + V_O^{\bullet\bullet} \leftrightharpoons O_O^x + 2h^{\bullet} \tag{7}$$

In dry oxidizing environments, oxygen vacancies are filled by atmospheric O_2 (eq. (7)). [21,24] An alternative way of writing this equation is to use the symbol $O_O^{\bullet}$ to refer to a hole $h^{\bullet}$ that is associated with an oxygen atom [22,25]

$$\frac{1}{2}O_{2(g)} + O_O^x + V_O^{\bullet\bullet} \leftrightharpoons 2O_O^{\bullet} \tag{8}$$

An important equation (9) for the uptake of water on the steam electrode side is called Oxygen Evolution Reaction (OER) [22] Here the formation of protonic defects creates two electrons.

$$H_2O + 2O_O^x \leftrightharpoons \frac{1}{2}O_2 + 2OH_O^{\bullet} + 2e' \tag{9}$$

These electrons cannot migrate through the electrolyte, so they are forced to circumvent the non-conductive electrolyte to reunite on the steam electrode side to form gaseous hydrogen (Figure 2-2:, green diagram). To describe this Hydrogen Evolution Reaction (HER) at the hydrogen electrode side, eq. (10) is used. [22]

$$OH_O^{\bullet} + e' \leftrightharpoons \frac{1}{2}H_2 + O_O^X \tag{10}$$

Finally, in defect chemistry the balance of charge is very important. The dopant concentration is theoretically closely related to the protonic defect concentration. The electroneutrality condition is given by eq. (11) $[Acc']$ is the acceptor dopant concentration, which as negative charge amounts to the sum of all positive charge carriers counteracting its charge. [23]

$$[Acc'] = [V_O^{\bullet\bullet}] + [2OH_O^{\bullet}] + [h^{\bullet}] \tag{11}$$

2.4 Cell Geometry and Material Requirements

The simplest architecture of a proton-conducting ceramic cell consists of three layers: two porous mixed conducting electrodes on either side of a dense, gas and electron tight proton-conducting electrolyte. This assembly must be chemically and mechanically compatible during processing as well as during operation.

PCECs of both tubular and planar cell designs have been evaluated in literature. Duan et al. showed successfully the production of reversible proton-conducting button cells with an active electrode area size between 0.5 and 0.65 cm^2. [26] Vøllestad et al. demonstrated a tubular cell design based on $BaZr_{0.7}Ce_{0.2}Y_{0.1}O_{2.95}$ electrolyte (BZCY721) with a Ni/BZCY-721 cermet as hydrogen electrode and a $Ba_{1-x}Gd_{0.8}La_{0.2+x}Co_2O_{6-\delta}$ steam electrode. Their set-up is shown in Figure 2-6 on the left. [13]

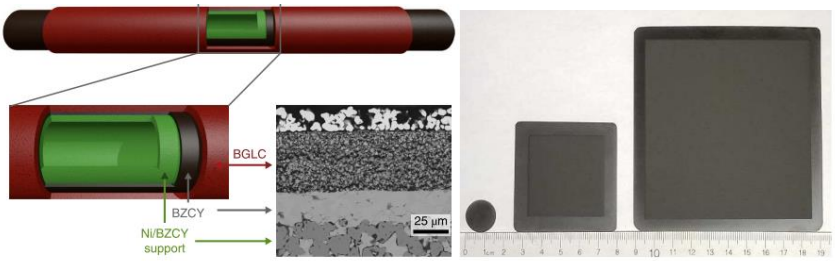

Figure 2-6: Example for tubular PCEC and the scale-up of planar PCFCs. [13,27]

This work will focus on the planar design for different reasons. Firstly, the literature shows a trend away from tubular structures towards planar geometries because of the better manufacturability and easier stack integration. [28] Secondly, Hino et al. found that in direct comparison their planar cells outperformed their cells with tubular design due to the better distribution of gas. [29] Thirdly, the planar design is more suitable for load changes. [30] Additionally, there is a large amount of expertise at the IMD-2 regarding the larger scale production of planar conventional SOCs which could potentially be transferred to PCEC manufacturing. [4,31–33]

2.4.1 Electrolyte Materials

Current research is predominantly based on electrolytes derived from $BaZrO_3$-$BaCeO_3$ (BZ-BC) based solid solutions. These oxide compositions exhibit proton conductivity at moderate to intermediate temperatures, e.g., 400 - 700 °C. Both end members of the $BaZrO_3$-$BaCeO_3$ system have specific problems that impede on their usability as electrolyte materials. $BaZrO_3$ is a compound that requires high sintering temperatures > 1600 °C to achieve a sufficient degree of densification. [3] This does not only increase the energy costs of the sintering step but also limits the choice of suitable electrode materials that are able to withstand these elevated temperatures if one co-sintering step is desired. The microstructure of $BaZrO_3$ has other major disadvantages namely relatively small grains (≤ 1-2 µm) and high resistance of its grain boundaries due to the formation of space charge zones with depletion of protons. [34]

$BaCeO_3$ on the other hand is also not suitable for the use in PCEC/PCFC. The composition exhibits a low degree of chemical stability in H_2O and CO_2 rich atmospheres. [35] Furthermore, the valence change of cerium Ce^{4+}/Ce^{3+} could contribute to the so-called electronic leakage which lowers the efficiency of the system. [22] This allows the electrons to be partially conducted through the electrolyte and not the outer power source. In addition, the valence change can also be accompanied by chemical expansion of the material. [36]

As addressed in the section on defect chemistry, substitution is used to improve the proton-conductivity. A common substitution of the B-site cation is yttrium and/or ytterbium. Trivalent yttrium substitution is charge balanced by the formation of oxygen vacancies, ($V_O^{\bullet\bullet}$). Eq. 12 describes the Zr substitution by Y in e.g., ZrO_2:

$$2Zr_{Zr}^{x} + O_O^{x} + Y_2O_3 \rightarrow 2Y'_{Zr} + V_o^{\bullet\bullet} + 2ZrO_2 \qquad (12)$$

Ytterbium substitution has the same effect while at the same time stabilizing the composition against deactivation by carbon buildup (in CO_2-containing atmospheres) and sulfur contamination. [37]

In conclusion, although both $BaZr_{1-x}M_xO_{3-\delta}$ and $BaCe_{1-x}M_xO_{3-\delta}$ (M = Y,Yb) show proton conductivity, the combination of the two into $BaZr_{1-x}(Ce,M)_xO_{3-\delta}$ offers the best compromise between proton conduction and chemical stability. [17] Duan et al. showed that in direct comparison $BaZr_{0.4}Ce_{0.4}Y_{0.1}Yb_{0.1}O_{3-\delta}$ outperformed BZY20 regarding maximum current density, Faradaic efficiency, and hydrogen production rate. Choi et al. showed that BZCYYb-4411 is a suitable compromise between cerate and zirconate properties. [26,38]

Processing this material by using standard sintering routes poses several issues including inhomogeneous phase formation. [39] Another important challenge is the evaporation of constituents. Barium tends to evaporate from the material at high temperatures leaving behind a barium deficient structure that is less conductive. In addition, evaporation of only part of the composition leads to a change in the A-to-B ratio. Figure 2-7 depicts the microstructure dependent on the A-to-B ratio. Figure a) with a slight under stoichiometry shows large pores whereas the microstructure of the specimen with higher A-to-B ratios exhibit less porosity but supports the emergence of stacking faults. [40]

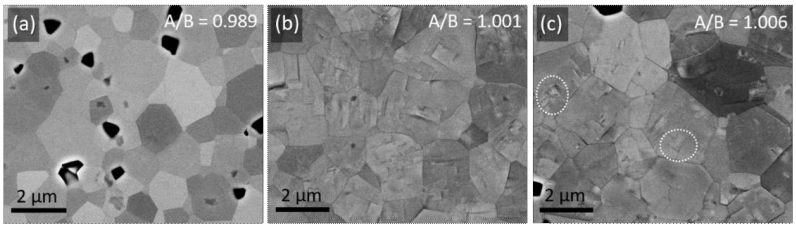

Figure 2-7: Microstructure changes depending on the A:B ratio. [40]

To counteract the barium evaporation, sacrificial powder is used during the sintering step or 3 - 4 mol.-% Ba overstoichiometry is introduced in the nominal composition. [41] It was shown that the addition of cerium to the $BaZrO_3$ composition can improve sinterability as well as conductivity at low amounts. [17] The effect of sinterability in the system BZY - BZCY - BCY was looked at closer by Li et al. [42] Apart from the high sintering temperature, another problem with sintering BZY is that the usual methods of sintering aid influence the electrical properties. Addition of NiO or CoO have been shown to contribute to electronic leakage. [43,44] However there are alternatives like reactive sintering where part of the driving force for sintering is provided through the components tendency to form a solid solution. [45]

Two compositions are studied within this thesis: $BaZr_{0.7}Ce_{0.2}Y_{0.1}O_{3-\delta}$ (with and without the addition of NiO as a sintering aid) and $BaZr_{0.4}Ce_{0.4}Y_{0.1}Yb_{0.1}O_{3-\delta}$ (BZCY-721 and BZCYYb-4411 respectively). Previous work at the IMD-2 has been conducted on the composition $Ba_{1.015}Zr_{0.625}Ce_{0.2}Y_{0.175}O_{3-\delta}$. Some comparative experiments are performed using that composition.

2.4.2 Hydrogen Electrode Materials

Since the operating temperature is relatively low compared to the conventional SOEC technology, it is essential to minimize ohmic resistance to the transport of protons through the electrolyte. [46] This is achieved by choosing a hydrogen electrode supported design with a minimally thin but at the same time defect free and gas tight electrolyte. This means that the hydrogen electrode material also functions as the mechanical support layer for the entire cell. [47] This layer requires a percolating network for electrons and hydrogen gas to ensure functionality. At the electrolyte interface, the material needs to also be proton-conducting to increase the number of triple phase boundary points where electrons and protons can react to gaseous H_2. These requirements are met by mixing an electronically conductive metal with the electrolyte material. The major part of the porosity results from the reduction of the metal oxide to the metal. [5]

The hydrogen electrode material is in general a combination of Ni(O) and the electrolyte material. This is due to the best performance and cost efficiency of Ni based catalysts in H_2 evolution reaction (HER) and long year experiences from the SOCs research. The reduced Ni and the electrolyte material form together a cermet composite which is then a porous, dual-phase mixed electronic-ionic conductor. At the triple phase boundaries between the electron-conducting metallic nickel-phase, the proton-conducting electrolyte material and the pore with the gas phase, two protonic defects release their protons under the consumption of the electrons and gaseous H_2 is formed (see eq. (10)). [22]

In SOECs, Ni-cermet hydrogen electrodes come into contact with H_2O which causes partial reoxidation of the nickel and a degradation of the electrode as a whole. However, Ni-cermets in PCECs avoid this degradation mechanism due to the fact that the hydrogen electrode is not exposed to oxidizing environments. [48]

Wrubel et al. found that the hydrogen concentration at the hydrogen electrode can have a significant effect on the Faradaic efficiency. H_2 buildup contributes to the electronic leakage due to the reduction of cerium. [22] Therefore it is desired to design the hydrogen electrode such that the removal of H_2 is enhanced.

The mechanical support for the entire cell will be based (as with conventional fuel electrode supported SOCs) on the nickel-electrolyte material dual phase. In this work, functional hydrogen electrode layer and the mechanical support will not be different regarding their composition.

2.4.3 Steam Electrode Materials

Compared to the hydrogen electrode material selection, the steam electrode material has more choices. The material needs to be at least catalytic to the dissociation of the H_2O molecules. It also must be ensured that protons can diffuse as protonic defects towards and through the electrolyte. Also, the pores must form a percolating network to ensure the transport of H_2O to the points of reactions and O_2 away from them.

$PrBa_{0.8}Ca_{0.2}Co_2O_{5+\delta}$ was chosen by Zhou et al. as a steam electrode to use the precipitation of $BaCoO_{3-\delta}$ on the surface of the PBCC as a point of adsorption and dissociation. [49,50] Choi et al. tested a similar material ($PrBa_{0.5}Sr_{0.5}Co_{1.5}Fe_{0.5}O_{5+\delta}$) as steam electrode for SOEC and found that higher Sr content was detrimental. [51] Therefore Zhou et al. chose to replace the Sr with Ca. [49] Other materials used in the literature thus far are: $BaCo_{0.4}Fe_{0.4}Zr_{0.2}O_{3-\delta}$, $BaLa_{0.5}Co_{0.5}O_{3-\delta}$, $Ba_{0.5}Gd_{0.8}La_{0.7}Co_2O_{6-\delta}$, $Sr_2Fe_{1.5}Mo_{0.5}O_{6-\delta}$. [5,52–54] In this thesis, only the electrolyte and hydrogen electrode will be discussed.

2.5 Ceramic Preparation Process

To achieve the desired properties, the ceramic sample has to be produced initially by following the ceramic process. This process spans the entire production starting with the preparation of a powder of a desired phase, shaping a green body and its consolidation through sintering. The unique characteristic of the ceramic process (from an engineering and economical point of view) is that the quality of each step is heavily influenced by the quality of the process before it. For example: Improper homogenization of the starting chemicals can lead to stoichiometric gradients which in turn can lead to locally different diffusion and sintering kinetics leading to heterogenous microstructures. Differences in the microstructure can cause localized stresses due to a mismatch in coefficients of thermal expansion in the specimen causing it to break during heat-treatment.

2.5.1 Ceramic Powder Processing

To achieve a high-quality cell, attention should be paid first and foremost to the ceramic powder qualities. These are: chemical composition and crystal structure, powder morphology, particle

size distribution and specific powder surface area. Each of these characteristics can be influenced by the production path of the ceramic powder.

The most traditional method of producing ceramic powders of a desired composition is called Solid State Reaction (SSR). In this method, a mix of oxides or carbonates are brought together in the desired stoichiometry and are calcined (heat-treatment below the sintering temperature) to react the starting chemicals to form (ideally) a single-phase powder. Other methods are spray pyrolysis or sol-gel-methods. [55]

It is also an option to form the green body directly using the starting chemicals and to join the phase reaction and consolidation of the body into one heat-treatment step. This so-called Solid-State Reactive Sintering (SSRS) method forgoes the traditional calcination step in powder synthesis. The phase formation and consolidation is combined into one step, thereby saving time and energy in the production process while also improving densification and lowering the sintering temperature. [42,56] As demonstrated by Deibert et al., the partial SSRS process could be successfully integrated with the tape casting technology for PCECs fabrication. [4] Partial refers to the heat-treatment of oxide/carbonate powders at 1100 °C. This leads to the disintegration of $BaCO_3$ but not yet to the formation of BZCY single-phase powder. This work will concentrate on SSR, SSRS and purchased powders.

2.5.2 Shaping

The process of forming a compacted specimen from the prepared powders is called shaping. The goal of the shaping process is a green body of sufficient stability to be handled and high green density to achieve a dense sintered specimen. One can generally distinguish the different shaping processes by the amount of additives added to the ceramic powder. During pressing, no or only small amounts of pressing aids are added while on the other end of the spectrum wet powder spraying consists primarily of the liquid carrier material for the ceramic powder. In the course of this work the following shaping methods for green bodies are used: i) uniaxial pressing, ii) cold isostatic pressing, iii) tape casting, iv) screen-printing, v) lamination and vi) cutting.

The most conventional method is the forming of a green body through pressure. Figure 2-8 shows the three steps of the dry pressing process. [57] First the powder will be filled into a mold. Then the powder will be pushed down and compacted by a die. At the end, the green pellet will be ejected from the die after releasing the pressure.

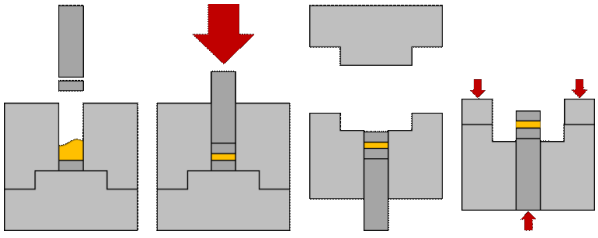

Figure 2-8: Forming of a green body through uniaxial pressing after Marrony et al. [57]

One issue is the inhomogeneous displacement of the powder. Powder towards the die wall is prevented from moving by the wall friction. Figure 2-9 left) shows a diagram with zones of equal density within a green body. These density variations that result from the pressing are

later be present in the sintered body. Green body density is an important factor for achieving a high-density ceramic. [58,59]

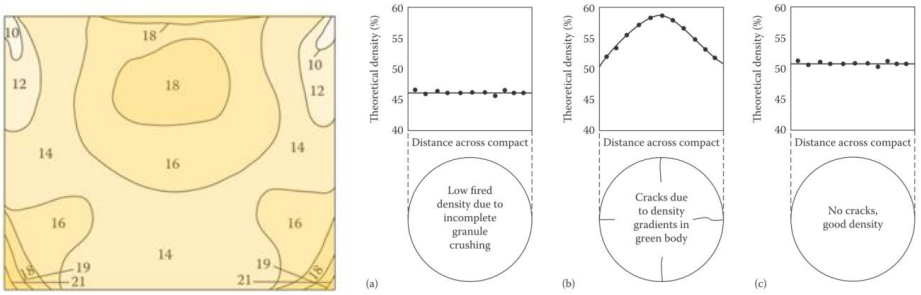

Figure 2-9: left) Density gradients in a pressed green body, right) influence of insufficient green body density on the final density. [59,60]

Figure 2-9 (right) shows the different densities that result from differences of the pressing process. [59,60] In the first picture, it can be seen that the density of the fired pellet is low because the density of the green pellet was insufficient. The second picture shows the effects of an unequally filled pressing dies. The last picture shows the ideal of having good green and final density.

Figure 2-10 shows three distinct types of pressing defects. The laminations are mostly caused by stresses by differential spring-back during the ejection. Ring capping can be also due to excessive spring-back caused by air escaping at the die wall. Both laminations and ring-capping can be reduced by better lubrication. [61]

Figure 2-10: Pressing defects, formation of layers, end capping and ring capping after Reed. [61]

Another method of powder compaction is the use of cold isostatic press. Here, a prepressed pellet or loose powder is filled in a liquid tight bag. Then the bag is submerged in the liquid and the tank is sealed. [59] The liquid in the tank is subjected to an increase in pressure and the liquid isostatically applies pressure to the powder/pellet in the bag. The advantages of this method are the increase in homogenous density.

Another way to produce a green body is the technique of tape casting. Tape casting is a versatile and widely used method for producing thin, flat ceramic components. This technique involves the preparation of a slurry, which is a homogenous mixture of ceramic powders, solvent, a dispersing agent, and an organic binder system. The slurry is then cast onto a carrier tape using a doctor blade, which controls the thickness of the resulting tape. After casting, the tape undergoes a drying process where the solvent evaporates. (See Figure 2-11 a)). Despite the need for sophisticated equipment and techniques, tape casting is suitable for mass production, making it a critical technology in the fabrication of advanced ceramic components. [32]

To apply films of thin or medium thickness onto other substrates or layers, the technique of screen-printing can be used. (See Figure 2-11 b)) Here the substrate is placed below a mesh that is partly covered. When paste is spread over the mesh it will only be transferred to the substrate on the uncovered regions of the mesh. [57]

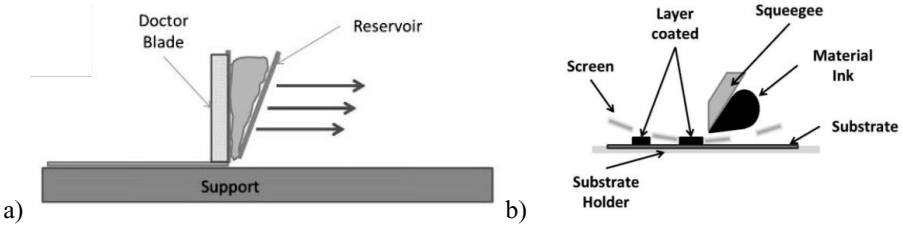

Figure 2-11: a) Basic tape casting set-up and b) the principle of screen-printing. [57]

For both methods, the right formulation of the slurry is critical to achieve. However, both types of slurries (or pastes) differ in the exact components used during the fabrication as the two methods require different viscosity and rheological properties in general. But both mixtures are multicomponent system generally consisting of a solvent, dispersant, binders, plasticizers, (pore former) and ceramic powder. The composition for the tape casting slurry in this thesis originates from the conventional SOCs and was adapted for the BZCY ceramics by Deibert et al. [4,62] Common defects in slurries are powder agglomerates and insufficient viscosities (either too high or too low), and chemical reactivity of the ceramic powder.

Important influences on the quality of the tape casting or the screen-printing process are the conditions during the slurry application. These are namely the relative humidity and the temperature. Machine parameters such as carrier tape speed, squeegee force, filling level of slurry reservoir and screen and substrate conditions can heavily influence the success of the application process. Common defects during tape casting are non-uniform evaporation of solvents leading to a drying skin, sedimentation effects leading to particle size gradients, porosity gradients, or variations in tape thickness. [63] One major parameter determining the successful casting of a slurry is the viscosity.

Lamination is the joining of two layers of one or multiple material tapes through the application of pressure and/or temperature (~ 80 – 90 °C) as pictured in Figure 2-12.

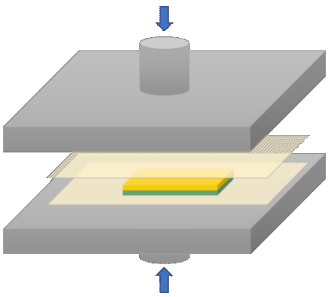

Figure 2-12: Schematic representation of a warm press used for lamination.

The last step in the shaping process for tape cast samples is the cutting of the sample geometry. Blanking, cutting or machining can be performed before or after binder burnout as well as after

sintering. The methods can be broadly separated into contact methods (cutting, punching) as well as non-contact methods (laser cutting).

Punching is done by using a punching tool of specific geometry. The edges of the tool are phased to form a blade edge. Another option is the use of scalpels and knives in conjunction with a ruler. This can be performed manually or by using a machine. Laser cutting can be employed when shaping green samples or sintered samples. In both cases, the formation of NiO-particles is a severe health hazard and is not performed at FZJ anymore. Important parameters of the cutting process are the cutting speed, tool geometry, tool precision, sample composition. Contact cutting tools are affected by abrasion through ceramic particles. Additional components such as binder content can influence the outcome of the cutting process. [64,65] The results of these methods can be very different with regards to cut quality, induced stresses, reproducibility and precision.

2.5.3 Components and Viscosity of Tape Casting Slurries

In its simplest form, a tape casting slurry comprises three fundamental components: ceramic powder, a solvent, and a polymeric binder. However, to optimize the quality and performance of the slurry, additional organic additives are commonly incorporated. [63]

Ceramic powder characteristics: Various ceramic powders have been successfully tape cast into layers. Ideal particle sizes are typically centered around d_{50} = 1 µm. Large agglomerates increase sedimentation risk, potentially causing issues during slurry storage or casting within the reservoir. Another important characteristic is the specific surface area. This characteristic determines how much surface is available to interact with the other slurry components which determines the general slurry behavior. [63]

Solvents: The solvent in tape casting slurries may be water or organic-based, with ethanol and ethanol-methyl ethyl ketone (MEK) mixtures being among the most widely used. These organic solvents are preferred due to their ability to accelerate drying times, although water offers a more environmentally friendly alternative. However, the use of water is often limited due to its slower evaporation rate, which can delay the drying process. [63]

In addition to serving as the primary transport medium for the slurry, the solvent must be compatible with the binder, as inadequate dissolution of the binder can lead to defects in the tape. Although solvents like toluene and dipropylene glycol monomethyl ether were once common, their use has declined recently due to safety concerns. [63]

Dispersing Agents: The primary additive is typically a dispersing agent, which interacts with the ceramic powder surface to prevent agglomeration. By minimizing particle clustering, dispersing agents enhance the homogeneity of the slurry. Consequently, this agent is generally added to the ceramic-solvent mixture as an initial step before introducing other ingredients. [66]

Plasticizers and other additives: Plasticizers may be introduced to enhance the flexibility of the green tape, slow drying rates, improve tape adhesion to the carrier foil, and improve lamination properties. These additives adjust the tape's manufacturability, making it easier to handle and reducing the likelihood of cracking or defects. [63,66]

Viscosity (η) is a measure of a fluid's resistance to deformation under an applied force. [67] It is also dependent on temperature and time. More specifically, it quantifies how a fluid responds to shear stress (σ) and the resulting shear rate ($\dot{\gamma}$):

$$\eta(T, p, t, \dot{\gamma}) = \frac{\sigma}{\dot{\gamma}} \tag{13}$$

In practical terms, high-viscosity fluids resist flow and deformation, while low-viscosity fluids flow easily. In tape casting, the slurry's viscosity determines its performance during different stages such as storage, application, and drying. It is particularly important to account for the varying shear rates encountered during these steps, as the slurry's viscosity changes dynamically based on the forces applied to it.

Under low-shear conditions like storage, the slurry's viscosity determines its resistance to sedimentation. The gravitational force acting on suspended particles creates a sedimentation velocity, described through Stokes Law. [68]

$$v = \frac{2}{9} \cdot \frac{(\rho_\mathrm{p} - \rho_\mathrm{f}) \cdot r^2 \cdot g}{\eta} \tag{14}$$

Where v is the velocity, $\rho_\mathrm{p}$and ρ_F are the densities of the particle and the fluid, respectively, r is the particle radius, g is the gravitational acceleration. From the equation, it is readily visible that the sedimentation speed of any given ceramic powder is dependent on the density as well as the size of the particles. Due to the distribution of particle sizes in any ceramic powder, settling will lead to a particle size gradient when left at rest.

Slurry movement in the tape caster's reservoir occurs under moderate shear rates. Here, it is critical that the viscosity is high enough to prevent particle settling yet low enough to allow smooth pouring and flow. The highest shear rates occur as the slurry is forced through the gap (h) under the doctor blade at a relative velocity (v).

$$\dot{\gamma} = \frac{v}{h} \tag{15}$$

This is where shear-thinning behavior becomes crucial. For optimal flow, the viscosity should decrease with increasing shear rate, allowing the slurry to spread uniformly without clogging or streaking. After the slurry exits the doctor blade, it should spread slightly to smooth out surface irregularities. During the drying stage, the slurry must maintain its structural integrity. This requires a viscosity high enough to resist deformation under gravitational forces. Understanding and controlling the viscosity at these key points is essential for optimizing slurry performance.

2.5.4 Binder Burnout

Binder burnout refers generally to the process of removing organic binders, plasticizers, pore formers, dispersants, and lubricants from a material through heat-treatment before the sintering process. This is typically achieved through direct boiling off, decomposition, or combustion of these organic compounds. [63,66] The effective removal of binders is crucial because it significantly impacts the final properties of the sintered specimen, such as density, porosity, as well as mechanical strength.

The quality of binder burnout is influenced by several critical factors. First, the selection and quantity of the binder play a significant role, as different binders exhibit distinct decomposition behaviors, occurring at specific temperatures and rates. Second, proper preprocessing and homogenization of the powder are essential to ensure uniform binder distribution throughout the material. Lastly, optimizing the heating rates and holding times during the binder burnout process is crucial to achieve complete decomposition of the binder while avoiding the formation of defects such as cracks or pores. [65]

During the removal of organic compounds, the green body loses a significant percentage of its volume and mass. While most of the solvents evaporate during the drying process under ambient conditions, approximately 14 wt.-% of organics (in the case of the tapes of this thesis) must be removed before sintering (after evaporation of volatile solvents). Typically, the mass loss behavior is tracked using a thermogravimetric measuring device, often coupled with differential thermal analysis.

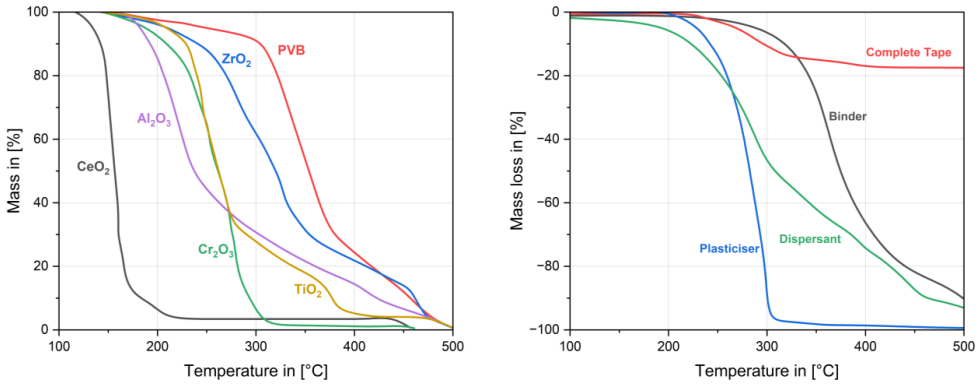

Figure 2-13: Thermogravimetric analysis of binder systems, left) binder (PVB) burnout influenced by the ceramic powder used in the specimen, right) example of organic components and their burnout behavior within SOC tapes and the individual contributions. (After [69,70])

The decomposition behavior of pure PVB differs from that of PVB within a ceramic green tape due to the presence of oxide powders, impacting decomposition in two main ways. Firstly, the flow of decomposition products out of the film is modified. Secondly, the diffusion rate of oxygen into the polymer is altered. The oxides also exert a catalytic effect on binder burnout, while the chemistry of the oxide powder affects the carbon residue formation. [70]

In the literature, it is often assumed that each organic component of the slurry disintegrates at specific temperatures. Figure 2-13 (right) illustrates the mass loss curves of common slurry additives, highlighting the wide range of temperatures at which burnout occurs. The dispersing agent begins disintegrating below 200 °C, while the binder completes its disintegration only at 550 °C. It is assumed that the mass loss of these components in a slurry system is equivalent to a superposition of the components' mass loss behaviors. However, this is not the case. Multiple external parameters influence the process, such as heating rates, oxygen partial pressures, total pressure, furnace ventilation, gas transport in the green body, geometry of the green body, and more. Additionally, the chemical interaction between the organic components and the ceramic powder can significantly influence the burnout temperature. [63] Figure 2-13 left) depicts the

burnout behavior of PVB mixed with various ceramic oxides. The PVB without added ceramic powder experiences the majority of its mass loss starting at approximately 300 °C and finishing before reaching 500 °C. When CeO_2 is used as the ceramic component, burnout finishes at around 200 °C. Notably, the addition of Al_2O_3, SiO_2 or TiO_2 not only modifies the maximum and minimum burnout temperatures but also extends the total range of temperature over which burnout occurs. [69,70]

During the binder burnout, the organic components do not just transform directly from the solid to the gaseous phase. They rather undergo a glass transition forming a decreasingly viscous melt surrounding the powder particles. This leads then to particle rearrangement and an anisotropic shrinkage, namely the tape shrinking more in normal direction than in the tape casting plane direction due to capillary forces as well as constraints due to friction. [71]

During this whole process it is important to note that the tape must remain sufficiently flexible to accommodate the dimensional changes caused by shrinkage during binder burnout without compromising the structural integrity. [72]

2.5.5 Sintering

Sintering is the heat-treatment process during which the green body is consolidated. The most important parameters for this process are heating rate, maximum temperature, and dwell time. However, other parameters can heavily influence the quality of the sintering results: cooling rate, furnace atmosphere, specimen geometry, heat distribution, setter plate and type of furnace. [55]

The sintering process is used primarily for the production of ceramics even though high quality metal products can also be produced through sintering (powder metallurgy). The driving force for the sintering process is the reduction in energy of the green body, related to the high surface area, non-equilibrium phases, inner tensions or applied pressure. One important influence is the particle size as this is related to high surface energies, therefore, sintering can be improved by using finer powders. [73]

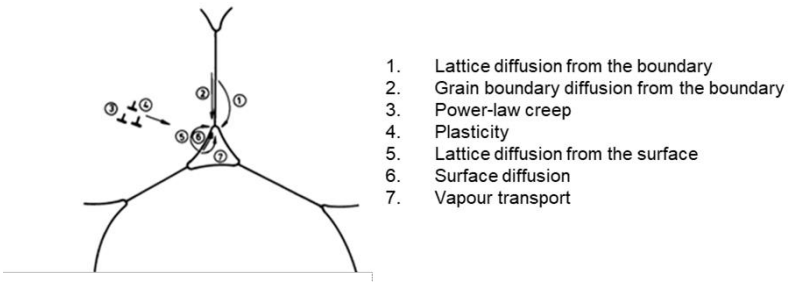

Figure 2-14: Schematic representation of the transport mechanisms of atoms to form and increase the sintering neck. 1 through 4 densify directly, while 5, 6 and 7 only contribute to neck growth after Wilkinson et al. [74]

Several mechanisms are taking place during this temperature stage (detailed in Figure 2-14). [74] Densification involves the elimination of pores, resulting in increased specimen density. Sufficiently small pores which are surrounded by only few grains will shrink to reduce the free energy. However, pores which are surrounded by too many grains may grow

instead. [73] The elimination of these pores is crucial for improving mechanical properties such as strength, hardness, and electrical as well as thermal conductivity. As particles come into contact, they form small bridges or necks between them. These necks grow and strengthen as sintering progresses, eventually binding the particles into a cohesive solid mass.

In the standard theory of sintering, three stages are defined. [55] These stages are experimentally not entirely distinct but the separation serves the theoretical description of the process. The sintering process typically advances through three stages (see Figure 2-15). In the initial stage, loosely packed powder particles are brought into contact. Some neck formation and surface diffusion begin, but densification is limited. During the intermediate stage, particle necks increase in size and particle rearrangement accelerates. Densification becomes more pronounced, and porosity decreases. In the final stage, usually during the isothermal holding period, densification is the primary focus. Porosity further diminishes, allowing the material to achieve its intended properties.

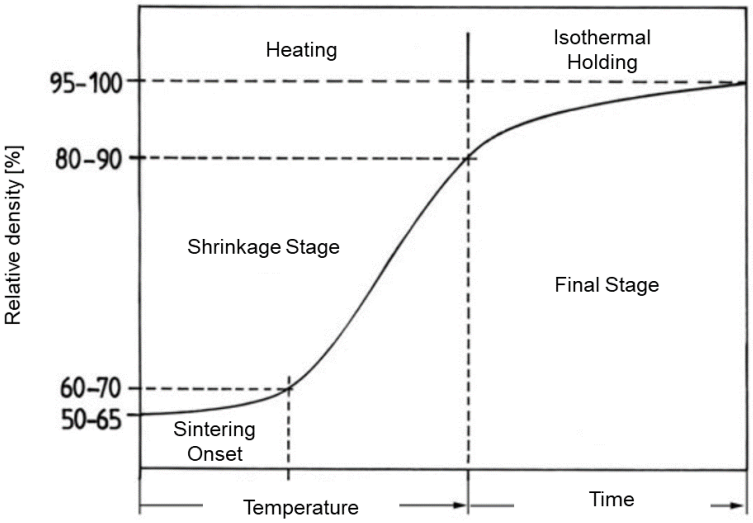

Figure 2-15: Shrinkage curve of a conventionally sintering ceramic body, encompassing initial, intermediate and final stage after Salmang et al. [75]

Sintering can be classified into several types based on the mechanisms and conditions involved. Solid-state sintering involves the consolidation of particles without the presence of a liquid phase. It relies on diffusion and densification mechanisms to achieve a dense, solid structure. In contrast, liquid-phase sintering involves the presence of a transient liquid phase during the process. This liquid phase facilitates particle rearrangement and densification through mechanisms such as dissolution-precipitation (Figure 2-16). The specific phenomena supported by liquid-phase sintering depend on the amount of liquid phase present. With the addition of a small amount of sintering aids (a few vol.-%), the transient liquid phase enhances diffusional transport at the particle surface. As the percentage increases to 20–30 vol.-%, the dominant mechanism transitions to the viscous rearrangement of particles. [73] This type of sintering is often employed for materials that are challenging to sinter through solid-state mechanisms.

Sintering mechanisms in the BZCY (with NiO as sintering aid) ceramic involve several processes that enable densification and formation of a dense ceramic body. Presumably, the key sintering mechanism is the formation of a transient liquid phase BaY_2NiO_5. [76,77] Without sintering aid, sintering temperatures of > 1550 °C are regularly required for full densification of BZCY. [78]

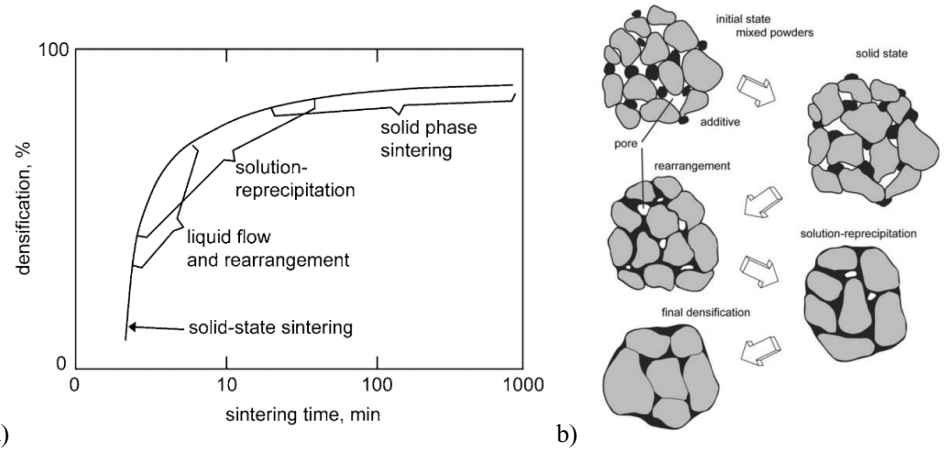

Figure 2-16: Densification behavior during liquid phase sintering: a) densification curve, b) microstructural changes. [79]

One important point remains to address. The so-called constrained sintering occurs when a sintering body cannot shrink freely. [80] The most placative example is a three-layer system in which the middle layer shrinks while the other two do not and thereby restricting the shrinkage of the middle layer. However, constrained sintering effects have to be considered not only in these obvious cases but to some extent in all sintering bodies. [81] For all ceramic bodies, there is an interaction between sample and setter plate as well as gradients within a green body leading to differential densification. These gradients can be the result of the tape casting process (e.g., inhomogeneous evaporation of solvent) or they can be inherent in the green body if two layers are joined to form a single body. Two layers of different materials will regularly have different shrinkage behaviors which lead to internal stresses. These internal stresses can then cause camber and mechanical failure.

Figure 2-17 illustrates the shrinkage behavior of two layers. The top row shows the overall shrinkage of each layer individually: the orange layer exhibits greater shrinkage than the blue layer. In the second row, the orange and blue layers are connected (e.g., after lamination pressing). During sintering, both layers attempt to shrink as they would independently; however, the connection imposes counteracting forces on each layer, affecting their shrinkage behavior.

The orange layer shrinks less than in the unconstrained case, while the blue layer shrinks more. This is due to the additional compressive stresses induced in the blue layer by the densification of the orange layer. The bilayer assembly often tries to alleviate these induced stresses, leading to camber formation in the sample.

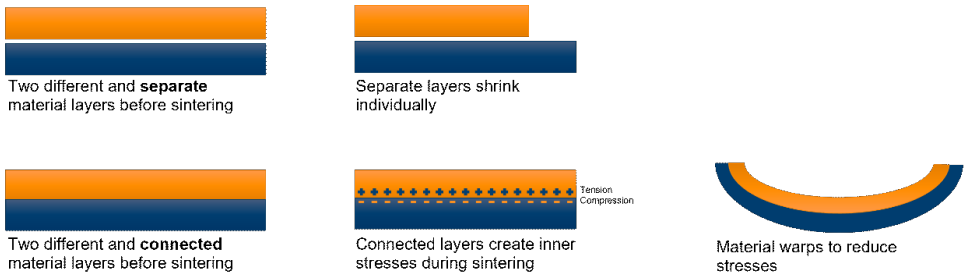

Figure 2-17: Warpage mechanism based on the shrinkage difference in a two-layer system.

These localized shrinkage differences can also be the result of intentional multilayer assemblies. As mentioned earlier, any gradient in green density, chemical composition, stresses, local atmosphere and more can lead to a similar behavior as introduced above. Figure 2-18 shows some common influences on the green body. Analogous to the schematic of the two-layer system above, the first row depicts the shrinkage of the sample if it is not in contact with the setter plate. In row two, the shrinkage of the flat sample is hindered through the friction of the setter plate. This leads to different shrinkage behaviors of the top side and the bottom side. The third row depicts the two major chemical interactions the sample experiences. At the setter plate/sample interface, chemical interaction through diffusion takes place. Many standard refractory setter plates such as Al_2O_3 or MgO react with nickel leading to a loss of nickel in the border region of the sample creating a gradient throughout the specimen. Another possibility is that the sintering process is also influenced by the sintering atmosphere, oxygen partial pressure and evaporation of species. In the case of BZCY, barium evaporation is a well-known problem. [82] The sample surface exposed to the atmosphere will therefore experience a loss of barium which in turn can influence the sintering behavior. This list of shrinkage behavior gradients inside samples is not exhaustive. These gradients are so common and the causes so manifold that they can be treated as the norm, not the exception.

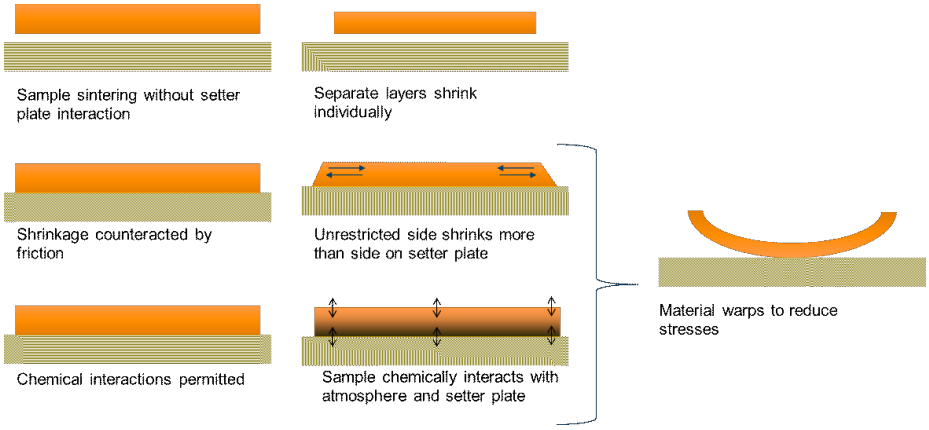

Figure 2-18: Influence of the setter plate on a single layer material during sintering.

If the stresses exceed the sample's ability to accommodate through camber, other defects can occur in the sample. Figure 2-19 depicts several of these defects inside a two-layer sample. Cracking can occur if the fracture toughness of the bottom layer is exceeded through the

warpage. Delamination can be the result of either an insufficiently connected interface or the weakest point for crack propagation to occur.

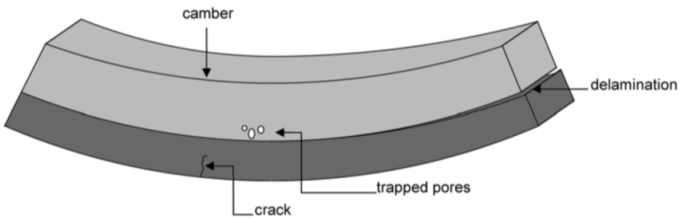

Figure 2-19: Common defects during constrained sintering. [83]

Precise control of temperature and dwell times is essential to avoid issues such as overheating, warping, or inconsistent properties. Sintering can introduce residual stresses in the material, which may need to be addressed through additional treatments or processes.

After sintering, the cooling phase can also be the cause of thermoelastic stresses and defects. This is generally due to a mismatch in coefficients of thermal expansion (CTE). Figure 2-20 depicts the CTEs for a similar BZCY composition. If such mismatches cannot be avoided, the detrimental effects can be mitigated through cooling with very low rates.

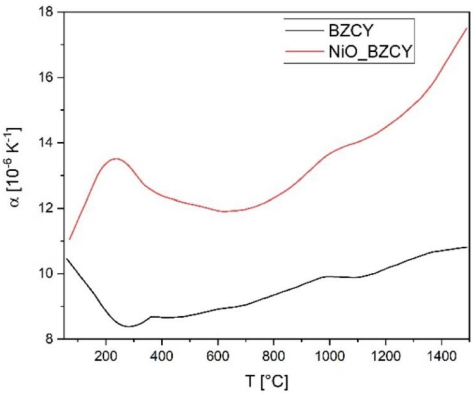

Figure 2-20: Coefficients of thermal expansion for the electrolyte and the hydrogen electrode material NiO/$Ba_{1.015}Zr_{0.625}Ce_{0.2}Y_{0.175}O_{3-\delta}$. [4]

2.5.6 Mathematical Treatment of Shrinkage Measurements

Dilatometry provides crucial insights into the sintering behavior of materials by measuring the dimensional changes (expansion or shrinkage) of a sample as a function of temperature. During these experiments, the initial length of the sample (L_0) is used as a reference to track changes in length (ΔL) over time and temperature. [81] The engineering strain ($\epsilon_{engineering}$) is a commonly used measure for dimensional changes and is calculated as:

$$\epsilon_{engineering} = \frac{\Delta L}{L_0} \tag{16}$$

This simplification assumes that strain is small and the sample dimensions change linearly. However, for sintering processes, particularly in ceramic systems, the total shrinkage often exceeds 10 % of the original length. [81] In such cases, the engineering strain no longer provides an accurate representation of the material behavior due to the significant nonlinearity introduced at higher strains. For larger deformations, the true strain (ϵ_{true}) must be used, which accounts for the continuous and exponential nature of dimensional changes. True strain is calculated as:

$$\epsilon_{true} = ln\left(\frac{L}{L_0}\right) \tag{17}$$

where L represents the instantaneous length of the sample at a given point in time or temperature. This logarithmic relation provides a more precise measure of the deformation, particularly under conditions of large shrinkage during sintering.

In addition to strain, the true strain rate ($\dot{\epsilon}_{true}$) is of particular importance for understanding the kinetics of sintering and related phenomena. It is defined as the time derivative of the true strain:

$$\dot{\epsilon}_{true} = \frac{d\epsilon}{dt} \tag{18}$$

This parameter reflects the rate at which shrinkage occurs, allowing for a dynamic assessment of material densification and deformation during the sintering cycle. When sintering multi-material laminates, differential strain rates between layers are a primary cause of warpage. Warpage occurs when the difference in true strain rate ($\Delta\dot{\epsilon}_{true}$) between adjacent layers deviates from zero:

$$\Delta\dot{\epsilon}_{true} \neq 0 \tag{19}$$

This difference is nearly inevitable due to the distinct thermal expansion and shrinkage behaviors of the materials involved. Such mismatch leads to internal stresses and curvature in the sintered laminate, posing a significant challenge for achieving flat, defect-free components. In real cases, it is most often only relevant that the resulting ceramic bodies are flat after cool down. Therefore, it is also acceptable to have a cell which cambers during sintering but does so in two opposing directions leading to a flat cell at the end of the sintering process. Understanding and quantifying the strain rate mismatch is, therefore, critical for optimizing sintering protocols and material compatibility in multilayer systems.

2.5.7 Calculation of Activation Energy from Dilatometric Measurements

As discussed in the preceding sections, sintering is governed by thermally activated mass transport processes that may occur simultaneously or sequentially during densification. These mechanisms directly give rise to macroscopic shrinkage, which can be accessed experimentally by dilatometric measurements. Consequently, analysis of sintering curves provides a means to extract kinetic parameters of the process, in particular activation energies, and to assess the temperature dependence of the dominant transport phenomena. [84] In this context, activation-energy analysis offers insight into the dominant kinetic contributions, as different transport processes are typically associated with characteristic ranges of activation energy.

In a general sense, an activation energy represents the energetic threshold that must be exceeded for a thermally activated process to occur. For an elementary process with a well-defined mechanism, the temperature dependence of the rate constant $k(T)$ can often be described by an Arrhenius-type relationship:

$$k(T) = A * \exp\left(-\frac{E}{RT}\right) \tag{20}$$

where A is the pre-exponential factor, R is the gas constant and E is the activation energy. A direct determination of the activation energy from this expression would, in principle, require isothermal measurements, since the Arrhenius equation describes the instantaneous rate at a fixed temperature.

In dilatometric sintering experiments, the process is typically conducted under non-isothermal conditions. The macroscopic shrinkage can be treated analogously to the progress of a thermally activated reaction. For this purpose, a degree of conversion, $\alpha(t)$, is the fractional length change defined based on the measured specimen length:

$$\alpha(t) = \frac{L(t) - L(t_S)}{L(t_F) - L(t_S)} \tag{21}$$

where $L(t)$ is the specimen length at time t, t_s denotes the onset of sintering and t_f the end of the sintering step. In this equation, $\alpha = 0$ corresponds to the beginning of shrinkage and $\alpha = 1$ to its completion. In practice, thermal expansion is subtracted from the raw dilatometric signal to isolate the sintering-related shrinkage.

This definition allows the sintering process to be expressed in a generalized kinetic form:

$$\frac{d\alpha}{dt} = k(T) * f(\alpha) \tag{22}$$

where $f(\alpha)$ describes the dependence of the rate of conversion on the extent of conversion and $k(T)$ follows an Arrhenius-type temperature dependence. Substituting the Arrhenius expression yields

$$\frac{d\alpha}{dt} = A * f(\alpha) * \exp\left(-\frac{E}{RT}\right) \tag{23}$$

For experiments conducted at a constant heating rate $\beta = \frac{dT}{dt}$, the time derivative can be transformed into a temperature derivative, leading to

$$\frac{da}{dT} = \frac{A}{\beta} * f(a) * \exp\left(-\frac{E}{RT}\right) \tag{24}$$

Separation of variables results in an integral formulation,

$$\int_0^\alpha \frac{d\alpha}{f(\alpha)} = \frac{A}{\beta} * \int_{T_0}^{T} \exp\left(-\frac{E}{RT}\right) dT \tag{25}$$

The left-hand side of this expression is commonly written as the integral conversion function $G(\alpha)$, while the right-hand side contains the so-called temperature integral of the Arrhenius term. This temperature integral has no closed-form analytical solution. Its appearance is a direct consequence of the non-isothermal nature of the experiment, as the measured shrinkage

depends on the cumulative temperature history rather than on a single isothermal rate constant. [85]

Isoconversional methods exploit the fact that, for a fixed degree of conversion α, the value of $G(\alpha)$ is constant. This allows the temperature dependence of the process to be evaluated without specifying an explicit form of the conversion function f(α). Such approaches are therefore particularly suitable for complex processes in which the underlying transport mechanisms are unknown or may change during the course of sintering.

The Ozawa–Flynn–Wall (OFW) method is an integral isoconversional approach originally developed for the analysis of thermally activated reactions with unknown reaction pathways. [85,86] Using an approximation of the temperature integral proposed by Doyle [87], the OFW method yields a linearized relationship of the form:

$$\ln \beta = \ln\left(\frac{AE}{R}\right) - \ln G\,(\alpha) - 5.3305 + 1.052\,\frac{E}{RT} \tag{26}$$

At a fixed degree of conversion, plotting the logarithm of the heating rate against the reciprocal temperature for experiments performed at different heating rates results in a linear relationship. The slope of this line is proportional to the activation energy, while the intercept contains the pre-exponential factor (see Figure 2-21).

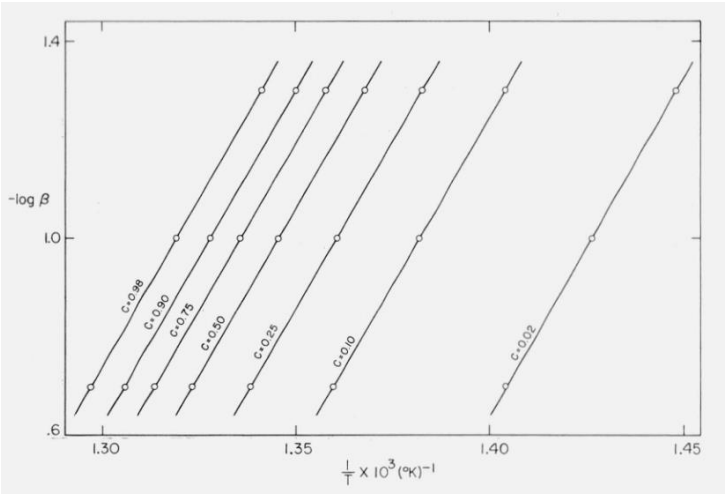

Figure 2-21: Exemplary plot to determine the activation energy for different degrees of conversion $0.02 < c < 0.98$. [85]

Because this procedure evaluates the effective temperature dependence of the overall shrinkage rate at a given stage of transformation, the extracted activation energies do not correspond to a single elementary transport process. Instead, they represent apparent activation energies. Apparent activation energies describe the effective kinetic behavior of the system at a specific degree of conversion and reflect the combined influence of all contributing transport mechanisms at that stage of sintering.

In practical sintering systems, multiple transport mechanisms may act simultaneously or sequentially, and the dominant mechanism may change with temperature, density, or

microstructural state. Consequently, apparent activation energies are expected to vary with conversion. Such variations provide valuable insight into transitions between different kinetic regimes, even though a unique microscopic mechanism cannot be assigned. In this way, isoconversional analysis enables the identification and comparison of sintering stages without imposing restrictive mechanistic assumptions.

3 Methods and Devices

3.1 Characterization Methods

Laser diffraction analysis for measurement of particle size distribution (PSD): The laser diffractometer used was the LA-950V2 Horiba with Mie analysis method due to the expected particle size around 1 µm. Powder samples were dispersed in ethanol, measured, and then dispersed using ultrasound and measured again. The refractive index was needed for the evaluation of the measurement, which was not available for BZCY. A standard value for barium zirconate was used instead (n = 2.6). The result was a histogram depicting volume percentages over sphere diameter. This technique assumes spherical, opaque particles.

Specific surface measurement using the Brunauer-Emmet-Teller-method (BET): This method measures the surface area per gram of powder through the measurement of gas adsorption and desorption of nitrogen (Jung Instruments Areamat). The amount of adsorbed/desorbed gas is proportional to the surface area of the specimen.

Rheology: Viscosity is measured using a rheometer (Modular Compact Rheometer, MCR 301, Anton Paar) with a plate-on-plate (electrode slurry) and a double-gap setup (electrolyte setup). The type of set-up which was used dependent on the amount of available slurry.

X-Ray diffraction analysis (XRD): In this work, two different XRD devices are used. The primary device for XRD measurements, unless otherwise noted, is the D4 Endeavor from Bruker AXS using Cu-Kα-rays at room temperature. The measuring procedure is a grazing beam incident angle measurement performed on powders or sample pieces mounted to adhesive film or polymer clay for qualitative assessments of the phase structure. The second device is the Empyrean from Malvern Panalytical, used for measurements intended for Rietveld analysis to determine quantitative phase composition. The software HighScore Plus from Malvern Panalytical was used for the analysis. The result of this measurement is the intensity of refraction at different angles of incidence, which can be matched to phase structures if the stoichiometry is known.

Scanning electron microscopy (SEM) and Energy-dispersive X-ray spectrometer (EDX): Different SEM devices with various capabilities were used during the course of this work. Unless otherwise mentioned, the standard device is the Hitachi TM3000 tabletop SEM equipped with an EDX sensor using Quantax70 software. Additional images were taken using the Zeiss Gemini 450. Cross-sections were metallographically prepared and sputter-coated with platin.

Transmission electron microscopy (TEM): In collaboration with the Philipps-University Marburg, a few selected samples were prepared and analyzed using TEMs.

Porosity analysis: Porosity analysis is performed using SEM micrographs on polished cross-sections and the threshold method, employing the upper and lower Otsu-splitting method in the software Dragonfly or manually using the software ImageJ (Figure 3-1).

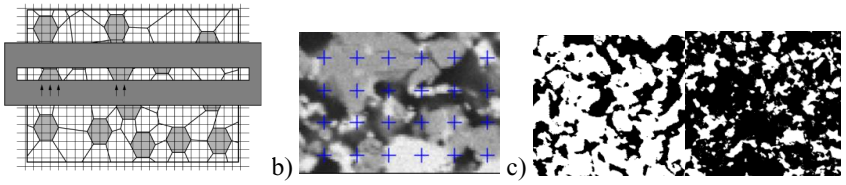

Figure 3-1: a) Line interception as detailed in DIN EN ISO 13383, b) crosses inserted by Fiji software, c) binary images achieved by thresholding. [88]

White light surface topography measurement: The surface topography of samples was measured after sintering using the white light device Cyberscan CT350T (Cybertechnologies). The step size was set to 100 µm. Additional measurements were performed on cells in the green state to compare warpage and surface quality before and after sintering. The data was prepared using the ASCAN software, filtering measurements below 100 µm to separate background and sample and to enhance the visualizations.

Laser microscopy: A laser microscope from the KEYENCE VK-X3000 Series was used to investigate surface roughness of initial samples and defects in green tapes.

Differential Thermoanalysis – Thermogravimetry (DTA-TG): The STA 449 F1 Jupiter simultaneous thermogravimetry device from NETZSCH with alumina crucibles were used.

Dilatometry: Measurement of dimensional changes during heat-treatment was performed using three different dilatometers: horizontal, vertical, and optical. The standard measuring device was the (horizontal) NETZSCH Dilatometer 402C, samples were measured up to 1600 °C with a heating rate of 5 K/min. The NETZSCH TMA 402F1 vertical dilatometer was used for the sintering investigation of single-layer tapes. The settings used for the vertical dilatometer: Different heating rates (0.5, 1, 2, 5, 10, and 20 K/min) were used, with a holding period of 3 hours at 1550 °C, followed by cooling to room temperature at 10 K/min. Each heating rate was measured once, with selected rates repeated to test reproducibility. Data was processed using Proteus software and further analyzed with OriginLab. Optical dilatometry was performed using the TOMMIplus (ThermoOptical Measuring Device, Fraunhofer ISC); however, due to machine failures, the machine was only used for qualitative photographs of high-temperature sample deformation. The setup is pictured in Figure 3-2. The program for these measurements followed the standard heat-treatment procedure.

Calculation of activation energy: Activation energies were evaluated from dilatometric shrinkage data using the software NETZSCH Thermokinetics. Measurements recorded at different constant heating rates were imported into the software and analyzed using an integral isoconversional approach. The shrinkage data was normalized by defining the specimen length at the onset of sintering as 0 % conversion and the final measured length as 100 % conversion. For predefined conversion levels (2 %, 5 %, 10 %, up to 80 %, 90 %, 95 %, and 98 %), the software evaluates the corresponding temperatures for each heating rate. Apparent activation energies were determined by linear regression of the logarithm of the heating rate versus the reciprocal temperature at each conversion level, following the Ozawa–Flynn–Wall formalism implemented in the software.

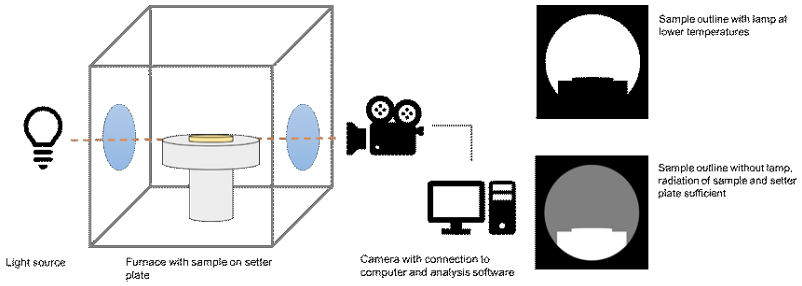

Figure 3-2: left) Schematic of optical dilatometry set-up, right) shadow outline of the samples inside the TOMMI furnace.

3.2 Machines and Devices

Two machines were used for homogenization: i) TURBULA 3D Shaker Mixer from WAB-group and ii) Thinky ARV-310 from Thinky Cooperation. The first device was used in all steps where milling or homogenization of the powders was the primary focus. The Thinky mixer was used in the standard slurry homogenization steps.

Multiple tape casting devices were used for the experimental work. They differed in size, accuracy, and experimental effort (such as availability, ease of cleaning, and operational demands). For slurry investigations, a lab bench tape caster was used (see Figure 3-3). The machine consisted of a vacuum suction device to fix the casting foil to the casting bed. At the time of the experiments, the automatic blade movement was out of order. Therefore, a metal bar with a precise distance of 100 µm between the cylinder and the carrier foil was used to manually draw the slurry over the carrier foil. As the carrier foil could be removed freely after casting, multiple casting experiments were performed without waiting for the tape to dry, significantly increasing experimental throughput. This was the major advantage of this machine. However, the setup was limited to small amounts of slurry and, due to the nature of the bar, was constrained by the different castable heights as well as limited reproducibility.

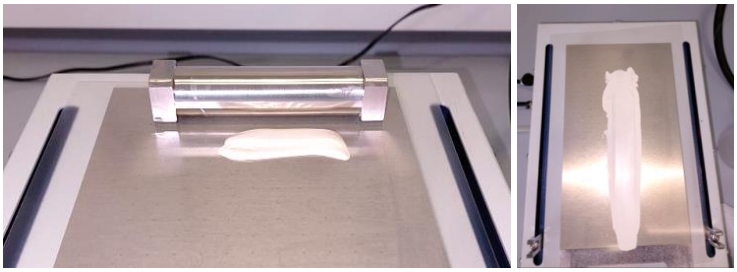

Figure 3-3: left) Slurry application with casting block of set height, right) after tape casting a low-quality slurry (table top tape caster, MTI Corporation).

The tape caster used primarily throughout the experimental work was the "KaroCast" Micro-tape caster (KMS, Germany, Figure 3-4, left), equipped with a moving roll-to-roll carrier foil, fixed reservoir, and adjustable doctor blade. It was entirely encased and explosion-save, with an individual fume suction system. The blade height was manually adjusted using two

micrometer measurement devices. For the sequential tape casting procedure, the roll was manually rewound to use the same casting head twice.

Figure 3-4: left) Medium size tape caster, “KaroCast”, KMS, right) industrial-size tape caster “JuCast”, KMS.

The third casting device was the "JuCast", an industrial-size tape caster also by the company KMS (Figure 3-4, right). It was equipped with multiple casting heads, allowing for sequential tape casting without reversing the coil. The casting bed width and length were longer, enabling one casting session to produce more tape and increasing the percentage yield of the tape, as the fade-in and fade-out of the slurry were of the same length (few centimeters at the beginning and the end). The disadvantage was that the experimental effort associated with using such a large device is immense. Casting with this machine required two trained technicians (if a new type of slurry is used), and the reservoir with the casting blade had to be inserted and removed using a crane.

For shaping the pressed powder pellets, a manual 2-pillar press was used. The lamination/warm-pressing was carried out using the servo-hydraulic 4-pillar laboratory press. Both presses were from the same supplier, P/O/Weber (Figure 3-5).

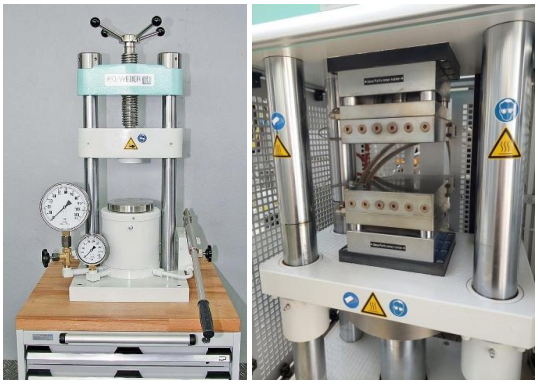

Figure 3-5: left) Manual 2-pillar press, right) servo-hydraulic 4-pillar-laboratory press both from P/O/Weber. [89]

Sample blanking was done using a punching tool, a scalpel and a ruler or an automatic cutting device (Cameo 4, Silhouette America, see Figure 3-6). The blades used were the “automatic blade” from Silhouette America. Cutting files were created using the Silhouette Studio software. The machine parameters included number of cutting runs (multiple cuts), blade speed, blade force (without unit), blade depth (without unit, approx. 100 µm per step).

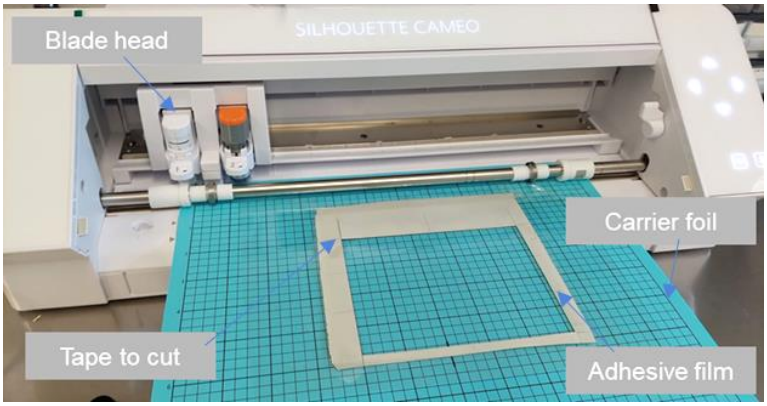

Figure 3-6: Automatic cutting device Cameo 4 from Silhouette America.

3.3 Target Cell Geometries

The standard procedure during cell development is to prepare small button cells based on dry pressed powder electrolytes. In the first step, symmetrical cells are tested to characterize the individual electrode contribution. Then, full button cells are produced. Figure 3-7 pictures schematically these different types of cells for pre-tests.

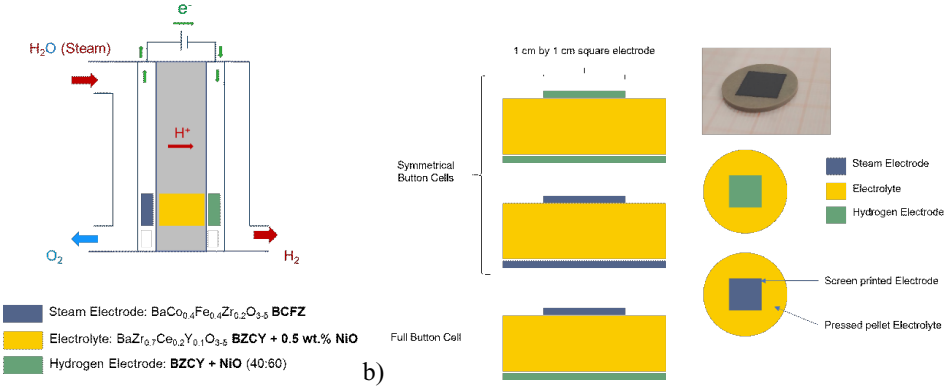

Figure 3-7: a) Schematic representation of a full cell, b) schematic representation of the primary symmetrical button cells.

The next step is transitioning to half-cell preparation through sequential tape casting. Only after these steps have been successful, it is advisable to attempt upscaling. Upscaling consists of two aspects: 1) producing larger cells and 2) increasing the number of samples produced. In this thesis, different types of half-cells or cell components were produced. Some configurations are only used for experiments supporting the development process. Figure 3-8 shows the cell configuration that is actually intended to be the result of this process. The obtained large-area cells are then suitable for stack integration, as it has been shown by Braun et al. [27]

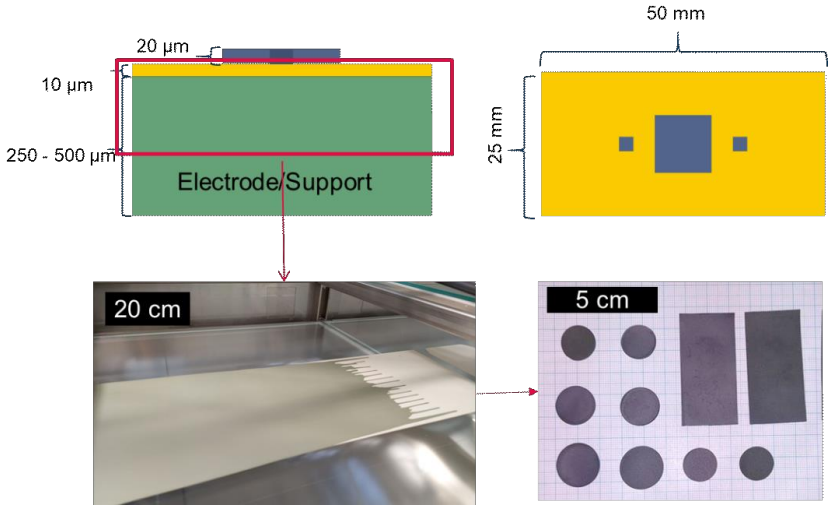

Figure 3-8: Schematic depiction of the target cell configuration, including the sequential tape casting process and target sample shapes.

For this thesis, multiple different types of tapes were prepared and are listed in Table 3-1. Thick electrolyte tapes were prepared for the shrinkage analysis as well as for the production of electrolyte-supported tape cast cells.

Table 3-1: Table of different types of tapes cast with their corresponding application in this thesis.

		Thickness (blade gap g)	Usage
Single layer electrolyte (thick)	El (thick)	g = 800 µm (KaroCast)	Electrolyte for symmetrical hydrogen electrode cells, shrinkage analysis, symmetrical steam electrode cells
Single layer electrolyte (thin)	El (thin)	g = 80 µm (KaroCast)	Sintering experiments, Symmetrical hydrogen electrode cells, symmetrical steam electrode cells
Single layer electrode	Su	g = 800 µm (KaroCast) g = 1200 µm – 1600 µm (JuCast)	Support layer
Bilayer	El|Su	g = 80 µm (electrolyte) + 800 µm (electrode) KaroCast g = 80 µm (electrolyte) + 1200 µm (electrode) JuCast	Sequentially tape cast bilayers

4 Powder Processing and Pellet Preparation

In ceramic processing, each manufacturing step critically influences the quality attainable in subsequent steps. Therefore, meticulous attention to the powder processing stages is essential. As outlined previously, initial developments in cell fabrication are typically conducted on dry-pressed pellets (Figure 4-1). These pellets serve a dual purpose: they enable characterization of the electrolyte material in isolation and function as the electrolyte layer for both symmetrical cells and prototype full cells.

Figure 4-1: Sample stages of electrolyte supported button cells (d = 25 mm).

During the course of this work, three major tasks were undertaken. The first task involved transferring the process developed in the ProtoMem project for the BZCY-622 composition to the BZCY-721 and BZCYYb-4411 compositions. This transition presented significant challenges, which are discussed in detail in this section. To address these difficulties, it was decided to procure the powders from an external supplier. While this resolved some of the initial issues, it introduced new complications into the process. The strategies employed to manage these subsequent challenges are also outlined in this section.

Table 4-1: Table of raw chemicals including stoichiometry, specific surface areas and particle sizes.

Chemical	**Supplier**	**Stoichiometry**	**BET in m^2/g**	**d_{10} in µm**	**d_{50} in µm**	**d_{90} in µm**
$BaCO_3$	Sigma Aldrich	$BaCO_3$	1.75	0.34	1.82	5.06
CeO_2		CeO_2	8.94	1.40	9.58	24.77
ZrO_2		ZrO_2	6.46	0.10	0.68	3.94
Y_2O_3		Y_2O_3	3.41	3.71	5.95	9.23
NiO (Vog)	Vogler	NiO	3.77	0.51	1.33	5.20
NiO (MT)	Marion Technologies	NiO	1.42	0.54	1.38	4.38
NiO (Bak)	J.T. Baker	NiO	4.13	0.11	0.83	59.56
BZCY-721 21K1	Marion Technologies	$BaZr_{0.7}Ce_{0.2}Y_{0.1}O_{3-\delta}$	3.87	0.09	0.59	45.83
BZCY-721 22K2	Marion Technologies	$BaZr_{0.7}Ce_{0.2}Y_{0.1}O_{3-\delta}$	3.16	0.39	7.05	72.31
BZCY-721 22K4	Marion Technologies	$BaZr_{0.7}Ce_{0.2}Y_{0.1}O_{3-\delta}$	5.07	0.51	1.56	45.07
BZCY-721 23K1	Marion Technologies	$BaZr_{0.7}Ce_{0.2}Y_{0.1}O_{3-\delta}$	6.90	0.27	6.49	85.71
BCFZ 22K1	Cerpotech	$BaCo_{0.4}Fe_{0.4}Zr_{0.2}O_{3-\delta}$	1.76	1.91	3.77	6.58

4.1 Initial Powder Processing and Pellet Pressing Procedure

This section outlines the initial process, the challenges encountered, and the corresponding solutions implemented.

4.1.1 Initial process from raw oxide/carbonate mixture to sintered pellet

The initial process began with raw oxide and carbonate mixtures, which underwent distinct heat-treatments depending on their intended use: BZCY for the electrolyte layer and BZCY for the substrate layer. Following heat-treatment, the powders were dry-pressed into circular pellets and subsequently sintered.

Solid state reaction: The base ceramic powder mixture was produced by weighing $BaCO_3$, ZrO_2, CeO_2 and Y_2O_3 in the stochiometric amounts for $Ba_{1.015}Zr_{0.7}Ce_{0.2}Y_{0.1}O_{3-\delta}$. (see Table 4-1) Over-stoichiometric Ba was added to account for Barium evaporation. The mixture was then combined with denatured ethanol and ZrO_2-grinding balls for mixing on the TURBULA mixer for 24 hours at 72 rpm. The mixture was subsequently dried at 80 °C overnight on a heating plate. The powder was split into two fractions. One part of the material was calcined at 1100 °C for 6 hours with a heating/cooling rate of 3 K/min (electrolyte powder EPu), and the other part was calcined at 1300 °C for 8 hours with a heating/cooling rate of 3 K/min (electrode/support powder SPu). After calcination, 0.25 wt.-% of NiO was added as a sintering aid to the EPu powder and mixed again with ethanol and grinding balls as detailed above.

Dry pressing: After the second homogenization and drying step, the powders were pressed using a manual 2-pillar laboratory press, with glycerin as a pressing additive (1 droplet per g). Table 4-2 depicts the pressing parameters for these samples.

Table 4-2: Pressing parameters for manual pressing.

Manual pressing parameters	Powder weight	4 g
	Holding time	3 min
	Pressing force	~ 25 kN
	Mold diameter	25 mm
	Calculated pressure	~ 50 MPa

Sintering of pellets: The pellets were then sintered in a crucible: stacked on top of each other, separated and covered with some sacrificial powder at 1550 °C for 6 hours with a heating/cooling rate of 2 K/min.

Results: Along the entire process several challenges were apparent: The initial hurdle was the preparation of pressed pellets. Many samples broke during pressing. Figure 4-2 depicts two examples of broken green bodies. Picture a) shows pellets which broke during the ejection phase of the pressing process with cracks running orthogonally or slightly slanted to the pressing direction. Picture b) shows the characteristic ring capping. The green bodies which only fractured partially (such as Picture b) were sintered. However, all pellets fractured either during the sintering process or immediately upon removal from the crucible (Picture c).

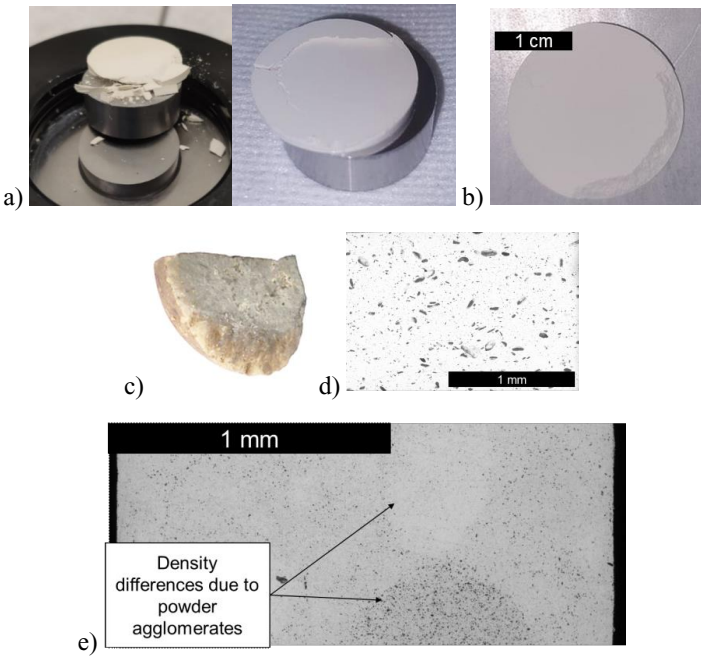

Figure 4-2: Examples of problems during sample preparation: a) broken samples after the pressing step, b) ring-capping after ejection, c) broken sample after sintering with inhomogeneous visual appearance, d) example of microstructure after insufficient distribution of pressing agent example of microstructure with density gradients possibly due to powder agglomerates.

Microstructure analysis showed that pellets showed different defects. Picture d) shows pores up to 200 µm in length which are attributed to an excessive amount and insufficient homogenization of the pressing agent. Picture e) depicts the large differences in densities across the entire pellet possible due to powder agglomeration.

Conclusion: The general assessment of the initial process indicated that it was not suitable for this powder. The main issues included excessive defects during pressing, fractures and inhomogeneities after sintering, and microstructural flaws revealed by SEM analysis. The SEM investigation suggested improper use of the pressing agent as one source of defects, along with insufficient density and density gradients within the material.

4.1.2 Direct improvements to the initial process

Several improvements were implemented in the powder processing and pellet pressing procedures.

Pre-pressing to enhance density distribution: To improve the pressing process, crack formation was analyzed. Based on the theoretical background, the initial cracks were attributed to delamination caused by air entrapment within the sample and uneven density distribution. This issue was addressed by introducing a de-airing step for subsequent pellets. Before the final pressing step, a pre-pressing force of 10 kN was applied for approximately 10 seconds, followed by decompression and the standard pressing step as described earlier.

Variation of pressing agents: Different pressing agents were evaluated, including glycerin, polyvinyl alcohol (PVA), and water each at 1 droplet (using a Pasteur pipette) per g. (When using a disposable 3 ml Pasteur pipette, one droplet of water can vary in volume between 0.05 ml and 0.15 ml depending on the pipette type. [90] higher weight and surface tension of glycerin, the volume is even less controlled, introducing a significant limitation in reproducibility.) The most favorable results were achieved using water.

Mitigating fracture during ejection: To mitigate spring-back effects caused by elastic compression, the pressure was released at a slower rate (manually by opening the valve more gradually). While the resulting pellets occasionally exhibited ring-capping, this defect was deemed acceptable for the intended use case.

Cold-isostatic pressing: The samples were subjected to cold isostatic pressing (CIP) at 2000 bar for 120 seconds. Some bending was observed after the pressing process (Figure 4-3). The warpage exhibited by the pellets after cold isostatic pressing persisted after sintering. Consequently, the sintered samples required grinding to achieve a uniform thickness for subsequent screen-printing. Despite this, the pellets approximately retained their original shape, in contrast to those that had not undergone cold isostatic pressing (CIP) prior to sintering. Additionally, the crack orientation differed significantly from the initial samples. Instead of horizontal cracking, the cracks in the cold isostatically pressed samples propagated vertically from the outer edge towards the center (compare Figure 4-3).

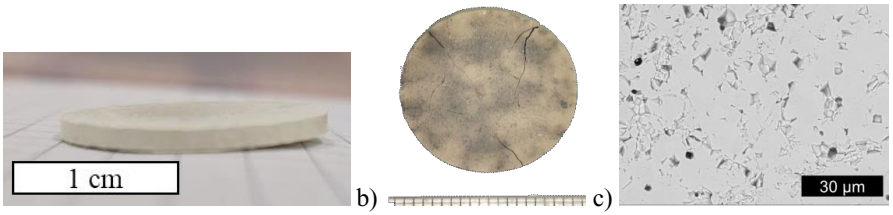

Figure 4-3: a) Green pellet, bent after cold isostatic pressing, b) defect pattern in a sample after sintering c) SEM micrograph of cross-section.

4.1.3 Causes for Failure of Initial Process

The issues encountered in this work were not present in the previous project, prompting an in-depth investigation of the powders used in the ProtoMem project. [77] Three key differences were identified: a smaller particle size, the addition of 0.5 wt.-% NiO instead of 0.25 wt.-%, and the inclusion of repeated calcination and milling steps.

Table 4-3: Properties of powders produced within the ProtoMem project.

	BZCY-625-2-175 – MPI (+0.5 wt.-% NiO)	**BZCY-625-2-175 – E2 (+0.5 wt.-% NiO)**
d_{10}	0.07 µm	0.66 µm
d_{50}	0.13 µm	1.62 µm
d_{90}	2.75 µm	3.87 µm

Two powders were analyzed to determine the difference in particle size. Figure 4-4 displays the PSD curve and Table 4-3 lists the powder properties of the previous project. On the left the powder produced by the Max-Plank-Institute for Solid State Research (Stuttgart, Germany) used for tape casting and on the right the powder produced through a similar process as above.

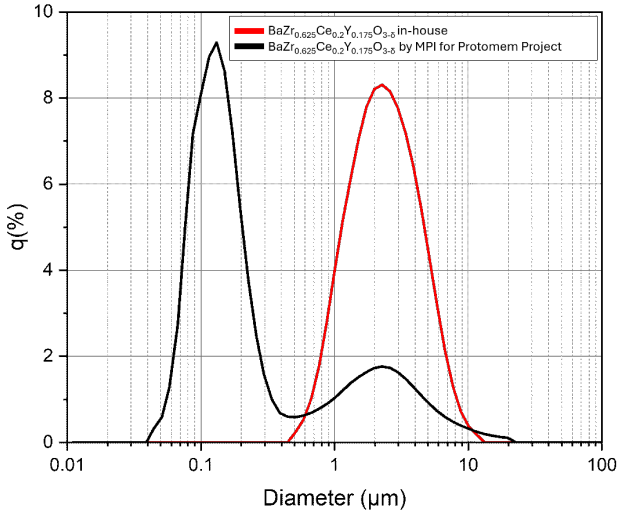

Figure 4-4: PSD of powder from the Max-Plank-Institute used in the ProtoMem project (black) and in-house powder of the same stoichiometry (red).

It became clear that particle size of the original composition lies below that achieved in the above introduced process. Even though the stoichiometry was the same for both powders, the particle size distribution was very different. This was due to the difference in powder production processes. The powder produced at MPI for the ProtoMem project was calcined using an ultrahigh speed heating method which is not available at IMD-2 and therefore not used in this work. However, even the in-house synthesized powder using the process as introduced initially led to d_{50} values of 1.62 µm for this particular composition, implying that the issue might also be stoichiometry dependent.

Table 4-4: Results of modified milling procedure.

	Electrolyte Batch	**d_{10}**	**d_{50}**	**d_{90}**	**Substrate Batch**	**d_{10}**	**d_{50}**	**d_{90}**
		in µm				in µm		
Initial procedure	B5 El + 0.25 wt.-% NiO	1.00	2.65	6.48	B6 Su	3.39	6.70	13.75
Adjusted procedure	B8 El	0.29	2.01	15.38	B8 Su	0.67	3.33	22.61

Decrease of particle size through improved milling process: First adjustments of the process are shown in Table 4-4. The adjustment consisted in using a ratio of 1:2:3 for powder : milling balls: ethanol to be milled on the tumble mixer. The change led to a decrease of the particle size characteristics d_{10} and d_{50} but the d_{90} values increased significantly. This suggests that the modified milling procedure might increase the risk of agglomerate formation. But ultimately, this improved milling procedure was chosen. However, the particle sizes still exceeded those of the ProtoMem project.

Improving phase composition through multiple calcination steps at 1100 °C: The results are depicted in Figure 4-5. The phase structure of the calcined powder can be matched to an

yttrium-substituted barium zirconate and a barium cerate. The two additional calcination steps did not influence the phase composition. However, the powder that underwent three calcination cycles exhibited an additional peak in the particle size distribution, corresponding to hard agglomerates around 100 µm in diameter, which can lead to substantial density gradients within a pellet or tape. Therefore, repeated calcination and milling steps were excluded because it did neither improve the phase composition nor the particle size.

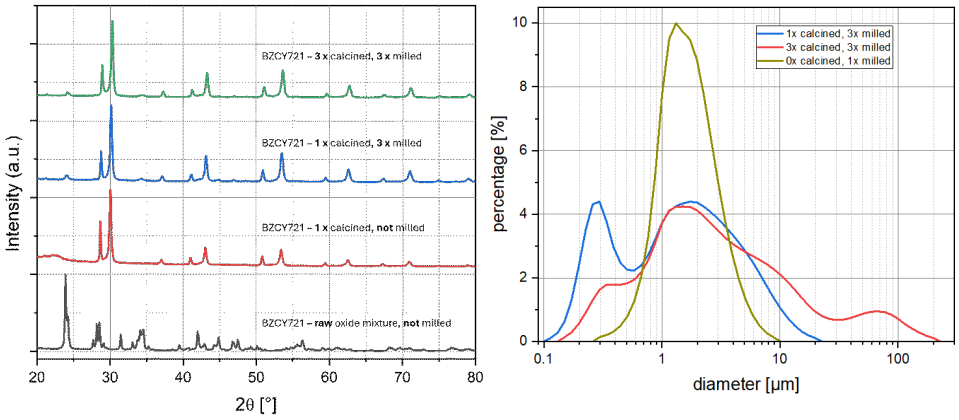

Figure 4-5: left) XRD spectra and right) PSD analysis of SSR-powder at different stages of the 3 × calcination and 3 × milling process.

Increase in NiO concentration as sintering additive and change of supplier: Comparison with the published ProtoMem results showed that an NiO concentration of 0.5 wt.-% was optimal for the electrolyte composition. [77] The initially used concentration of 0.25 wt.-% was based on an earlier calculation error. Increasing the NiO content to the corrected value of 0.5 wt.-% led to a substantial improvement in sintering outcome. Another factor identified as having a major influence on the manufacturing success was the NiO supplier. Changing the supplier from J.T. Baker to Marion Technologies did not improve the process. However, returning to NiO supplied by Vogler improved the sintering results. One possible explanation is that the three NiO powders differed in their particle size distributions, which may have affected the homogeneity of NiO dispersion and thereby reduced the formation of density gradients.

Investigation of raw materials as a source for inhomogeneous electrolyte calcination: One strategy to decrease the particle size prior calcination was the separate milling of the raw materials. Analysis of the particle size distributions of the starting oxides and carbonate revealed large differences in particle size. It would have been an option to mill the powders of larger particle sizes before preparing the raw oxide mixture. This route would have been pursued if the decision to go forward with purchased powders would not have been made.

Other challenges: Additional issues were found to occur after storing the samples for a certain time. Spontaneous breakage was recorded for several samples after storage in the laboratory for three weeks. Figure 4-6 a) depicts the sample right after sintering. Picture b) documents the appearance of a multitude of cracks in the entire sample. Pictures c) -to d) show the microstructure of this specimen using SEM. Picture c) documents the crack formation and also

hints at the formation of zones of varying densities which might be related to internal stresses after sintering which might have caused the delayed cracking. Picture d) shows the appearance of stacking faults which were more frequent around the cracks then in the matrix. [40] This phenomenon happened to several samples which were stored together during this period. It was observed that the tendency of the sample to fracture was increased if the sample appeared to be not fully sintered. One possible reason for the breakage could be the formation of $BaCO_3$ on the surface. This reaction might be triggered by the presence of barium outside the perovskite structure. This was an indicator for deciding against over-stoichiometric BZCY to be purchased.

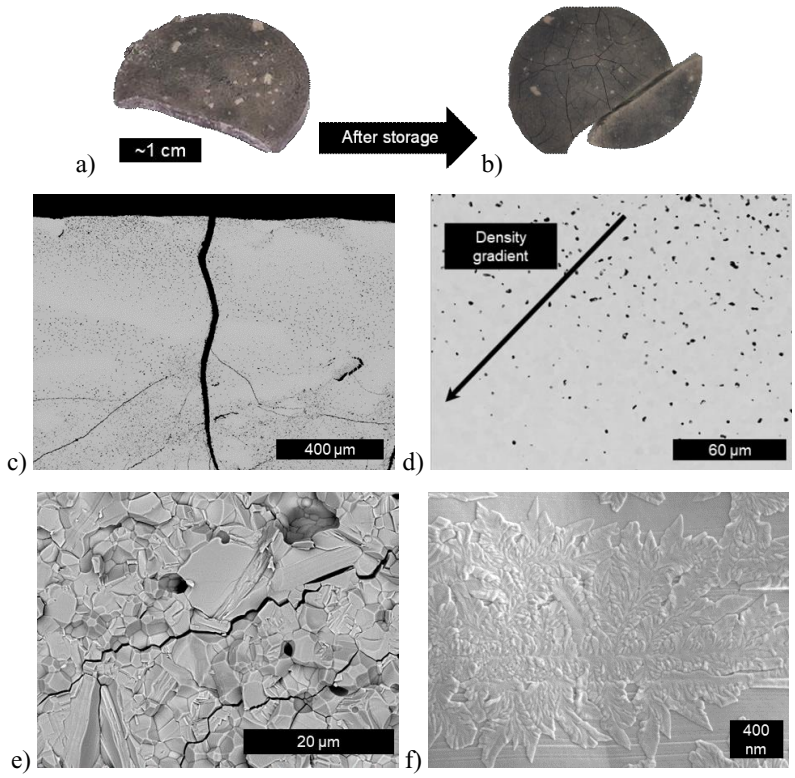

Figure 4-6: BZCY-721 sintered at 1550 °C: a) before and b) after several weeks; SEM polished cross-section: c) crack formation and inhomogeneous density distribution inside the sample, d) density gradient; SEM fracture surface: e) formation of substructures of stacking faults, f) formation of dendritic structures, potentially $BaCO_3$.

4.2 BZCYYb-4411 as Electrolyte Material

4.2.1 Background and Motivation

The two electrolyte material candidates investigated in this thesis were BZCY-721 and BZCYYb-4411, both of which are currently considered standard materials for proton-conducting electrolytes. [1],[13] At the outset of this thesis, the focus was placed on investigating both compositions. The high cerium content in the latter composition was expected to enhance sinterability. The primary objective of this experimental section was to

evaluate the transferability of the initial process to the alternative electrolyte material BZCYYb-4411.

4.2.2 Experimental Set-Up

For this experimental series, powders of the different variations were produced. The powders were not independently synthesized but rather derived from a common raw oxide/carbonate mixture. Figure 4-7 shows a relationship diagram illustrating the powder synthesis variation. The powders were analyzed using the D4 diffractometer.

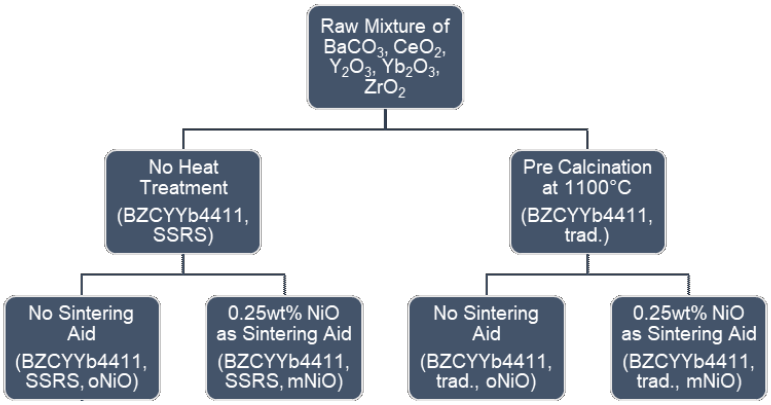

Figure 4-7: Schematic of different compositional variations of BZCYYb.

4.2.3 Results and Discussion

Figure 4-8 illustrates the XRD results for calcined and non-calcined BZCYYb powders, both with and without the addition of NiO as a sintering aid. The XRD patterns for the non-calcined powders (top patterns) are nearly identical, as the addition of 0.25 wt.-% NiO does not significantly influence the overall diffraction results. However, the situation differs for the calcined powders, where additional peaks are observed. A comparison with the characteristic NiO pattern confirms that these peaks are not attributable to NiO. Notably, the first peak at 23.94 ° corresponds to $BaCO_3$ indicating its presence in the sample. Since the calcination process was only partially completed, the appearance of multiple phases in the XRD spectrum is not unexpected. It is important to note that the calcined powder containing NiO originates directly from the powder without NiO, with the only difference being the subsequent addition of NiO and homogenization using a tumble mixer. This strongly suggests that the formation of $BaCO_3$ occurred during the mixing process.

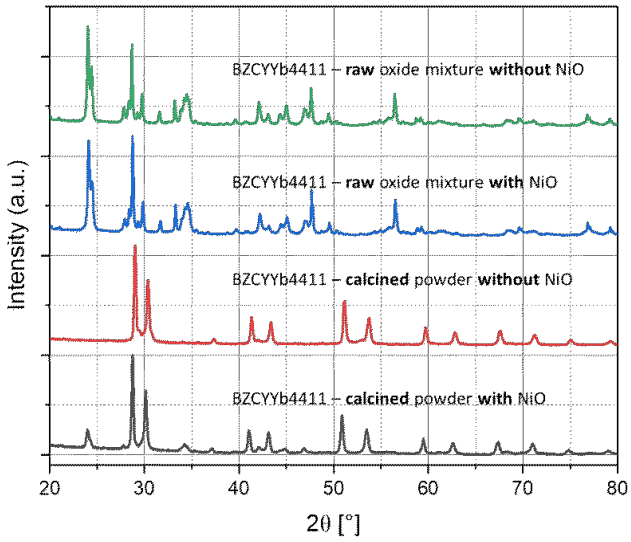

Figure 4-8: XRD diffractograms of the calcined BZCYYb composition for the non-calcined powder (top) and the calcined powder (bottom) with and without the addition of NiO. Additional peaks in the calcined powder with NiO can be matched to $BaCO_3$ not NiO.

Figure 4-9 presents the particle size distribution analysis. While the particle size distribution of the standard BZCY-721 powder can be generally characterized as monomodal, the BZCYYb-4411 powder exhibits a polymodal distribution. Notably, the BZCYYb-4411 powder contains hard agglomerates with diameters of approximately 100 µm.

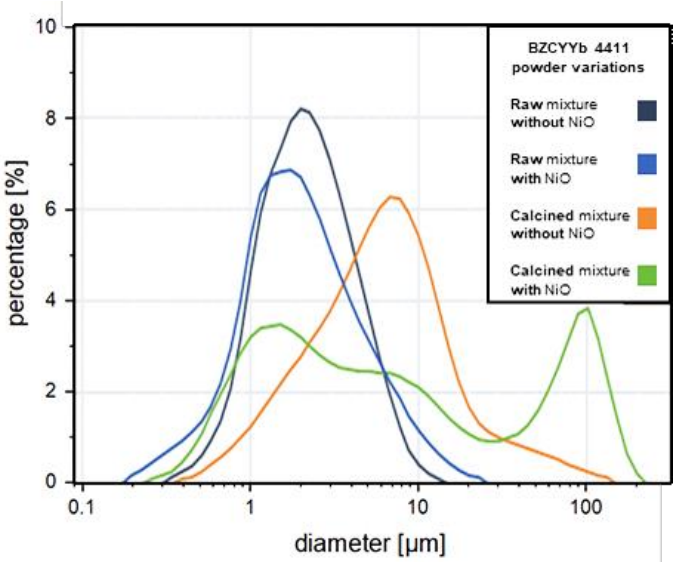

Figure 4-9: Particle size distribution of all BZCYYb-4411 variations.

4.2.4 Conclusion

The calcination results for the BZCYYb powder indicate that the addition of NiO, or more specifically, the mixing procedure in ethanol, resulted in the formation of $BaCO_3$. This observation, combined with the polymodal particle size distribution of the powder after preprocessing and the existing challenges in processing the BZCY-721 composition, led to the decision to exclude the BZCYYb composition from further experiments in this thesis.

4.3 Scalability Challenge: Transition to Purchased Powder

It was observed that the powder preparation process introduced numerous challenges. Beyond the previously mentioned issues, the most significant impact on this work stemmed from scalability limitations. The initial powder preparation process employed the solid-state reaction method, which is well-suited for laboratory-scale production. However, scaling up introduces additional complexities. Key challenges include managing the large volumes of ethanol required and ensuring its safe evaporation—posing both safety risks and time constraints. Furthermore, the availability and size limitations of explosion-proof heating cabinets significantly affect drying conditions and subsequent preparation steps, presenting further barriers to scalability. For a scalable process that requires large-scale samples, ideally cut from the same tape, multiple kilograms of powder are needed. However, the existing lab-scale process, while effective for small batches, reaches its practical limit at approximately 50–100 grams.

As a result, the decision was made to purchase BZCY-721 powder from a supplier capable of producing large quantities within a single batch. This approach not only ensures consistency but also mitigates health hazards associated with ceramic powder handling—such as mixing, drying, and sieving—particularly when repeated calcination steps are required.

4.3.1 Characterization of Purchased Powder

The purchased powder was successfully used to prepare sintered samples, which remained intact after sintering. However, samples prepared using purchased powder Batch 22K2 exhibited the formation of a Ce-Y-oxide phase. Figure 4-10 displays the XRD spectra of two sintered bilayers produced using in-house BZCY powder and one using the purchased powder. The spectra reveal that the electrolyte layer based on the in-house powder appears to be single-phase, while the electrolyte layer prepared with the purchased powder shows an additional Ce-Y-oxide phase. Another notable difference lies in the predominant BZC-phase: The in-house powder matches the reflection peaks of the rhombohedral crystal structure (BZC-46), whereas the purchased powder aligns more closely with the cubic crystal structure (BZC-91).

From an engineering perspective, this difference is not critical to the production process, as both structures exhibit proton conductivity. However, the presence of the Ce-Y-oxide phase may reduce the yttrium content in the bulk material, potentially leading to a lower vacancy concentration, which could, in turn, decrease proton conductivity.

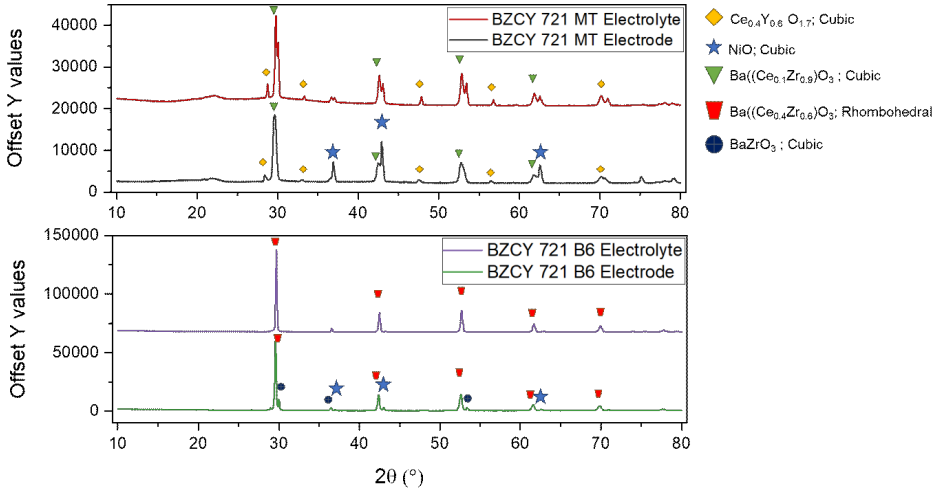

Figure 4-10: XRD diffractograms of the electrolyte side and the substrate side of sintered bilayers. The top diagram refers to samples based on purchased BZCY-721 22K2 and the bottom diagram to the in-house BZCY-721.

The powder was subjected to heat-treatment to investigate whether the phase composition could be influenced by this process. XRD measurements, conducted after holding times of 3, 6, and 9 hours, confirmed the persistent presence of a Ce-Y-oxide phase. The occurrence of this phase is concerning, as it may lead to unfavorable performance when present in the electrolyte. Figure 4-11 further reveals a noticeable shift in the XRD patterns from $BaZrO_3$ towards $Ba(Ce_{0.1}Zr_{0.9})O_{3-\delta}$ at longer holding times, indicating compositional changes within the material over time.

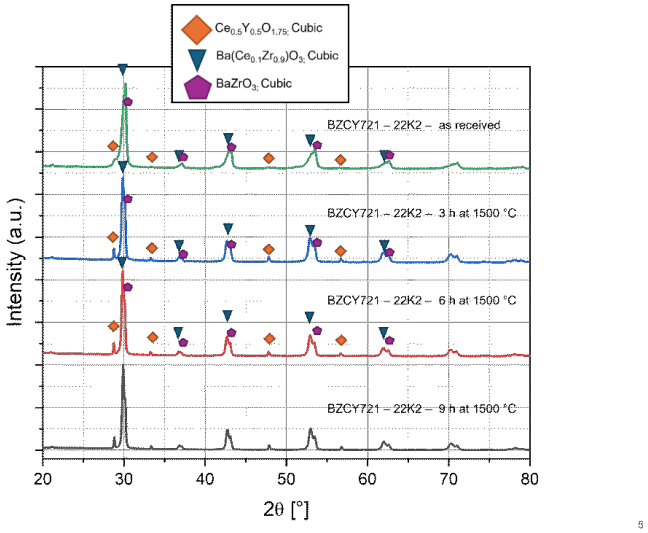

Figure 4-11: XRD diffractograms of BZCY-721 22K2 powder as-received and heat-treated at 1500 °C for 3, 6 or 9 hours.

The powder was eventually replaced by the supplier. However, multiple samples in this thesis were based on this batch of powder. Two additional batches of powder were received: 22K4 and 23K1. The Figure 4-12 depicts the particle size distributions as well as the different XRD spectra of the powders. It is evident, that especially with regard to the particle size distribution, reproducibility of the powder is limited.

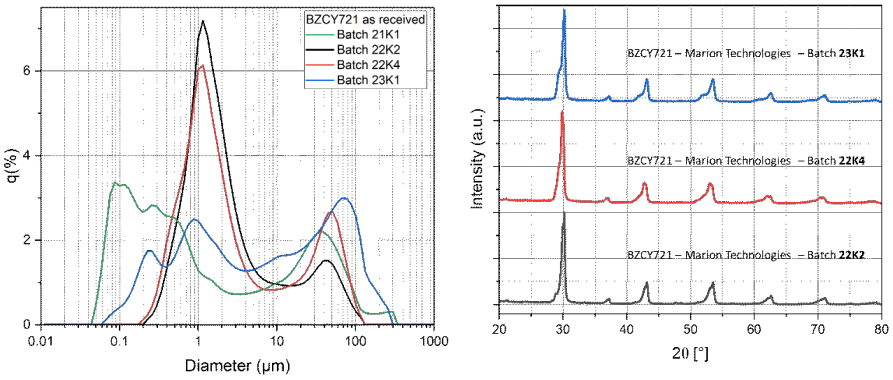

Figure 4-12: left) Particle size distribution and right) XRD spectra for different batches of purchased powders.

Although the formation of Ce-Y-oxide secondary phases was not initially detected in these powders (as determined through XRD analysis of sintered cells), subsequent measurements conducted at Philipps University Marburg confirmed the presence of this secondary phase in samples prepared with Batch 22K4 (see supplementary Figure 12-5 and Figure 12-6).

4.4 Conclusion of Powder Processing and Pellet Preparation

Meticulous powder processing is essential for producing high-quality ceramic samples. During the initial investigations, several significant challenges were identified: inadequate particle sizes, suboptimal pressing process, insufficient density, density gradients and crack formation during sintering.

To address these challenges, several process improvements were investigated. A key improvement was the increase of sintering aids; by increasing the NiO content to 0.5 wt.-% and switching to a different supplier, the sinterability of BZCY-721 improved significantly. Pressing parameters were also adjusted. Replacing glycerin and PVA with deionized water as a pressing agent improved the density of sintered samples, offering a simpler and cleaner solution. Additionally, the introduction of cold isostatic pressing (CIP) further densified uniaxially pressed pellets, although this process introduced deformation that required subsequent grinding to achieve flat surfaces suitable for later stages of preparation. Finally, sintering the samples inside a powder bed improved the density and quality of the sintered samples.

A major process change during the course of this work was the decision to transition from in-house powder synthesis to using commercially sourced BZCY-721 powder. The challenges of producing high-quality powder in-house, such as difficulties with phase formation, particle size control, and batch scalability, made this shift necessary. Purchased powders offered several

advantages: their production at kilogram scale ensured slurry batch-to-batch consistency and significantly reduced the time and effort needed for quality control. This change not only simplified the process but also enabled consistent slurry preparation and tape production, which are critical for scalable manufacturing.

The findings of this chapter can inform further research in two distinct ways. On the one hand, the multitude of minor changes and observations presented here can serve as a valuable reference for future researchers employing the standard solid-state reaction process to produce powders and pressed pellets of this composition. On the other hand, for recreating the process developed in this thesis with the goal of manufacturing larger-scale cells: it must be emphasized that the best course of action is to purchase commercially produced powders. This avoids the complications and inefficiencies associated with handling insufficient powder quantities for experimental purposes.

5 Slurry Preparation and Tape Casting

After the processing of ceramic powders, the next critical step involved forming layers with organic binder systems during slurry preparation and tape casting. This section focuses on the steps undertaken during these processes, detailing their evolution and optimization throughout the experimental work of this thesis.

The initial procedure was based on the method developed by Menzler et al. and Schafbauer for solid oxide cells (SOCs). [33,62] This method was subsequently adapted by Deibert et al. to meet the specific requirements of the BZCY-composition within the ProtoMem project. [4] While the procedure provided a functional starting point, it revealed several limitations, particularly when using the KaroCast tape caster. Defects such as thickness inconsistencies and surface irregularities frequently occurred, necessitating further investigation and refinement. The work conducted in this section focused on the following key aspects of slurry preparation and tape casting:

- Variation of base ceramic electrolyte powder: Non-calcined BZCY-mixtures were used as the base electrolyte powder to improve sinterability.
- Variation of slurry composition
    - Dispersant type and amounts: Different dispersants and their concentrations were systematically studied to assess their impact on slurry stability and homogeneity.
    - Solvent types: Various solvents were evaluated to optimize slurry viscosity and improve drying behavior during tape casting.
    - Improved slurry compositions: Experimentally-derived modifications to the original slurry formulations were tested to address specific issues, such as pinhole formation and weak layer adhesion.
- Transfer of process from KaroCast to JuCast: The medium scale slurry preparation and tape casting process was adapted to the use of the large-scale tape caster JuCast.

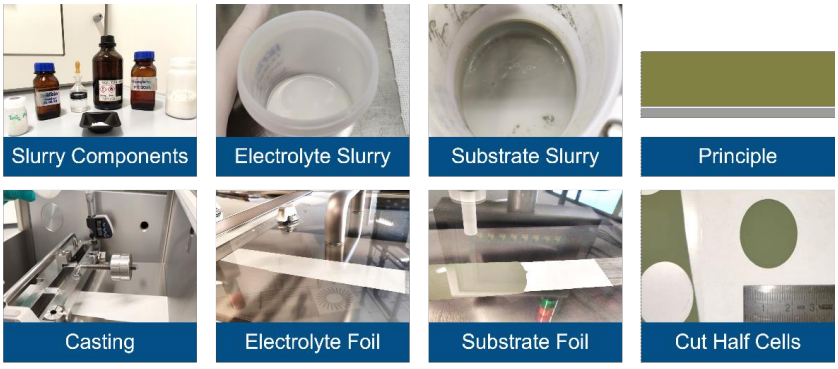

Figure 5-1: Overview of the slurry preparation and sequential tape casting process.

5.1 Initial Slurry Preparation and Tape Casting Process

The core structure of all half-cells consisted of a sequentially tape cast bilayer comprising a thin electrolyte layer and a thicker hydrogen electrode layer. For full-cell configurations, an additional support layer was required to enhance mechanical stability, as sintered bilayers alone proved too fragile for handling. The initial process involved preparing separate slurries for each layer and sequentially casting them to form the bilayer.

The overall process of the sequential bilayer tape casting process is depicted in Figure 5-1. The ceramic powder was mixed with a system of organic additives (see Table 5-1). Generally, two different types of slurries were used in this thesis: electrolyte (Named Year-ES-Nr.) and hydrogen electrode/substrate slurries (Year-SS-Nr.). All slurries were mixed in the following order. First the milling balls were weighed into the container. Then the Ethanol/MEK mixture was added and then the dispersant Nuosperse. The container was gently moved to allow the solvent and dispersant to mix.

Table 5-1: Polymers used as slurry components.

Name	Supplier	Chemical	Use
BUTVAR PVB B-98	Eastman	Polyvinyl Butyral	Binder
Nuosperse FX9086	Elementis	Polymeric surfactant dissolved in methoxy propyl acetate	Dispersant
PEG-400	Merck	Poly(ethylene glycol)	Plasticizer Type I
3G8 Ester	OXSOFT	Triethylene glycol-di-(2-ethylhexanoat), 2,2'-Ethylendioxydiethyl bis(2-ethylhexanoate)	Plasticizer Type II

For the electrolyte slurry, BZCY-721 electrolyte powder (pre-reacted at 1100 °C with 0.25 wt.-% NiO as sintering aid) was used. For the hydrogen electrode/substrate slurry, the BZCY-721 electrode base powder (heat-treated at 1300 °C) and NiO were only mixed at this stage. This was 40 wt.-% in-house synthesized BZCY-721 powder produced through solid state reaction and 60 wt.-% NiO (J.T. Baker).

After the BZCY-721 powder and the NiO were added, the container was tightly closed, inserted into the Thinky mixer and homogenized for 3 min at 1000 rpm without vacuum. After a cooling down period, the further components were added in the following order: 3G8 Ester, PEG-400 and PVB 98. This was followed by a final mixing step at 1500 rpm for 3 min. After resting for 24 h, the slurry was mixed again at 1000 rpm for 3 min and again 24 h later at the same condition approximately 30 min before being cast.

Table 5-2: Tape casting conditions of the first run.

	Electrolyte layer	Hydrogen electrode layer
Blade gap	80 µm	800 µm
Speed of carrier foil	5 mm/s	2.5 mm/s
Relative humidity	34 %	34 %
Temperature	21.9 °C	22.1 °C

At the beginning of the casting process using the KaroCast, the carrier tape is started without slurry in the reservoir. After the movement speed has equilibrated, the slurry is poured into the

reservoir by hand, retaining the remaining milling balls through use of a spatula. The slurry reservoir is bordered to the side with aluminum space holders to restrict the flow of the slurry to the sides. The casting parameters and conditions for the first tape casting run are given in Table 5-2.

First, the electrolyte layer (white/grey in Figure 5-1) was cast and after drying (~ 4-6 h) the carrier foil was manually rewound and the electrode slurry (dark green Figure 5-1) was cast directly onto the electrolyte layer. The hydrogen electrode layer was cast in such a way that not the entire electrolyte tape was in contact with the electrolyte layer and therefore these sections could be used as single layer support. In subsequent casting runs, an additional substrate layer of a slurry with the same composition was cast as a single layer. After the tape had dried (~ 17 h), the tape was removed from the machine. To produce half-cells, the tape was cut using different tools and single layer substrate and bilayer were are joined using a warm press. (See Chapter 6 for details of the lamination and cutting process)

Samples are sintered using the following program: a heating rate of 0.5 K/min to 900 °C, followed by 2 K/min to 1500 °C, with a 3-hour hold at 1500 °C, and a cooling rate of 2 K/min. (See Chapter 7 for details of the heat-treatment process)

5.2 Bilayer Tapes with SSRS-based Electrolyte Powders

One approach to improving the density of ceramics involves leveraging the driving force of solid-state reactions to form complex oxides directly from raw oxide/carbonate mixtures ($BaCO_3$, CeO_2, ZrO_2 and Y_2O_3) during the sintering process. This method eliminates the need for a separate calcination step to pre-react the ceramic powder, potentially enhancing densification and reducing processing complexity. Non-calcined powder of a slightly different stoichiometry ($Ba_{1.015}Zr_{0.625}Ce_{0.2}Y_{0.175}O_{3-\delta}$) with 0.5 wt.-% NiO was studied in the project ProtoMem and it was shown that successful casting of electrolyte tapes from this raw mixture is generally possible. [91] In this experimental part, the target was to see if sequentially tape cast bilayer tapes could be successfully be prepared.

5.2.1 Experimental Set-Up

The slurry preparation and tape casting procedure was the initial process as detailed above using the KaroCast machine. Table 5-3 gives an overview of the ceramic powders used for these specific experiments and Table 5-4 gives the full composition.

Table 5-3: Slurry and tape abbreviations for SSRS tests.

	22-ES-1	**22-SS-1**	**22-SS-2**	**22-SS-3**
Ceramic powder	Batch 7 SSRS + 0.25 wt.-% NiO (J.T. Baker)	40 wt.-% Batch 6 calcined 1300 °C 8 h + 60 wt.-% NiO (J.T. Baker)	40 wt.-% MT 22K2 + 60 wt.-% NiO (J.T. Baker)	

The slurries 22-ES-1, 22-SS-1 and 22-SS-2 were initially planned for bilayer tapes and 22-SS-3 was planned as single layer support tape. This plan was adapted to respond to the unexpected defects occurring in 22-ES-1. Finally, three bilayer tapes were cast with differing electrolyte layer drying times. The surface structure of the resulting half-cells was analyzed using the Keyence laser microscope.

Table 5-4: Slurry compositions of tape casting series 22-1.

	22-ES-1	**22-SS-1**	**22-SS-2**	**22-SS-3**
BZCY-721 Batch	B7 Raw + 0.25 wt.-% NiO	B6 1300 °C 8h	MT 22K2	MT 22K2
Intended use	Electrolyte	Electrode	Electrode	Support
Electrolyte drying time before sequential casting	NA	6 h	24 h	48 h
	Weight in g			
Powder	14.98	19.99	19.97	29.97
Additional NiO	NA	29.99	30.02	45.04
Ethanol/MEK Ratio 34/66	5.83	18.56	18.58	27.83
Nuosperse FX9086	0.23	0.75	0.75	1.13
PVB 98	1.05	3.50	3.50	5.24
3G8 Ester	0.53	1.74	1.74	2.63
PEG-400	0.53	1.75	1.74	2.64
Milling Balls (3mm ZrO_2)	15.05	49.92	50.09	74.90

5.2.2 Results and Discussion

During the casting process, the electrolyte slurry (22-ES-1) exhibited an unexpectedly bad pouring behavior as compared to the non-SSRS slurries. The slurry did not distribute equally along the doctor blade which led to different slurry filling heights inside the reservoir. (This is generally considered a prerequisite of constant thickness across the tape width.) This led to the in-situ adjustment of the width defining blocks to ~ 10 cm distance. The cast tape dried well, remaining crack-free and without significant defects.

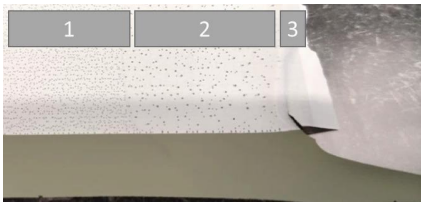

Figure 5-2: Defects in electrolyte side of bilayer with electrolyte slurry based on raw mixture of BZCY-721, section 1) small pinholes aligned along the casting direction, section 2) larger holes with more random positioning and section 3) no holes in electrolyte tape that was not covered by electrode slurry.

The 22-SS-1 tape covering the 22-ES-1 tape showed no cracks after drying. However, after removal of the bilayer tape from the carrier foil, 22-ES-1 was found to have developed circular defects across the entire tape. These holes were observed exclusively in the electrolyte layer and only in areas covered with electrode slurry; no holes appeared in the single-layer electrolyte tape. Figure 5-2 shows an image of these defects on the electrolyte tape, revealing three distinct areas. In the left region (1), small, regularly spaced holes aligned with the casting direction were visible. In the middle region (2), the holes were more dispersed and less evenly aligned. The right region (3) exhibited no holes. The differences between these regions appear to have

resulted from the depletion of the electrode slurry reservoir during casting, leading to the region (2) being covered with a thinner layer of electrode slurry than the region (1).

Two different possibilities for the occurrence of these holes were found. Either gas bubbles were formed inside the electrolyte slurry regardless of the presence of the electrode slurry. Or a reaction between the electrode and the electrolyte slurry created a gaseous species. In the first case, the gas would have been produced inside the electrolyte slurry and diffused to the surface. The reason for the holes would have been the collection of the gas at the electrolyte/electrode interface. It was hypothesized that this effect could then be avoided by letting the electrolyte more time to produce the gas without being covered by the electrode tape.

Given the length of the electrolyte tape, it was possible to perform two additional tape casting steps on top of 22-ES-1 using slurries 22-SS-2 (24 h) and 22-SS-3 (48 h drying time). The casting process proceeded smoothly, with the slurries spreading evenly along the doctor blade. Both electrode tapes exhibited drying cracks. Hinting at the different drying behavior of the electrode slurry when using the purchased powder 22K2 as opposed to the in-house BZCY-721 Batch B6. Hole formation occurred in the electrolyte layer of all bilayer tapes regardless of drying times of 6, 24, or 48 hours, suggesting that the influence of the electrode layer went beyond the mere function of a gas blocking layer.

Sintered half-cells from these tapes were investigated using the Keyence Laser microscope Figure 5-3. The average hole depth was found to be 80 µm, suggesting that the holes extended beyond the electrolyte layer into the electrode layer. Figure 5-3 (bottom) shows an example where the hole depth even exceeds 100 µm, significantly surpassing the thickness of the electrolyte layer with a blade gap of 80 µm and a dried thickness of ~ 20 µm.

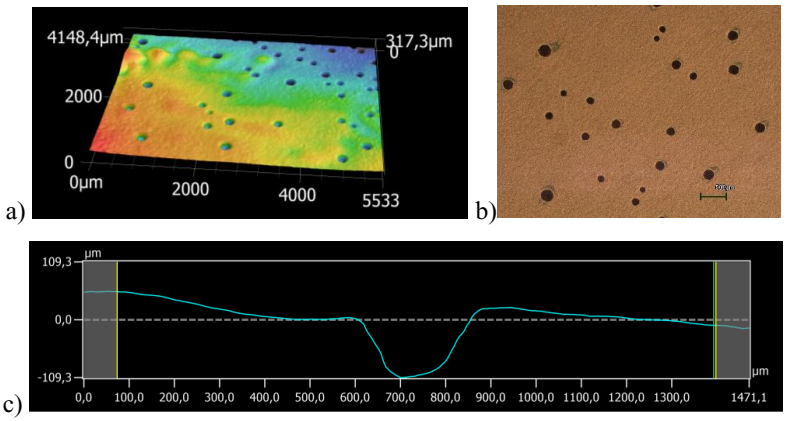

Figure 5-3: Surface topography of sintered tape based on SSRS ceramic powder: a) 3-D plot picturing pinholes in electrolyte appearing after casting the electrode layer, b) light microscopy image, c) line profile of exemplary hole depth.

5.2.3 Conclusion

It was demonstrated that processing unreacted BZCY-721 mixtures as the base material for electrolyte half-cells is not feasible with the current slurry formulation, presumably due to the development of gaseous species. Hole formation only occurred when the second layer was applied, raising the question of whether the gaseous phase developed specifically upon contact

with the hydrogen electrode layer, or if the gas would have developed regardless and was simply trapped due to the overlaying tape. If the use of unreacted carbonate/oxide mixtures as electrolyte powders is desired in the future, further investigation is required to determine the exact mechanism behind the gas formation and its interaction with the second layer. This would presumably include the reformulation of the slurry composition. Therefore, the SSRS electrolyte powder was excluded from the scope of this thesis.

5.3 Dispersant Selection: Sedimentation Experiments

5.3.1 Background and Pre-Tests

After switching from in-house powders to purchased powders another issue was discovered. Although powder batch BZCY-721 22K2 was able to be cast with the original slurry composition, this was not the case for the following batch 22K4. Using slurries based on the 22K4 was not feasible due to the slurry's excessively high viscosity, preventing it from being poured into the reservoir. Initially, additional solvent was added to reduce the viscosity, resulting in a castable slurry after incorporating 40 g of solvent, which is ten times the initial amount. Adding a surplus of solvent to a slurry generally reduces viscosity but also decreases the solid loading, leading to insufficient densities after sintering. [It was hypothesized that excessive solvent evaporation during the two-day dwell time could have been the cause.

A new slurry batch with the same powder was prepared, but the viscosity was already excessively high immediately after mixing the plasticizer and binder, with no significant evaporation observed during the weighing process. This excluded solvent evaporation (MEK/Ethanol) as the cause of the increased viscosity. After that, another possible explanation was explored: the higher surface area of the new powder batch BZCY 22K4 (~5 m^2/g) compared to BZCY 22K2 (~3 m^2/g) at similar particle size distributions.

The initial slurry composition as introduced earlier was based on the composition used for conventional SOC, adapted with additional solvent to reduce viscosity. In the original publication, the dispersant was chosen on the sedimentation speed. [62,92] Since transitioning from yttrium-stabilized ZrO_2 to BZCY-based cells, the slurry composition was not reassessed using rheology measurements, specific surface areas, or particle sizes. However, the slurry composition should be specifically developed for a ceramic composition and to only be slightly adapted to accommodate powder batch differences.

Fully developing a new slurry composition would have exceeded the frame of this work. Therefore, a different approach was chosen. Several smaller investigations were conducted. The first countermeasure was to systematically investigate the dispersant type and amount in the slurry, as the increased surface area suggests a need for more dispersant.

The following experiment focused on the influence of the dispersing agent and its concentration on powder dispersion inside the solvent. The objective was to achieve a mixture that forms a densely packed powder bed. [65,66] The “best” performing amount being represented with the lowest powder bed after sedimentation.

Table 5-5: Dispersion mixtures and d_{50} after milling.

ID	Powder	Dispersant	Dispersant content [wt.-%]	d_{50} [µm]
1	22K4	N/A	0.0	0.73
2		Nuosperse FX 9086	0.5	0.76
3			1.0	0.67
4			1.5	0.63
5			2.0	0.65
6			2.5	0.65
7		BYK 220S	0.5	0.69
8			1.0	0.70
9			1.5	0.69
10			2.0	0.68
11			2.5	0.72
12	BZCY-625-20-175 + 0.5 wt.-% NiO	Nuosperse FX 9086	1.5	1.37
13	22K2 + 0.5 wt.-% NiO		1.5	0.85
14	21K1 as received		1.5	0.63
15	22K4 + 0.5 wt.-% NiO		1.5	0.60

5.3.2 Experimental Set-Up

The materials used in this study were: powder with the stoichiometry $BaZr_{0.7}Ce_{0.2}Y_{0.1}O_{3-\delta}$ (22K4), dispersants Nuosperse FX9086 and BYK 220S and solvent Methyl Ethyl Ketone/denatured Ethanol-mixture (66:34 wt.-% ratio). As a reference, three previously castable ceramic powders were included: 21K1, 22K2, BZCY-625-20-175 (in-house). The previously non-castable powder mixture of BZCY-721 22K4 + 0.5 wt.-% NiO was also included. The mass percentages and the dispersant types were varied according to Table 5-5. The sedimentation experiment followed a scaled down procedure as outlined by Mistler et al. [65] Detailed description in the supplementary information.

The cylinders were kept undisturbed for seven days. The height of the dispersion and the sedimentation layer was documented after filling and after the seven rest days. The heights were recorded with the help of a flashlight to enhance the separation line contrast. In addition to the heights, the clarity of the supernatant liquid was recorded.

5.3.3 Results and Discussion

The overall results of the phase separation for mixture 1 to 11 are shown in Figure 5-4 top) 30 min after filling and bottom) after seven days of rest. Mixtures 12 to 15 are not included in the diagrams because their settlement heights dropped below the lowest mark on the cylinder. After filling the cylinders, the reference suspensions (1 & 15) stayed uniform, not separating into multiple layers. Seven days later, reference mixture 1 (without dispersant) was clearly separated into two phases. However, the packed powder height was more than double that of the other mixtures. This observation suggests that the untreated powders flocculated after milling, which leads to a decrease in packing density and an increase in powder bed height. Mixture 15 was not readily analyzed due to the settlement height dropping below the minimal measuring height of the cylinder. Visual comparison between the suspension with the mixture

of equal dispersant concentration (mixture 4) showed that the settlement behavior and the clarity of the supernatant liquid were similar.

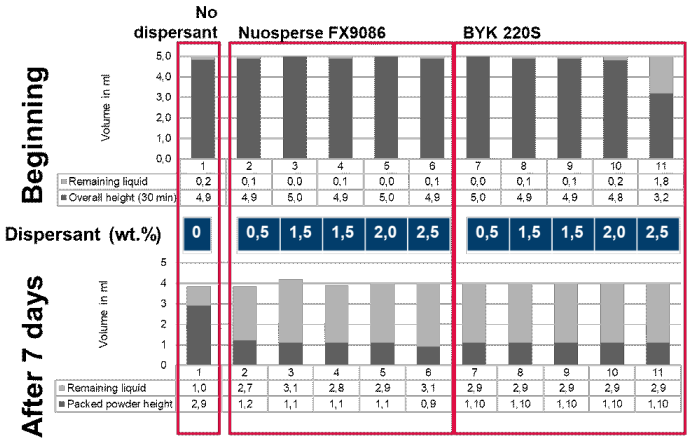

Figure 5-4: top) Powder sedimentation height approximately 30 minutes after transfer to the measuring cylinders; bottom) powder sedimentation height after seven days of rest.

After one week of sedimentation, the powder sedimentation height for most samples was quite similar, ranging from 0.9 to 1.2 ml. The significant difference in the samples was not the powder bed's height but the supernatant liquid's cloudiness. Mixture 6, for example, displayed the lowest powder bed height. However, it exhibited an additional gradient within the liquid. Mixture 3 showed a similar gradient between the 2- and 3-ml marks. Regarding the BYK series, the supernatant liquid generally turned clearer compared to the Nuosperse samples. This might suggest that the dispersants have a different particle-size cutoff. This cutoff decides if the dispersant makes the powder settle more densely or keeps the particles in suspension. [66]

Of the four additional mixtures (12-15), only mixture 13 appeared different. Here it was visible that the supernatant liquid was cloudier than the others. The mixture contained powder of smaller primary particle sizes (previously) deemed too small for tape casting. The sedimentation behavior of mixtures with BYK 220S was similar to that of Nuosperse. The most obvious difference was the cloudiness of the supernatant liquid. Right after filling the suspension in the cylinders, phase separation was observed in sample Nr. 11 (2.5 wt.-% BYK). The sedimentation started immediately and concluded in a clean separation between the liquid and the settled powder.

The PSD analysis (Table 5-5) established no significant difference between the particle sizes of different mixtures if they are based on the same ceramic powder. For all mixtures based on 22K4, the particle size distribution is monomodal and lies within $d_{10,min} = 0.32\ \mu m$ and $d_{90,max} = 1.72\ \mu m$ with the as-received powder exhibiting a bimodal PSD with $d_{10} = 0.51\ \mu m$, $d_{50} = 1.56\ \mu m$, $d_{90} < 45.07\ \mu m$. Table 12-2 in the supplementary section gives the particle sizes in more detail as well as the composition of the slurry.

It is important to note that the powder of BZCY-625-20-175 + 0.5 wt.-% NiO prepared in the same manner as the other in-house powders had the highest d_{50} value of 1.37 µm and the previously castable batch 22K2 of 0.85 µm, whereas the powder that was not castable had a d_{50}

value of 0.597 µm. This supports the assumption that the “non-pourable” quality of the slurry was the result of the difference in particle size.

Tape casting of full-composition slurries with adjusted dispersants: Based on these results, slurries with adjusted dispersant amounts were prepared following the standard procedure including plasticizers. The first slurry was prepared using 2.5 wt.-% BYK 220S as a dispersant (slurry 23-ES-2), and the second slurry had an increased Nuosperse FX 9086 amount of 2 wt.-% (slurry 23-ES-3). Even though the two complete slurries appeared to be homogenously mixed, the slurries were again not pourable. After letting the slurry rest for two days, the viscosity was even higher. In addition, slurry 23-ES-3 had developed bubbles on the slurry's surface, which contained non-dissolved binder. Slurry 23-ES-2 did not show this behavior but had an even higher viscosity. (As mentioned previously the viscosity was not measured for all slurry batches due to insufficient amounts.) Slurry 23-ES-3 was homogenized after adding 1 g MEK/Ethanol solvent mixture and an additional mixing step at 1000 rpm and 3 min using the Thinky mixer. During casting, bubble formation was observed, leading to discontinuities in the cast tapes. Slurry 23-ES-2 was only homogenized after adding 2.5 g of MEK/Ethanol mixture and two homogenization steps. The tapes were allowed to dry on the machine for 1.5 days to account for the increased solvent content, which slowed the drying process. The removal of both tapes from the carrier film proved difficult. Whereas previous tapes could be lifted off in one motion, both tapes tore in multiple locations during the removal. This showed that the changes to the dispersant content were not successful.

5.3.4 Conclusion

The experiment confirmed that both dispersants generally work for the given powder. The lowest packed powder height for Nuosperse was achieved with the highest dispersant concentration of 2.5 wt.-%. As this concentration is the highest of the here investigated concentrations, it is possible that the actual minimal powder bed would have been achieved at higher concentrations. The supernatant liquid at 2.5 wt.-% showed an additional gradient. Therefore, 2 wt.-% was used as dispersant content. All other powder bed heights of both dispersants were similar after the 7-day resting period. Therefore, the sedimentation experiment did not provide any distinct outcome as to which concentration would work best in a slurry. However, powder bed height is an indicator for the green density of a tape. Regarding the known difference in surface area of the new powder batch, it was decided to proceed with an increased amount of dispersant of both dispersant types.

In conclusion, neither the increase of the dispersant amount nor the switch to another dispersing agent resulted in castable slurries.

5.4 Solvent Variation in Simplified-Composition Slurries

5.4.1 Background and Motivation

The previous experiments showed that there remained open questions with regards to the slurry composition and the influence of the particle surface area on the castability of the slurries. The change to the dispersant did not solve this issue. To replace the full investigation into slurry development a different approach was chosen.

Returning to the initial development process as detailed by [62], two possible mitigation strategies were identified. The first was regarding the usage of a MEK/Ethanol mixture as solvent base. MEK was chosen by Schafbauer as a solvent component to modify and improve the drying behavior of the thick electrode tapes and to increase the viscosity. However, the non-castable slurries in the case of this thesis were those used for thin electrolyte tapes. Therefore, the addition of MEK was irrelevant with regards to drying behavior. Furthermore, omitting the MEK entirely and switching to ethanol-based electrolyte slurries might decrease the viscosity to a castable range. The second difference between the YSZ used in SOC manufacturing and the BZCY-721 in this thesis was their interaction with water. When adding YSZ to water the pH-value remains neutral (tested through pH-strip) whereas the BZCY-721 powder in water created a pH-value of >11. It is known that powders which react with water can form hydroxyl groups that greatly affect the rheology of a slurry. However, the effect is not the same in all systems because the actual nature of the interaction depends on the other components of the slurry. [63,66] Therefore, anhydrous ethanol was chosen as another possible solvent in addition to denatured ethanol.

To limit the possible influences of the additional organic components, in the first step, the composition of the slurries was chosen to be limited to solvent, ceramic powder and binder PVB. The second step was to determine which dispersant should be used for the best performing simplified-composition slurry of the first step.

5.4.2 Experimental Set-Up

This experimental series encompassed slurries made from a solvent (anhydrous ethanol, water-containing ethanol (>97 vol.-% alcohol, denatured), or MEK/Ethanol), ceramic powder (BZCY-721, Batch 22K4), and binder (PVB 98). The slurries were prepared with regard to the homogenization procedure as introduced in the initial procedure. In the second part of the experiment, PVB 98, Nuosperse FX 9086 or BYK 220 S were added as dispersants. PVB 98 acts as a binder in high concentrations but as a dispersant in low concentrations. [93] All slurries were cast using the manual tape caster to improve through-put.

5.4.3 Results and Discussion

Solvent selection (Figure 5-5): The first observation was that the slurry containing MEK/Ethanol was exceptionally viscous which made it non-castable. The dispersant Nuosperse FX 9086 had to be added to make the slurry castable. Neither of the two ethanol-based slurries showed similar issues. The ethanol-based slurries spread similarly well. The more severe cracking for the denatured ethanol might primarily be the effect of casting an increased slurry amount. The overall surface quality of the tapes was best for the anhydrous ethanol-based tape. However, both tapes showed clear signs of powder agglomeration. Therefore, the second section of the experimental series involved the addition of a dispersant to an anhydrous ethanol-based slurry.

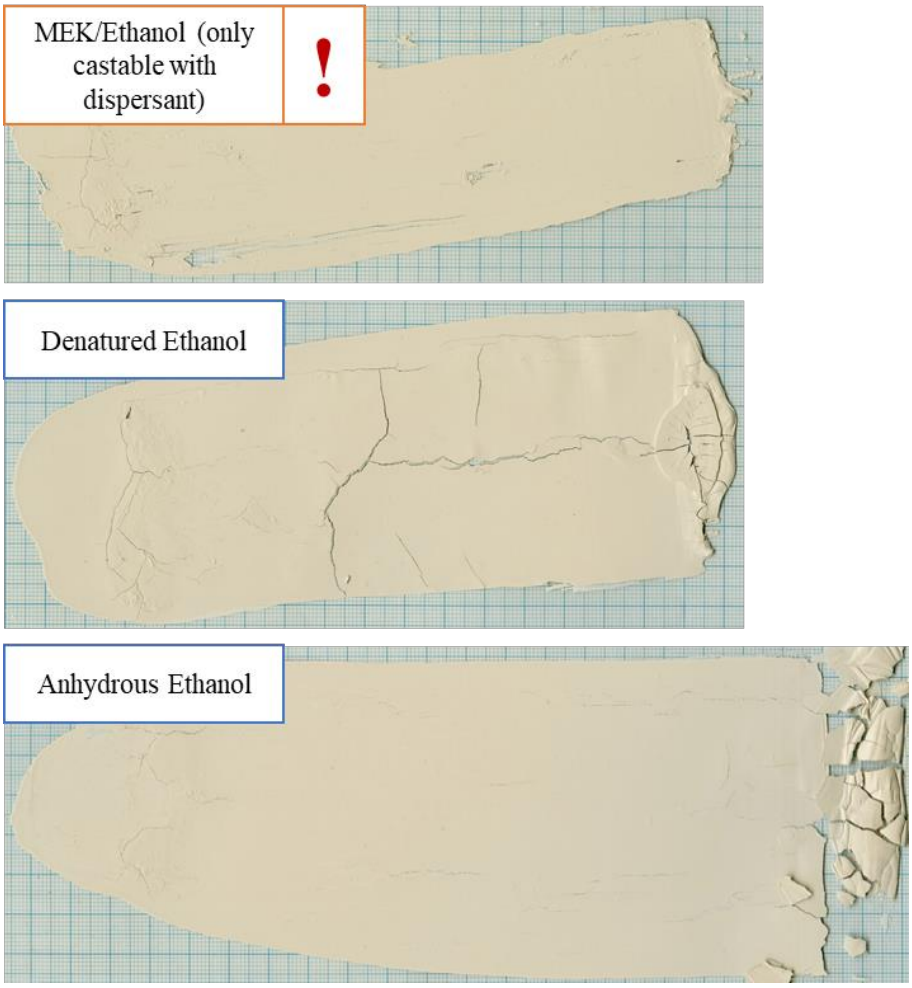

Figure 5-5: Impact of solvent on casting results for slurries composed only of ceramic powder, solvent, and binder without plasticizers (manually cast slurries, scanned).

Dispersant selection (Figure 5-6): The results show a clear difference in the tape quality concerning surface smoothness and crack formation. The crack formation is most pronounced for the PVB dispersant, followed by the BYK 220S containing sample. Therefore, Nuosperse FX 9086 was confirmed as the best-performing dispersant with regard to surface quality and crack formation. The proper amount of dispersant was already determined previously to be 2 to 2.5 wt.-%.

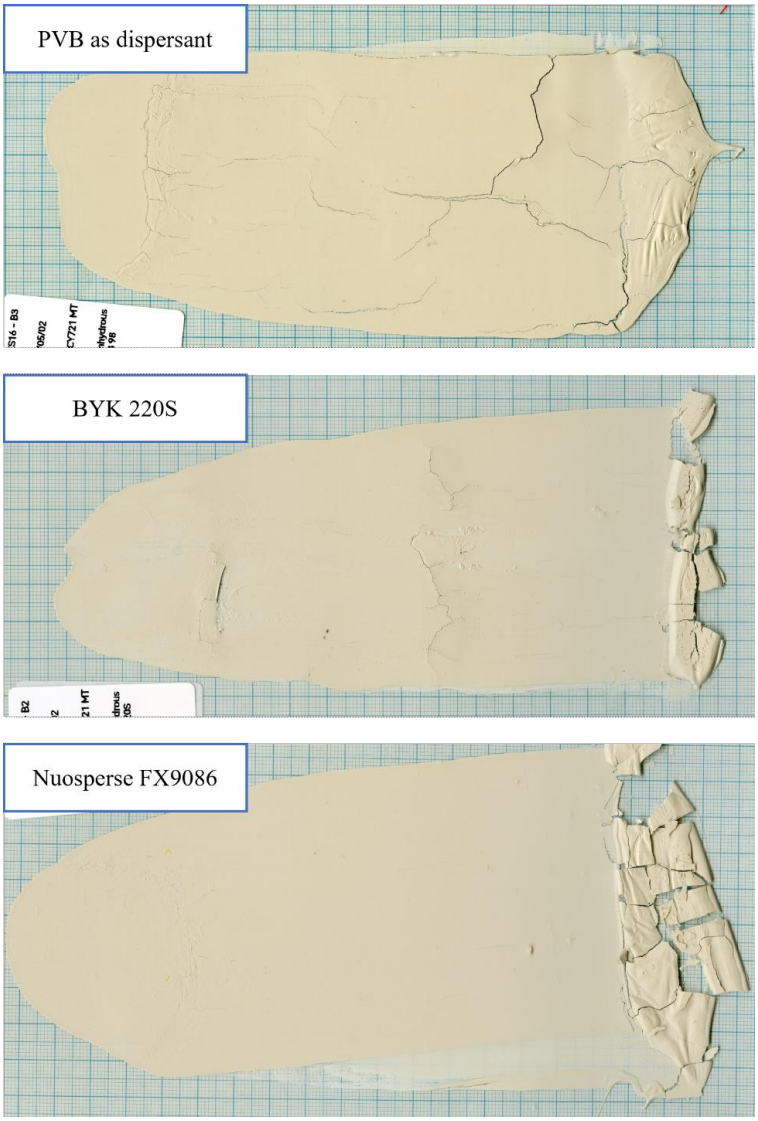

Figure 5-6: Impact of dispersant on casting results for slurries composed only of ceramic powder, anhydrous ethanol and binder without plasticizers (manually cast slurries, scanned).

5.4.4 Conclusion

It was found that the omission of MEK was a crucial improvement to the slurry castability (in simplified-composition slurries). The difference between the results of the anhydrous and denatured ethanol were small, however, the overall impression of the anhydrous ethanol-based tape was better with regards to surface smoothness. Nuosperse FX 9086 was confirmed as the best performing dispersant.

5.5 Empirically-Derived Slurry Compositions

5.5.1 Background and Motivation

All simplified-composition slurries tape cast in the experiments above showed a lack of flexibility and high brittleness. This is the reason for the use of plasticizers to improve green-tape flexibility. However, it was not clear what specific slurry formulation would produce the best results. Because of the limited time available, the slurry components where not varied in a full factorial experimental design. Rather, six different compositions were tested for which there was an empirically plausible reason for their suspected improved performance.

5.5.2 Experimental Set-Up

Table 5-6 lists the different empirically derived compositions. The first two compositions were using MEK/ethanol mixtures as solvents. The first one without a modification to the solid content; the second one with additional solvent to decrease the solid content from 25 vol.-% to 15 vol.-%. The next two compositions were those for which the solvent was entirely ethanol-based (denatured ethanol and anhydrous ethanol). The last two compositions varied the binder and plasticizer contents. Because of the observation of insufficient binder dissolution in previous experiments, one composition had a decreased binder content. The last composition was modelled after the currently used composition of the SOC manufacturing. The slurries were prepared following the initial procedure apart from the variation stated above. The casting was performed using the manual tape caster.

Table 5-6: Empirically derived electrolyte slurries with their specific features.

Slurry ID	Specific condition
23-ES-4	Reference composition (as introduced in the initial procedure)
23-ES-5	15 vol.-% solid content instead of 25 vol.-%
23-ES-6	Denatured, water-containing ethanol as solvent
23-ES-7	Anhydrous ethanol as solvent
23-ES-8	Decreased binder content (5 wt.-% instead of 7 wt.-%)
23-ES-9	Modified binder-to-plasticizer ratio Binder: Plasticizer I: Plasticizer II, 2 : 1.5 : 1.5

5.5.3 Results and Discussion

Figure 5-7 shows the overview of the casting results for all 6 empirically-derived compositions. The experiment confirmed that the reference composition 23-ES-4 and the reduced binder composition 23-ES-8 were not readily pourable. The slurries had to be “scraped” with a spatula onto the casting foil before being cast. The resulting tapes showed excessive streaks and general uneven thicknesses. In direct comparison, the reference composition performed slightly better than the composition with a decreased binder content. The tape produced from 23-ES-5 exhibited fractalized borders, indicating insufficiently low surface tension possibly due to the increased solvent amount. Such border behavior is inacceptable for a tape casting slurry because the slurry should not continue flowing in such an unrestricted manner after leaving the shear stress zone underneath the doctor blade.

Three compositions were found to be generally acceptable as basis for future slurry formulations. Both ethanol-based slurries, 23-ES-6 and 23-ES-7, demonstrated comparable

quality with smooth surfaces and good casting ability. The last sample utilizing the SOC-additive-ratio was found to be easily castable, however, it was thicker than the other tapes.

Figure 5-7: Impact of differently adapted slurry compositions on casting results. Manually cast slurries, scanned, color saturation digitally changed to enhance defect visibility.

Denatured ethanol was selected as the solvent for future tape casting for three reasons: (1) both experimentally-derived ethanol-based slurries showed qualitatively similar results; (2) denatured, water-containing ethanol is significantly less expensive than anhydrous ethanol; and (3) PVB 98 dissolves more easily in water-containing ethanol, as stated by the manufacturer.

5.5.4 Conclusion

The experiments demonstrated that the MEK-free, ethanol-based slurries yielded the best results. Minor differences are observed between anhydrous and denatured ethanol, leading to the preference for denatured ethanol. Agglomerates on the tape surface indicated the necessity of a dispersant. Therefore, various dispersants were tested. Nuosperse FX 9086 outperformed BYK 220S and PVB, making it the preferred dispersant. The results of the empirically-derived slurries showed that the composition used for 23-ES-6 is optimal for future tape casting slurries.

5.6 Transfer to Large-Scale Tape Caster

The scalability of cell production using the initial procedures encountered significant limitations. These limitations primarily stemmed from the quality of the tapes produced during the initial process. Defect-free areas were sparse, with an approximate defect density of one per

9 cm². This was manageable for smaller circular samples but highly restrictive for larger samples.

5.6.1 Initial Process Adjustments and Machine-Specific Scalability

Two major factors contributed to the scalability issues: the slurry quality and the machine-specific characteristics of the KaroCast tape caster. One major scalability issue lies in the amount of slurry produced. The standard amount produced to be tape cast successfully on the KaroCast is 10 – 14 ml. The absolute maximum amount of slurry prepared using the standard Thinky mixer route produces 24 ml of slurry (30 g ceramic powder). Significant amounts of slurry are lost to the milling balls. Therefore, crucial quality assurance methods like the viscosity measurement can only be done on batches specifically prepared for rheology measurements. Therefore, the procedure was adapted for larger amounts of slurry. Other key advancements included:

Dispersant content optimization: Increasing the dispersant content reduced the occurrence of agglomerates in the electrolyte layer.

Solvent change: Switching to ethanol as the electrolyte solvent ensured castability across different batches of powders, even when variations in particle size distribution or surface area were present.

Milling ball sieving: Implementing a sieving step for the milling balls before pouring the slurry eliminated the risk of milling balls falling into the slurry reservoir, which previously caused streaks in the tapes, significantly improving the available defect free sections of the tape.

Deairing process: With larger slurry quantities, gas bubbles could not sufficiently rise to the surface before casting. To address this, a deairing step was introduced approximately 30 minutes to one hour before casting each slurry.

These measures significantly enhanced the uniformity and quality of the produced tapes, reducing defects and variability in the final layers. Despite those improvements in slurry quality, several issues with the KaroCast machine limited scalability:

Manual rewinding and alignment issues: During sequential casting, the machine required manual rewinding of the carrier foil. This process increased the risk of misalignment, leading to inconsistencies in the layered structures.

Casting thickness limitations: The KaroCast could cast a maximum thickness of 800 µm. The machine's design featured an incline directly after the doctor blade, causing thicker electrode layers to flow downward along this incline. This led to thickness variations along the casting direction. To mitigate this issue, the carrier foil speed was increased as soon as the reservoir started emptying, allowing the tape to quickly reach the flat, high point of the machine for drying. However, this approach restricted the usable tape section to the flat segment—approximately 30 × 15 cm^2 —suitable for half-cell manufacturing.

Tape thickness variability across width: A persistent issue with the KaroCast was the variability in tape thickness across its width. This problem was ultimately traced to a defective micrometer screw used to set the blade gap height. Although this defect was not inherent to the

machine design, it significantly impacted the lamination process and underscored the need for a more reliable system.

Lamination requirements: The limited casting thickness necessitated the casting and lamination of single-layer electrode tapes. This doubled the required slurry preparation, casting runs, and machine occupancy per half-cell, further limiting scalability.

These combined limitations—both in slurry preparation and machine capability—highlighted the need for a more robust solution. The JuCast tape caster was selected as the primary system for scale-up efforts due to its advanced capabilities and potential to overcome the constraints identified with the KaroCast.

5.6.2 Transition to JuCast Tape Caster

The transition to the JuCast posed several challenges. The first was the necessary amount of slurry to be used during casting. It was found that using the optimized slurry preparation procedure as detailed above was sufficiently scalable for the electrolyte slurry. Therefore, the electrolyte process did not need further JuCast-specific optimization.

However, the electrode slurry required significant revisions to accommodate the larger slurry volumes demanded by the JuCast (min. 1 L). This included re-evaluating the mixing times, adjusting the dispersant ratios, and implementing enhanced deairing techniques to ensure uniformity in the larger-scale batches.

It became necessary to transfer to another homogenization device. Because of the lack of prior experience using this route for BZCY-based slurries, the procedure for conventional SOC-support slurries (NiO + YSZ) was used. The same percentages as in the initial procedure were maintained; however, the mixing steps required more time on the turbular mixer. Specifically, the binder dissolution took several hours longer than expected. The specific procedure can be found in the standard operating procedure in the supplementary information. The casting speeds were transferred from the initial KaroCast procedure.

5.6.3 Viscosity Measurements of JuCast Slurries

In this work, the increased volume of slurry prepared allowed for the first time the execution of viscosity measurements on the produced slurries. Figure 5-8 illustrates the viscosity as a function of shear rate for both electrode and electrolyte slurries. The viscosity assessments were conducted on two slurry formulations. The electrode slurry was characterized using a plate-on-plate setup, optimal for analyzing slurries with moderate viscosities and providing insights into shear-thinning behavior. Conversely, the electrolyte slurry was examined using a double-slit setup, chosen to accommodate the specific viscosity range and flow characteristics unique to this formulation.

The casting range, as illustrated in the figure, represents the variation in shear rate experienced by the electrolyte and electrode slurries during the tape casting process. These variations are influenced by the interplay between casting speed and blade gap. The data highlights that increasing the blade gap results in a decrease in shear rate, which subsequently increases the viscosity of the slurry. This relationship provides a plausible explanation for the observed differences in layer thickness between the KaroCast and JuCast systems. Specifically, the

reduced shear rate at larger blade gaps likely increased the effective viscosity of the slurry during casting. This change in viscosity could have altered the correlation between blade gap and the resulting wet film thickness, leading to discrepancies in layer uniformity and thickness across the two casting setups.

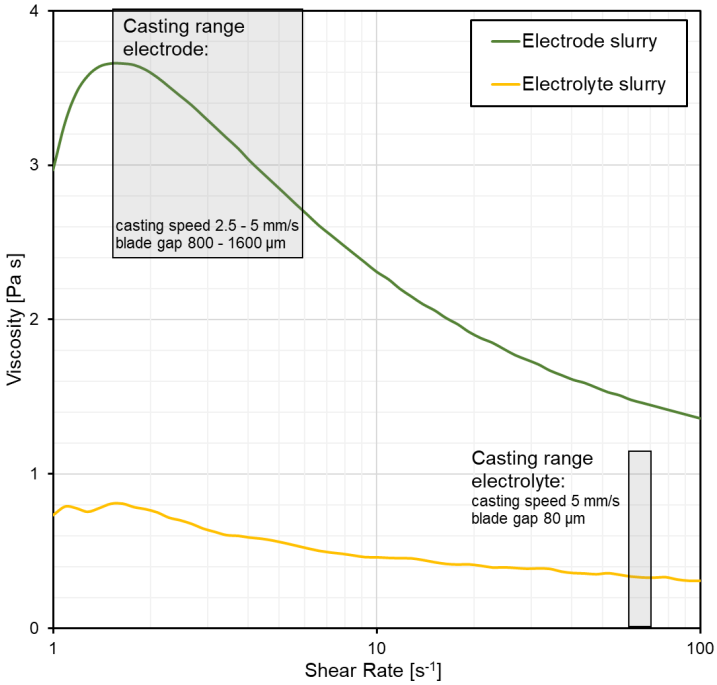

Figure 5-8: Viscosity of electrolyte and electrode slurries with highlighted tape casting ranges.

5.6.4 Comparison between bilayers cast on KaroCast vs. JuCast

This section examines the differences in cells tape cast using the KaroCast and JuCast machines. It includes a comparison of dried tape thicknesses, improved thickness variability, and Cyberscan topography measurements, highlighting the specific challenges associated with each process.

Table 5-7 shows the differences between the set blade gaps and the achievable tape thickness. Although it is known that the blade gap to dried tape thickness ratio depends on the specific device, the differences between the two machines are stark. For the electrolyte layer, the blade gap was set to 80 µm for both machines, as the electrolyte thickness was not supposed to vary between the KaroCast and JuCast. However, the achieved dried thickness was 14 µm for the JuCast compared to 20 µm for the KaroCast. Notably, the variability of the thickness using the JuCast was significantly improved. This improvement represents a major step towards improved scalability and comparability of different cells. For the electrode layer, attempts were made to increase the thickness by raising the blade gap to 1200 µm during the JuCast casting. Despite this, the achieved dried tape thickness was 272 µm for the JuCast, only slightly above the 260 µm achieved using the KaroCast.

Table 5-7: Comparison between blade gap height and resulting dried thickness using both types of tape casters.

	JuCast		KaroCast	
	Blade gap	Tape thickness	Blade gap	Tape thickness
Electrolyte (purchased BZCY-721, MEK free slurry)	80 µm	14 µm ± 1 µm	80 µm	20 µm ± 5 µm
Electrode (Standard slurry, BZCY-721 + 60 wt.-% NiO)	1200 µm	272 µm ± 5 µm incl. electrolyte	800 µm	260 µm ± 30 µm incl. electrolyte

The Cyberscan topography measurements revealed further insights into the surface characteristics of the tapes produced by both machines (see Figure 5-9). The figure shows two representative cells per bilayer before sintering from both the KaroCast and JuCast processes. The 3D plots were rendered using the same exaggeration factor; however, due to differing color attribution, the color bar is not included. Additionally, the line profiles share the same exaggeration factor to ensure consistency in comparison.

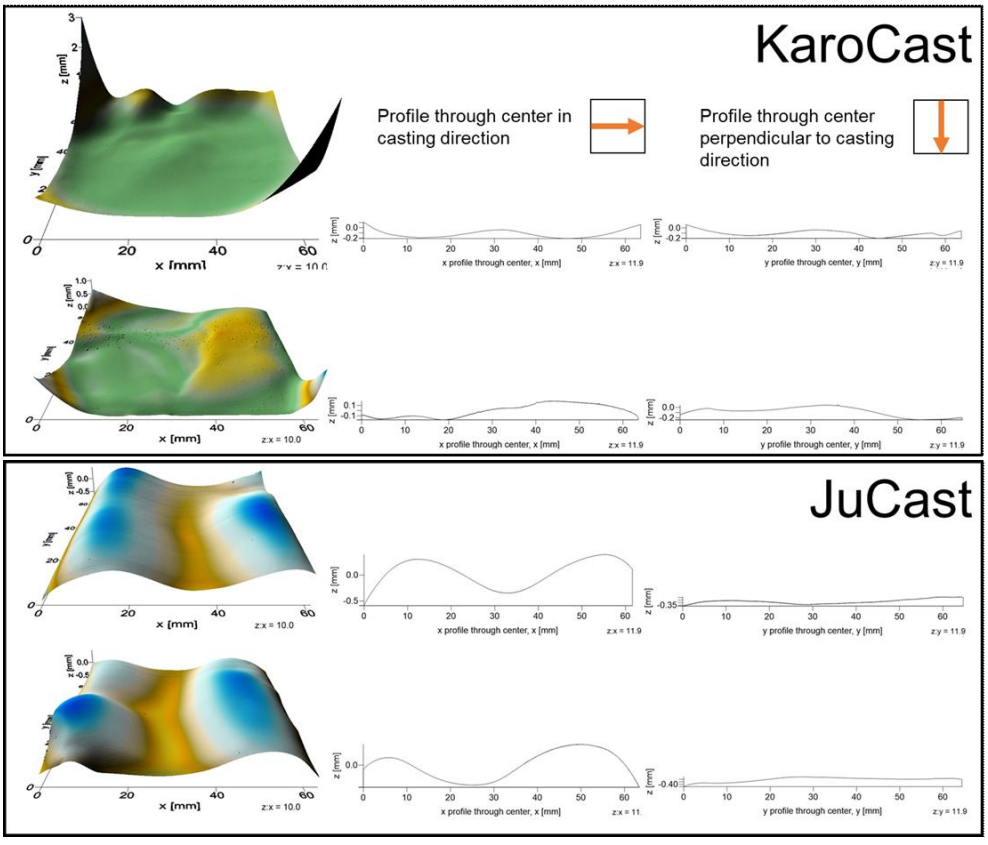

Figure 5-9: Topography measurements of two KaroCast and two JuCast samples. Cell 1, 3 and 4 show the measurement of the electrolyte side whereas the cell 2 is depicted with the electrode side facing upwards to illustrate the defects.

The first notable observation is the overextended corners in the KaroCast samples, reaching up to 3 mm in height. This is a common handling defect, as the corners serve as primary points of contact when manipulating these large cells. To a lesser extent, this defect is also seen in the JuCast samples. However, due to improved care during handling in the JuCast process, these overextensions were successfully minimized and are no longer as pronounced in the representative JuCast samples. This is a weak point which gained influence during upscaling of the cells. Smaller, round cells do not experience this issue due to geometric conditions.

The next observation relates to the surface structure of the cells. All cells exhibited excessive waviness, which was most pronounced in the JuCast samples along the casting direction. Perpendicular to the casting direction, the JuCast samples appeared much more even. In contrast, the KaroCast samples displayed a less regular structure overall. However, the differences between the two measurement directions were much smaller in the KaroCast samples compared to the JuCast samples.

When waviness is disregarded, a comparison of the surface qualities reveals additional differences. (Quantification of surface roughness was not possible due to the limitations of the measurement setup, which could not handle the large overall height differences in these samples.) The JuCast samples exhibited a distinct "groove" pattern in the casting direction, which was visible to the naked eye. This pattern likely originated from machining marks on the doctor blade. Despite this, the surface quality of the JuCast samples appeared significantly more homogeneous than that of the KaroCast samples. The latter showed less consistent surface characteristics, further underscoring the advancements achieved with the JuCast process.

The final observation relates to other defects present in the samples. In the second cell, the upper half of the cell surface is covered by small bumps. These bumps were consistently observed on all KaroCast electrode layer sides and might be attributed to gas bubbles, as the electrode slurry for the KaroCast casting run was not deaired. Additionally, topography measurements revealed agglomerates as another prominent defect in the KaroCast samples. In contrast, the JuCast samples exhibited far fewer defects. However, one notable exception was observed in cell three, which displayed a clear hole in the upper-right corner. This defect renders the cell unusable because of the non-gas-tight electrolyte.

5.7 Summary of Slurry Preparation and Tape Casting Improvements

This section outlines the challenges encountered and the significant improvements made during the slurry preparation and tape casting processes. Two major changes drove the developments in this area: the decision to switch to purchased powders and the optimization of slurry composition to improve tape quality.

The adoption of purchased powders enabled the preparation of much larger quantities of slurry. This switch to different ceramic base powders, however, pushed the slurry composition outside the processability window with regard to pourability, necessitating a reevaluation of the slurry formulation. Through systematic experimentation, MEK-free, ethanol-based slurries were identified as the most effective, with minor differences observed between anhydrous and water-containing ethanol. Denatured, water-containing ethanol was ultimately preferred due to its availability and usage in the electrode slurry composition.

Among dispersants tested, Nuosperse FX 9086 outperformed BYK 220S and PVB, remaining the preferred choice. The experimentally derived optimal composition for electrolyte slurries—featuring an increased dispersant content (23ES6) and denatured ethanol as the solvent—proved to be highly effective. This formulation set the standard for future electrolyte slurries used in the tape casting process.

All electrolyte slurries for subsequent experiments adhered to the improved composition unless otherwise specified. Substrate slurries cast on the KaroCast continued to follow the original procedure, using an MEK/ethanol solvent mixture. For substrate slurries cast on the JuCast, the same composition was employed, but the mixing procedure was adjusted to address the limitations of the Thinky Mixer for larger-scale homogenization.

The increased availability of powders also enabled the use of the large-scale JuCast tape caster, which necessitated adjustments to the slurry preparation procedure to accommodate the larger quantities. These changes included adapting the homogenization process and scaling up slurry production, which facilitated viscosity measurements that were previously infeasible. However, attempts to extend the thickness of the electrode layer to avoid laminating additional layers were not successful.

The combination of the JuCast and the improved slurry preparation route resulted in several advantages, including:

- Enhanced cell quality
- Reduced experimental effort per green cell
- Increased number of cells produced per preparation and casting run

6 Lamination and Cutting

This section addresses the joining of tapes through warm pressing as well as the precise cutting of samples into their final pre-sintering forms. This includes handling the fragile tapes, laminating multiple layers to form robust structures, and cutting them into precise shapes and sizes which account for dimensional changes due to sintering shrinkage. As determined in the previous chapter, the current hydrogen electrode layer cannot achieve sufficient thickness in a single casting step. To overcome this limitation, a bilayer tape is typically laminated with an additional single-layer hydrogen electrode tape.

This chapter outlines the initial methods and improvements introduced to optimize these steps while addressing potential challenges related to scaling the process for larger production volumes. Key aspects covered in this chapter include: strategies to prevent defects during lamination, introduction of the automatic cutting device, the impact of varying lamination parameters, lamination methods tailored for symmetrical cells, and the effect of the warm-pressing step outside the lamination function. By systematically addressing these topics, this section establishes a framework for optimizing the lamination and shaping stages, ensuring both the reliability and scalability of the manufacturing process.

6.1 Initial Lamination and Cutting Process

At this stage in the half-cell manufacturing process, the cast bilayer tape consisted of a thin electrolyte layer and a thicker hydrogen electrode layer, alongside a second single-layer tape made from the same material as the hydrogen electrode layer. The goal was to join the bilayer and the support layer through lamination using pressure and heat. Initially, a hole punch tool was used to cut circular samples from the tape. The diameter of the punch tool was chosen based on the availability of tape sections of sufficient quality to maximize the number of cells per tape (18 mm < d < 26 mm). First, defects in the electrolyte were visually identified, and the tape was then reversed to cut from the hydrogen electrode side. Then, discs with the same dimensions were cut from the single-layer electrode tape. Both discs were then stacked and placed between two protective polymer sheets to prevent adhesion and limit contamination before being inserted into the 4-pillar press. Initially, the samples were pressed at 9 MPa following the procedure outlined by Deibert und Ivanova. [6] Before the pressure was applied, the machine closed the distance between the two dies until only a small gap remained and the temperature rose to 80 °C to ensure uniform heating across the entire sample. Only after this equalizing step, which lasted 120 s, did the press fully close at a rate of 0.5 mm/s with a maximum force of 5 kN and increase the force to the set value within 30 seconds. The press then held the pressure for 120 s. After the holding period, the dies slowly released the pressure, returned to the starting position, and the samples were removed. This process commonly resulted in radial tears along the outer rim of the samples. To salvage these samples, discs of smaller diameter were cut, discarding the torn rim and retaining intact sections of the material.

6.2 Common Defects and Mitigation Routes

The success of the lamination process could be evaluated at several points throughout production. Several lamination defects are pictured in Figure 6-1 a) – e). Some defects were observable immediately after pressing, such as radial cracks (a), misalignment of the two discs

(c) and imprints from the polymer sheets or pressing die (b and e). These issues could often be attributed to suboptimal pressing parameters or handling errors. Other defects not pictured included inhomogeneous distribution of the pressure when multiple samples of different stacking heights or tapes with large thickness variability where pressed.

Some lamination defects, however, were not immediately detectable and only became evident during/after the sintering process (d). Samples with insufficient adhesion between layers frequently delaminated, while trapped air bubbles, which were initially invisible, became apparent as structural flaws after sintering. The trapped air defect also appeared to be more frequent with increasing cell sizes. These delayed manifestations of defects underscored the importance of careful monitoring and optimization during the lamination stage to minimize production losses and increase cell yield.

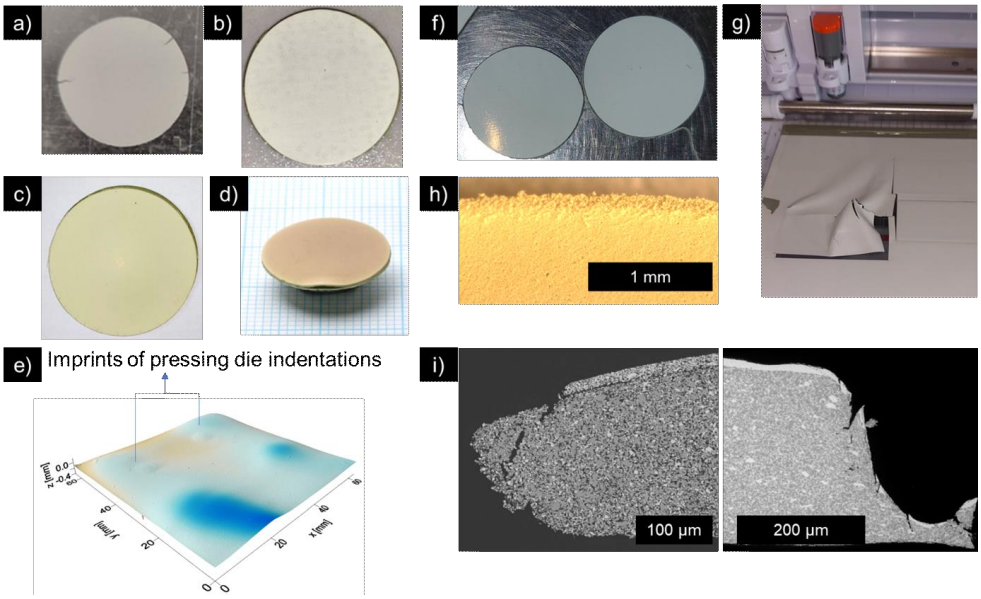

Figure 6-1: Lamination defects: a) radial tears due to over-pressing, b) circular imprints of polymer sheet, c) misalignment of sample discs, d) delamination visible after sintering, e) topography measurement of large-scale cells with imprints of defects of the pressing die. Cutting defects: f) deviation of ideal circular shape on the left and commonly occurring burrs on the right, g) machine caused ripping of tape due to insufficiently calibrated cutting parameters, h) coarse edges after sintering only observed in samples cut using hole punch, i) edge rounding in samples as seen using SEM caused through compression during shear-cutting.

The success of the cutting process could sometimes be immediately assessed right after cutting by observing the edge quality of the sample. The sample on the left of Figure 6-1 f) shows the deviation from the ideal circular form if the hole punch tool was not perfectly perpendicular during cutting underlining the severe influence of experimenter skill level, the sample on the right shows the common occurrence of cutting burrs. Removal of these burrs left coarse edges. Picture g) shows the effect of choosing incorrect cutting parameters and non-optimized patterns for the automatic cutting device in combination with cutting a thin bilayer with high thickness variability. The sample in h) shows the appearance of coarse edges after sintering which was

only observed after the sintering of samples cut using the hole punch tool. The cutting quality was generally influenced by the type and condition of the cutting tool as well as the skill of the experimenter. However, certain defects introduced during cutting, such as form deviations due to edge compression, only became apparent during microstructural investigation. In Figure 6-1 i) two different samples are shown which exhibited the defect of edge rounding which is a common defect in the shear cutting of plastic materials such as metal sheets. [94]

Several improvements are implemented to increase the sample yield by addressing these defects:

- The immediate adjustment to the process involved lowering the applied pressure to 7 MPa instead of 9 MPa. This change successfully prevented the occurrence of radial tears along the outer rim of the samples.
- Limitation of over-pressing through use of space holders (further details in the section on the variation of lamination parameters)
- Adapted sample placement within the pressing die to avoid die indentation imprints
- Reduction of experimenter influence through introduction of automatic cutting device

Another major improvement to the cutting process resulted from the achievement of defect-free tapes, made possible by advancements in tape casting. These high-quality tapes allowed for pre-sectioning into larger pieces before lamination without the need for carefully cutting around the tape defects, which significantly streamlined the workflow. By placing the cutting step after the lamination process, edge effects caused by material displacement during pressing or radial tearing were mitigated. This adjustment eliminated the need for redundant precision cutting steps, one before and one after lamination. Replacing the first precision cutting step by a minimal effort rough pre-sectioning cut. Laminated tapes also exhibited reduced thickness variation and enhanced stability, making them easier to handle and more suitable for precise cutting. These advancements significantly reduced the effort required for sample preparation while improving the overall reliability of the process.

6.3 Introduction of Automatic Cutting Device

The cutting process, while seemingly straightforward, is a crucial step in forming a green body from the tape cast layer. As introduced in the materials and methods section, three general approaches were employed during the course of this work, each with distinct advantages and limitations.

While the hole punch method as described above was effective for smaller samples, this method faced significant limitations when scaling up to larger cell geometries. Especially considering the high defect density in non-optimized tapes at the start of the thesis. Another drawback of the hole punch method was tool wear. The edge of the punch suffered significant abrasion due to the high force applied during cutting, leading to rapid degradation. Additionally, this approach was constrained to circular geometries, limiting its applicability for varied sample shapes. While it is feasible to manufacture custom pressing stamps for larger-scale production (as done for SOC manufacturing), this was not pursued in this work because the parameters for green body geometry, dictated through sintering shrinkage, were not fully defined. For larger-scale samples, an alternative approach involved manually cutting samples using a scalpel

guided by a pre-manufactured steel template. However, this method lacked precision and often resulted in uneven geometries and poor edge quality.

To address these shortcomings, a new automated cutting device (Silhouette Cameo 4) was introduced, significantly improving both shape flexibility and precision. Modifications to the standard cutting procedure as intended by the machine manufacturer included attaching the tape to the casting carrier foil through adhesive tape instead of using the self-adhesive cutting mats to eliminate cross contamination and damage to the tapes. Figure 6-2 a) pictures the cutting pattern which was optimized with regards to sample yield as well as corner and edge quality by incorporating cuts beyond the single cell geometry. Cutting two cells per cutting run was proven to be an ideal compromise between time saving, maximum lamination area and cut quality. The ability to produce samples with consistent geometries proved essential, especially for subsequent testing and evaluation.

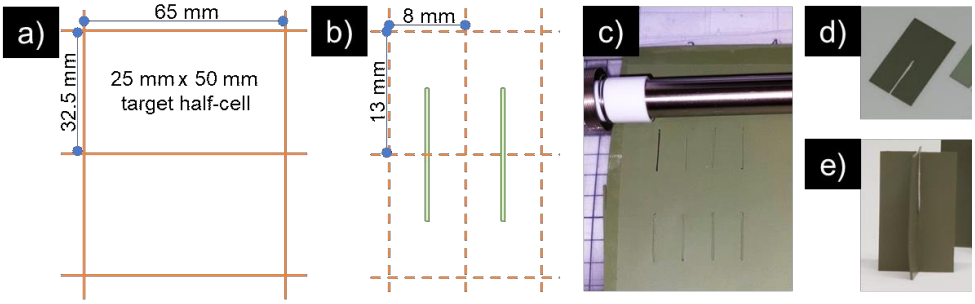

Figure 6-2: Cutting process using the Silhouette Cameo 4 automatic cutter: a) cutting pattern for improved edge and corner quality incl. double cell cutting to increase cell yield, b) cutting pattern for intricate patterns (Kirigami sample, see Chapter 7), green lines cut fully to avoid edge defects, orange line cut with less force to avoid tape tearing, c) picture of tape in cutting device between notch cutting step and cut of external borders d) sample pre-form and e) assembly.

Figure 6-2 b) – e) shows the extended capabilities by using an automatic cutting device. These samples were used for dilatometry measurements (further details in Chapter 7). The sample geometry was adapted from Mücke who characterized SOC materials. [95] In the original procedure, Mücke cut samples by hand after binder burnout leading to a very low yield of successfully prepared samples as well as posing significant health hazard by cutting non-matrix bound NiO powder. For optimal cutting of defect-free samples, the process was as follows: first, an oval interlocking notch was cut with a blade set to the appropriate depth to cleanly penetrate the tape. Subsequently, straight cuts are made to create a rip seam, allowing the sample to be separated from the surrounding tape with minimal force. The straight cutting edges extended beyond the sample's geometry to prevent displacement and damage during cutting.

6.4 Variation of Lamination Parameters

6.4.1 Background and Motivation

Several enhancements to the lamination process were initially tested empirically. To establish a more rigorous foundation, a systematic investigation was undertaken. The process parameters

chosen for variation were temperature, pressure, holding time and maximum allowed compression.

First, the set temperature of 80 °C may potentially be too low. This temperature was only slightly above the glass transition temperature of the binder PVB (72 °C-78 °C) [96], which is the minimum temperature required for successful lamination. Setting the press to only 80 °C raised concerns that the core of the specimen between the dies may not reach this temperature uniformly. Second, the observed crack patterns suggested that the yield strength of the PVB binder may have been exceeded during lamination, despite measured yield strengths of various PVB types exceeding 10 MPa. [97] However, deformation during the pressing process introduces more complex stress distributions than those observed in simple tension tests. Third, cracks may form if the maximum total compression tolerated by the tapes is surpassed.

To enhance experimental efficiency, Design of Experiments (DoE) was employed to plan and evaluate the experiments. [98] The objective was to streamline experiment execution, reduce the number of experimental runs, and enhance the quality of outcomes.

6.4.2 Experimental Set-Up

The investigated parameters were on the one hand given by the already used settings as well as from additional literature research. [6,62,95] The warm-press utilized is the 4-pillar laboratory press. The starting operational parameters included applying 7 MPa pressure for 120 s at a temperature of 80 °C. The maximum compression is not actively controlled.

Figure 6-3 shows the solution to limit over-pressing of the samples during lamination. Multiple metal sheets of defined thickness were inserted between the protective polymer sheet surrounding the sample. Through this the maximum compression was limited. This method of employing space holders has been documented for SOCs by Schafbauer. [62]

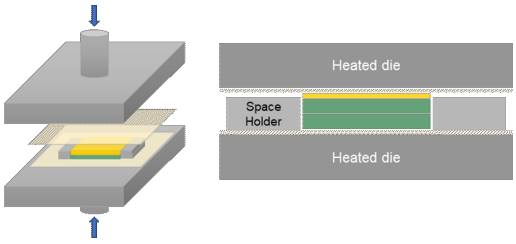

Figure 6-3: Set-up for improved lamination using space holders after Schafbauer. [62]

The preliminary assumed optimal operating settings (central experimental values) are 85 °C, 90 s, 6 MPa and a 10 % maximum compression of the tape. To find the actual optimal parameters, two reasonable values are chosen as minimum and maximum. Table 6-1 summarizes the different temperature, pressure and allowed compression values.

Table 6-1: Parameters for lamination experiments.

	Time in s	Temperature in °C	Pressure in MPa	Allowed compression in % of initial thickness
Minimum	60	80	4	5
Center	130	85	6	10
Maximum	200	90	8	15

A complete permutation (full factorial experimental design) of all possible variations would have required 81 experimental runs. Assuming the optimal combination falls within the interval defined by the maximum and minimum values listed above, the middle values were treated as center experiments within this range. To further reduce the number of variations, the fourth parameter of "allowed compression" was not independently chosen, reducing the necessary experiments to 10 runs (fractional factorial experimental design). The different values were encoded as -1, 0, 1 for minimum, center and maximum value, respectively. The compression value was always calculated by multiplying the other three encoded parameters. [98] The runs are listed in Table 12-4 (supplementary figure), with their order randomized to mitigate potential effects related to order or time. Each run involved four 26 mm circular tape cutouts: two of 800 µm single-layer electrolyte tape and two of 800 µm single-layer electrode tape. Initially, the thickness of each disc was measured at three points. Discs with measurements differing by more than 30 µm were excluded from the experiment. The remaining discs were then ordered by thickness, and matching pairs of electrode and electrolyte discs were selected to ensure the equal distribution of force over both disc pairs. To minimize the impact of tape thickness variation, the two pairs with the closest combined thickness were matched. The order of specimens was randomized. The primary target value was planned to be the density after sintering as determined by SEM analysis. A secondary target was the reduction in thickness, and diameter.

Before each experiment, the total thickness of the two discs were recorded. For each run, the height of the space holders was determined anew. The average thickness of the two specimen pairs served as the reference point for setting the height of the space holders. Three types of space holders were available: 300 µm metal strips, 100 µm metal strips, and 15 µm aluminum foil. These were matched to achieve the target thickness for each run. Due to variations in tape thickness, the maximum compression allowed by the space holders differed slightly from the target value listed in Table 12-4.

After lamination, the samples were sintered on MgO setter plates using the standard program: ramping at 0.5 K/min to 900 °C, followed by 2 K/min to 1500 °C, holding for 3 hours, and then cooling at 2 K/min to room temperature.

6.4.3 Results and Discussion

The first immediate result was the direct improvement of radial tearing. The tears only occurred in three samples. The commonality among those was that the compression exceeded the 15 % maximum.

Even though the change in diameter was tracked before and after the pressing, it had to be interpreted with a low level of certainty. This is due to the fact that during placement of the specimen in the pressing die and/or during pressing the discs slightly moved and were not perfectly centered. This led to inaccuracies of the diameter measurements as the overhang artificially increased the diameter (compare Figure 6-1 c)).

The comparison of the maximum compression and the observed thickness decrease reveals the paradoxical phenomenon that some samples appeared to have decreased in thickness beyond their maximal compression (Figure 6-4). This occurred most prominently in the samples with limited compression below 10 %. One possible explanation is the expansion of the tape during

heating and subsequent shrinkage during cooling exceeded that of the metal space holder strips. Above the 10 % threshold the achieved thickness consistently lay below the expected thickness.

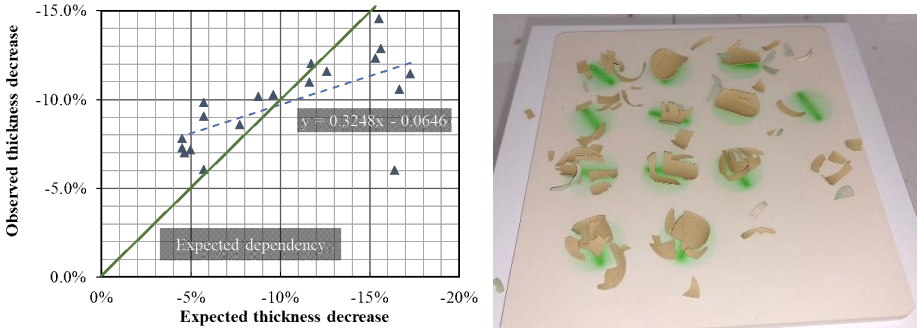

Figure 6-4: left) Comparison between observed thickness decrease and expected decrease, right) fracture after sintering of the two-layer laminates.

Another favorable outcome of this experiment was the increase in evenness in the tapes. The standard deviation of thickness within a sample decreased for 18 out of the 20 samples. This is important because local variations in thickness are assumed to cause warpage. It can therefore be concluded that using the warm press could be used to improve the overall quality of the cells by reducing the thickness variability. Even in cases for which there is no two layers to be joined it could still be favorable to warm press to improve the overall thickness gradient.

The specimen's camber during sintering was so different for the two layers that all specimen without exception broke (Figure 6-4 right)). Therefore, the final evaluation with regards to the influence of the parameters on the final density was not conducted. One observation was that the broken pieces were found everywhere inside the furnace. Where they touched the furnace insulation, no traces of nickel diffusion were visible. This fact suggests that at the time of the deposition of these pieces on the insulation, the temperature was comparatively low and it must have taken place during cool down because experience shows that nickel in direct contact with the furnace insulation at 1550 °C would cause discoloration of the furnace lining.

6.4.4 Conclusion of Lamination Parameter Variation

In conclusion, the results of this experiment were incomplete as the initial experimental design was flawed with regards to the chosen sample geometry of two thick single-layer tapes. This large differential thermal expansion behavior of both layers led to the fracture of all samples which did not allow for an in-depth investigation of potential influence of warm-pressing on microstructure evolution.

However, several important insights into the improvement of the lamination process were found, namely the limitation of the maximum compression to 10 % using the space holders. None of the samples at this maximum compression or below showed sign of delamination therefore any combination of the parameters is sufficient for future use. It was shown that the matching of the cell heights may have had a large beneficial influence next to the addition of space holders with regards to radial tearing.

The transferability of these observations to the bilayer-single-layer-electrode assemblies is limited with regards to the following: The actual local composition of each tape depends on the powder/binder interaction. Therefore, the plastic deformation behavior is also dependent on the powder inside the tape. Lamination of a thicker single-layer electrode onto a bilayer as is the case in the standard half-cell assembly might produce slightly different results as the ones in this experiment.

For the future cell preparation process, the pressing parameters were fixed at 85 °C, 7 MPa, 120 s holding time and 10 % maximum compression using space holders. In addition to this, it was beneficial to match the thicknesses of joined sample pairs to ensure homogeneous distribution of the pressure when laminating multiple samples.

6.5 Lamination of Symmetrical Cells

6.5.1 Background and Motivation

In the literature, electrode materials are commonly characterized in the following manner: the electrolyte is pressed to form a pellet and subsequently sintered. [99] The electrode powder is then mixed with specific binders to create a paste, which is either screen printed or applied by brushing onto the sintered pellet. The advantage of this method lies in its simplicity. However, a significant drawback is that it does not consider how the processing route and its parameters affect the material's microstructure. For instance, an electrode layer applied via screen-printing will exhibit a different microstructure compared to one produced through tape casting. This difference in microstructure can substantially influence electrochemical performance, e.g., through differences in porosity or percolation.

Another critical issue arises from the interface between the electrolyte and electrodes. The quality of adhesion between sequentially tape cast layers will differ significantly from that of a screen-printed layer on top of a pressed pellet.

6.5.2 Experimental Set-Up

Due to the challenges encountered during pellet production, an alternative approach was developed for preparing symmetrical cells. Figure 6-5 illustrates the schematic setup for symmetrical cells based on tape cast electrolytes. The symmetrical *hydrogen* electrode cells using tapes were created with four variations, i.e., i) Su + El|Su, ii) Su + El (thin) + Su, and iii) Su + El (thick) + Su, iv) Su|El + El|Su. For symmetrical *steam* electrode cells, two approaches were explored. The first involved an electrolyte support layer based on El (thick), while the second attempt used multiple layers of folded El (thin).

Lamination was carried out with the parameters: 80 °C, 7 MPa, 120 s holding time without compression limit. After lamination, the samples were sintered on MgO setter plates using the standard program: ramping at 0.5 K/min to 900 °C, followed by 2 K/min to 1500 °C, holding for 3 hours, and then cooling at 2 K/min to room temperature.

Su + El|Su: The pressing program employed was identical to the initial process described above used for laminating the supporting layer with the bilayer. Instead of adding an additional layer of the same diameter on the electrode side, a cut-out square was placed on top of the electrolyte side of the bilayer. These squares were cut to a side length of 11 mm to compensate for

shrinkage during sintering, aiming to achieve a final 1 cm² electrode area. In a second attempt, samples were prepared by warm-pressing two rectangular sections of bilayer and single-layer electrode tape, with final sample cutting conducted after pressing rather than beforehand.

Su|El + El|Su: As the second approach above.

Su +El (thin) + Su: All three layers were single layer tapes. Due to the fragility of the thin electrolyte tape the handling was only conducted by transferring the tape with the use of double-sided adhesive tape directly onto a single layer electrode tape. Then the third layer was added on top. A pre-section (~25 cm^2) was then laminated and cut into square cells.

El(thick): Two single layer electrolytes laminated together.

El(thin) folded: Thin electrolyte tape folded to achieve 16 layers, laminated as usual.

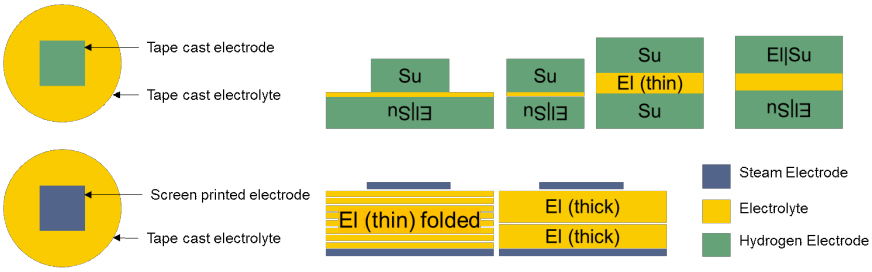

Figure 6-5: Alternative designs for symmetrical cells; top row) set-up consisting of three tape cast layers for hydrogen electrode symmetrical cells; bottom row) electrolyte supported steam electrode symmetrical cells based on thick electrolyte tape or multilayer thin electrolytes.

6.5.3 Results and Discussion

Hydrogen electrode symmetrical cells

Su + El|Su: Figure 6-6 illustrates the resulting laminated samples. Several adjustments to the pressing process were made, concluding that no single pressure setting was simultaneously low enough to prevent crack formation and high enough to ensure effective lamination. The asymmetrical shape of top and bottom were determined as cause of failure due to inhomogeneous pressure distribution and material flow.

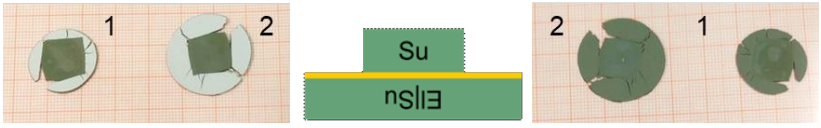

Figure 6-6: Lamination of square single layer electrodes onto bilayer, Su + El|Su-configuration, with two different diameters (Sample 1: d = 18 mm, sample 2: d = 24 mm). left) Top view, right) bottom view.

The adjustment to using square cuts for both tapes resulted in more promising pressing outcomes, as evidenced by the absence of corner cracking in the tapes. However, these samples did not sinter successfully, experiencing splitting along the electrolyte plane. Figure 6-7 left) displays the outcome of this approach.

Su|El + El|Su: These samples appeared flat after sintering. However, during handling they were readily delaminated at the El|El interface. This led to two flat half-cells per laminated pair. This favorable outcome was the reason for using this set-up to investigate its potential for warpage mitigation of full cells described at the end of this chapter.

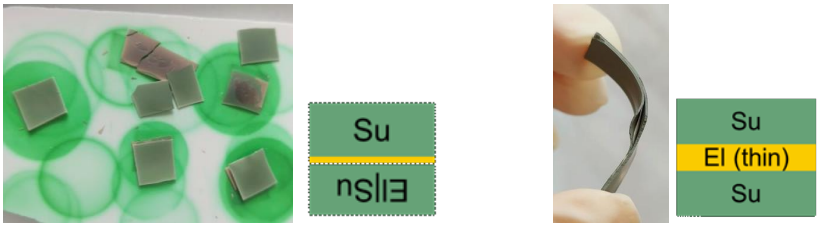

Figure 6-7: left) Symmetrical laminates containing a thick electrode layer and bilayer after sintering (Green color of setter plate due to previous sintering of round samples) Su + El|Su-configuration; right) failed lamination of two single layer electrode and a thin electrolyte layer, Su + El (thin) + Su-configuration.

Su + El (thin) + Su: The image on the right-hand side of Figure 6-7 highlights one issue of the third approach: delamination after warm pressing between the thin electrolyte layer and two thick electrode single layers (Su + El (thin) + Su-configuration) due to thickness differences within the electrode layer. This was the result of not being able to pre-section the layers due to the fragility of the electrolyte tape. It was therefore required to laminate a larger area which increased the risk of thickness variations. However, samples which were successfully laminated and sintered were also those of the Su + El (thin) + Su structure. As expected from literature, the symmetrical three-layer structure appeared to mitigate warpage. [100]

Despite the intact appearance after sintering, the cell did not remain intact. Figure 6-8 shows SEM analysis revealing crack formation at the electrode-electrolyte interfaces. The depicted cell was planned to undergo electrochemical testing; however, the electrode-electrolyte interfaces were major weak points leading to mechanical failure of the cell during in-situ reduction. As can be seen from the image on the right, the electrolyte layer never fully densified in this cell configuration, sintering shrinkage being potentially hindered because the electrolyte was fully constrained by the electrodes on both sides.

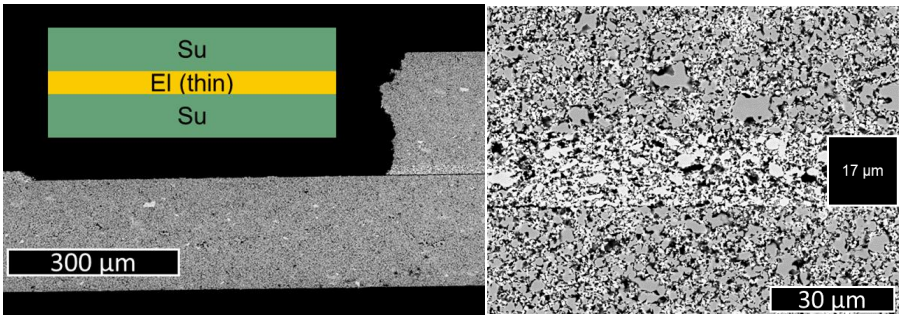

Figure 6-8: Delamination during in-situ reduction of symmetrical cells, left) delamination on the left between the electrode and the electrolyte interface of the top layer and on the right-hand side between the electrode and the electrolyte of the bottom layer, right) 17 µm thick electrolyte layer with severe porosity.

Steam electrode symmetrical cells

El + El: As stated above, two different approaches were undertaken for creating electrolyte supported cells. The results are presented for laminating two thick layers of electrolyte tape together as well as multiple thin electrolyte layers laminated together. As depicted in Figure 6-9, these samples exhibited significant warping, rendering them unsuitable as electrolyte supports for screen-printing. It is important to note that this warpage occurred even in the absence of a second electrode layer during sintering, indicating that the multi-material characteristic of the bilayer itself is not solely responsible for the observed warping.

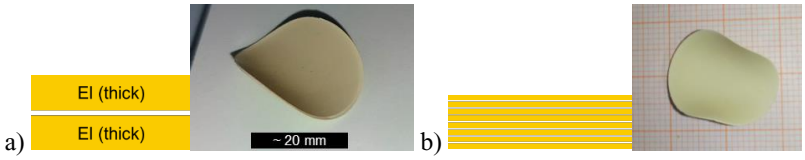

Figure 6-9: Schematics and photographs of a) warped two-layer electrolyte sample, b) warped multi-layer electrolyte.

Attempts were made to mitigate this warpage by adding a thin (5 mm) setter plate onto the sample weighing approximately 50 g during the sintering of four samples (~ 0.23 kPa). However, this resulted in crack formation approximately 1 mm away from the edge. Decreasing the pressure by choosing thinner setter plates was found to result in the warpage of the setter plates.

6.5.4 Conclusion of Lamination of Symmetrical Cells

Hydrogen electrode symmetrical cells: The lamination of symmetrical cells was found to be unfeasible without substantial modifications to the processing route. Among the configurations tested, the most promising was the Su|El(thin)|Su setup. However, even samples that appeared structurally intact after lamination exhibited insufficient densification post-sintering, rendering them unable to endure electrochemical measurements. General feasibility of this variation was, however, demonstrated by Pirou. [100]

Pirou showed that mechanical failure could be mitigated through immediate reduction following sintering. While this approach proved successful in their study, its applicability to the tapes presented here is doubtful due to the persistently low electrolyte density. The inadequate densification observed in these samples would likely undermine the stabilizing effects of immediate reduction, emphasizing the necessity for further optimization of both the sintering and densification processes to ensure structural and functional integrity.

A key finding from these experiments provided valuable insights into developing a warpage mitigation strategy for large-scale full cells. The symmetrical lamination of El|Su bilayers consistently resulted in clean delamination at the El|El interlayer, leaving two flat half-cells. This outcome highlights the potential utility of symmetrical lamination not only for structural purposes but also as a means to achieve uniformity and dimensional stability in the production of full cells.

Steam electrode symmetrical cells: The preparation of flat tape cast electrolytes was unsuccessful. As the pellet pressing process was successfully improved to produce pellets of

sufficient quality by the end of this study, further investigation into using tape cast electrolyte-supported symmetrical cells was discontinued.

6.6 Influence of Low-Temperature Heat-Treatment

6.6.1 Background and Experimental Set-Up

The waviness observed in samples cast on the JuCast raised the question of whether heat application alone could reduce this waviness by allowing the polymer to flow and smooth out when heated above its glass transition temperature. To investigate this, the lamination procedure described earlier in this chapter was adapted: bilayer samples were placed in the machine without applying force, isolating the effects of heat-treatment. To compare the influence of the standard procedure (pressure + heat) versus heat-treatment alone on polymer deformation, additional samples were processed under the standard lamination conditions (85 °C, 7 MPa, 120 s holding time with a 10 % compression limit). This comparison provided insights into the role of pressure in mitigating surface irregularities.

6.6.2 Results and Discussion

Figure 6-10 left) shows the initial topography measurement and the measurement after the heat-treatment without the application of pressure. As expected, subjecting the cell to a heat-treatment above the glass transition temperature of the binder allowed the cell to settle under its own weight and reduce the maximum distance between peak and valley by ~ 24 %.

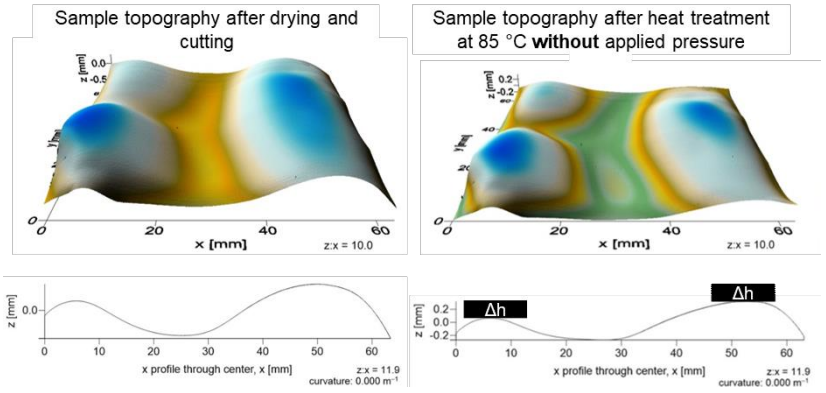

Figure 6-10: Topography measurement of tape cast bilayers using the JuCast, left) untreated sample, right) heat-treated sample without contact to the upper die.

Figure 6-11 illustrates the initial measurement (left) and the measurement after pressing (right). The initial warpage present before treatment was successfully eliminated. The overall reduction of maximum peak to valley distance was reduced by ~ 89 %.

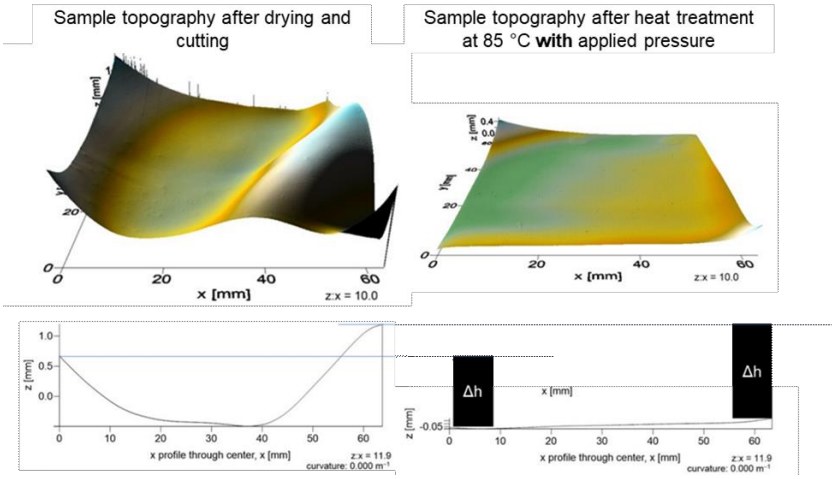

Figure 6-11: Topography measurement of large-scale bilayer sample, left) before and right) after heat-treatment with contact to the upper die.

6.6.3 Conclusion: Low-Temperature Heat-Treatment

The comparison between heat-treatment alone and warm pressing revealed critical differences in their effectiveness for mitigating sample waviness. While heat-treatment without applied pressure slightly reduced the excessive waviness of the samples, it failed to produce the desired flatness. The general wave form of the surface was preserved, indicating that heating above the glass transition temperature combined with gravitational influence was insufficient to fully smooth the surface.

In contrast, warm pressing demonstrated a clear advantage in addressing this issue. By applying pressure in addition to heat, the waviness was effectively mitigated, resulting in significantly improved flatness. This finding underscores the necessity of incorporating warm pressing into the process to achieve optimal surface quality and dimensional stability in the samples. Even if this means accepting defects introduced during the warm-pressing process as unavoidable.

6.7 Summary of Lamination and Cutting Process Improvements

The lamination and cutting processes underwent significant refinements during the course of this work, resulting in a more efficient and reliable methodology for producing green bodies. Several key changes were introduced to optimize both the lamination and cutting stages, addressing critical challenges and improving overall process consistency.

In the lamination process, the applied pressure was reduced to 7 MPa, which effectively minimized the occurrence of radial tears. Furthermore, the compression during lamination was limited to a maximum of 10 % of the initial sample thickness, ensuring better dimensional stability and reducing defects caused by excessive deformation. To achieve uniform force distribution during pressing, it was essential to use samples with identical total thicknesses when laminating pairs of samples. These measures significantly improved the adhesion between layers and the structural integrity of the laminated assemblies.

Whenever feasible, lamination was conducted prior to the cutting step, streamlining the workflow by eliminating redundant cutting stages before and after lamination. Cutting thicker, laminated assemblies also resolved issues of misalignment between the individual tape layers, further enhancing the quality of the final samples.

For the cutting process, the adoption of an automated cutting device proved highly beneficial. This device offered improved edge and corner quality, enhanced geometric precision, and the flexibility to create samples of varying shapes and sizes to meet different project requirements. These advancements not only reduced manual effort but also ensured consistency and repeatability across batches.

For long-term process development, two potential strategies warrant evaluation. First, the use of a multi-cavity pressing die or stamp could increase throughput and ensure uniformity in sample geometry directly during the lamination step. Second, modifications to the automated cutting device to enable in-line cutting could further enhance scalability and efficiency. These future improvements would support larger-scale production while maintaining the quality standards established in this work.

In summary, the integration of these process optimizations has greatly improved the lamination and cutting stages, contributing to a robust and scalable method for producing high-quality green bodies.

7 Binder Burnout and Sintering

This section focuses on the heat-treatment of the green bodies prepared as described above. Heat-treatment involves subjecting the green body to elevated temperatures and consists of two distinct stages: binder burnout and sintering.

Binder burnout involves the removal of non-ceramic powder components from the green body, including binders, dispersants, plasticizers, residual water, and solvents. Given that a significant portion of the green body's volume consists of these additives, binder burnout is a critical stage in the manufacturing process. Only after successful binder burnout can the powder particles consolidate during sintering to form a dense, cohesive body.

Typically, there are two approaches to heat-treatment: both stages can be conducted within a single furnace run, or binder burnout and sintering can be performed as separate steps. Initially, this work followed the procedure outlined in the ProtoMem project, which integrates both stages into a single furnace run.

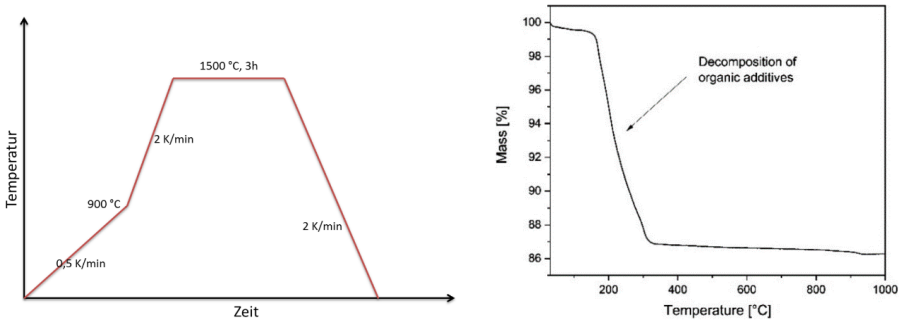

Figure 7-1: left) Binder burnout and sintering schedule used in the ProtoMem project, right) thermogravimetric measurement of NiO/$Ba_{1.015}Zr_{0.625}Ce_{0.2}Y_{0.175}O_{3-\delta}$ green tapes in air, heating rate of 5 K/min. [4]

7.1 Initial Heat-Treatment Process and its Shortcomings

The initial process was adapted from Deibert et al. [4] Samples (circular half-cells) were positioned on MgO setter plates with the hydrogen electrode facing downwards and subjected to heating in a muffle furnace under static air conditions. The heating schedule is outlined in Figure 7-1 left), commencing with a binder burnout phase (0.5 K/min up to 900 °C), followed by ramping to the isothermal sintering temperature (2 K/min to 1500 °C, 3 h), and concluding with a controlled cooling rate of 2 K/min to room temperature to accommodate for any mismatch in thermal expansion coefficients.

Figure 7-2 shows the SEM micrographs of two different cell batches to visualize the low quality of the initial cell and the impact of changing to purchased powder. Figure 7-2 left) depicts the top view and the cross-sectional microstructure of the electrolyte layer of the first half-cells prepared by the initial process. As open porosity is clearly visible across the electrolyte layer, it is evident that the electrolyte is not gas-tight.

Figure 7-2 (right) depicts a half-cell for which purchased powder of smaller particle size (BZCY-721 22K2) is used for the process with the heat-treatment kept the same. When using this powder, it was possible to obtain a sufficiently dense electrolyte. However, on a macroscopic scale, the electrolyte delaminated in large parts from the underlying electrode layer. Both cells were representative of all cells from these two production cycles.

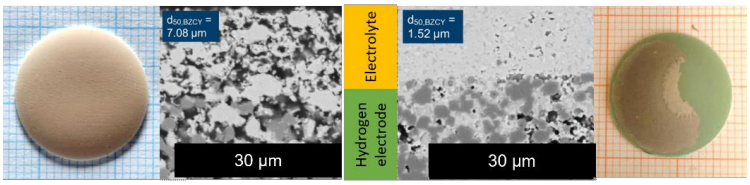

Figure 7-2: left) Cell of the first batch of sintered half-cells without process optimization, right) exemplary cell with increased electrolyte density after changing from in-house powder to using purchased powder BZCY-721 Batch 22K2.

Quantitative analysis was conducted using the image analysis software Fiji. [101] The line interception method revealed an electrolyte porosity of 41 % (Figure 3-1 a,b). For the electrode tape, the intersection method yielded 24 % porosity, with phase contents of 44 % NiO and 32 % BZCY-721, while the thresholding method indicated 32 % porosity, 44 % NiO, and 24 % BZCY-721. Because pores are the darkest color in the images and BZCY-721 appear lightest, the increase in porosity is not just a differentiation problem between BZCY and porosity but between all three phases. It was noted that the sample preparation process may have caused rounding of grain edges, which potentially affected results when using semi-automated grayscale thresholding methods. As a remedy, the cross-section preparation process was modified to a water-free method. These results underline the importance of comparing phase content and porosity quantifications only after checking the analysis method used to determine these numbers.

The initial process on its own experienced several issues. The first major issue was the electrolyte density, the second issue was the delamination of the electrolyte layer, the third problem was the shattering of the samples and the last issue was the excessive warpage. Several solutions addressing these issues have been partially presented in the chapters before, additional aspects will follow in the next sections.

With regards to scalability, the initial process used a comparatively inexpensive high refractory setter plate in combination with a single furnace run which reduced the energy consumption by omitting the separation of binder burnout and sintering steps. However, this omission led to the increased occupancy of the high-temperature furnace for an extended period of time for the low temperature heat-treatment. The number of samples per furnace run is limited by the overall amount of organic material burned out because of the lack of an exhaust system in these furnaces. Therefore, an increase in number of cells to be heat-treated will exaggerate the occupancy further.

7.2 Characterization of the Binder Burnout

7.2.1 Background and Motivation

To understand the transformation of the tape to a green body without organic components, it is important to take a step back and look at the components present in the tape before the binder burnout stage. In addition to the powder, the tapes contain solvent (MEK/Ethanol mixture), dispersant, plasticizers and binder. Methyl ethyl ketone and ethanol evaporate already in air at room temperature. Their boiling points are 80 °C and 78 °C respectively. [102,103] The burnout of pure PEG 400 was expected to start shortly below 400 °C and be completed by 450 °C. [104] The boiling point/burnout behavior of the dispersant (Nuosperse FX9086) and the type I plasticizer (3G8) were not provided by the manufacturer. The largest influence on the burnout of the organics inside the tape was expected to be the binder PVB. [63,66] However, temperature values reported in the literature typically pertain to the pure materials. Since the burnout and evaporation of substances are influenced by the additional components in the slurry, these values serve as approximations.

7.2.2 Experimental Set-Up

The burnout behavior was conducted through TG analysis. Heating and cooling were performed in Al_2O_3 crucibles at a rate of 5 K/min up to 1500 °C without any holding time. During the course of the work, many different tape compositions were tested. They are summarized in Table 7-1.

Table 7-1: Summary of tapes tested using TG analysis.

Purpose	Tested Tapes
Comparison of electrolyte and electrode tapes prepared following the initial slurry composition cast on KaroCast	22-ES-5 22-SS-5
Test of repeatability of the DTA-TG measurement	
Comparison of bilayer, electrolyte and electrode tapes prepared following the modified slurry preparation route cast on JuCast.	23-ES-17-SS-4 23-ES-17 23-SS-4
Comparison between the solvent-variation tapes	Tapes of Section 5.4
Comparison between the tapes of empirically-derived compositions	Tapes of Section 5.5

To analyze the microstructure of the green body after burnout, one cell (23-ES-17-SS-4) was heated as stated in the initial heat-treatment process up to 900 °C and then cooled down and a cross-section was prepared.

7.2.3 Results and Discussion

Figure 7-3 shows the results of the measurements for both types of tapes across two different temperature ranges. The observed differences are relatively minor. Mass loss below 200 °C (specifically at 166 °C, 99 %) is attributed primarily to residual solvent evaporation. [69] Comparing Figure 2-13 and Figure 7-4 reveals that the binder burnout for the three components of PVB + ZrO_2 shifts to lower temperatures. Three distinct steps in the PVB burnout process are clearly discernible for the electrolyte tape, whereas the burnout pattern of the electrode tape more closely follows that of pure PVB. The burnout of PEG-400 in the electrode tape appears

to occur below the burnout temperature of pure PEG-400, as no additional weight loss is observed beyond 400 °C. (Figure 7-3) In contrast, the electrolyte tape shows weight loss extending up to 800 °C.

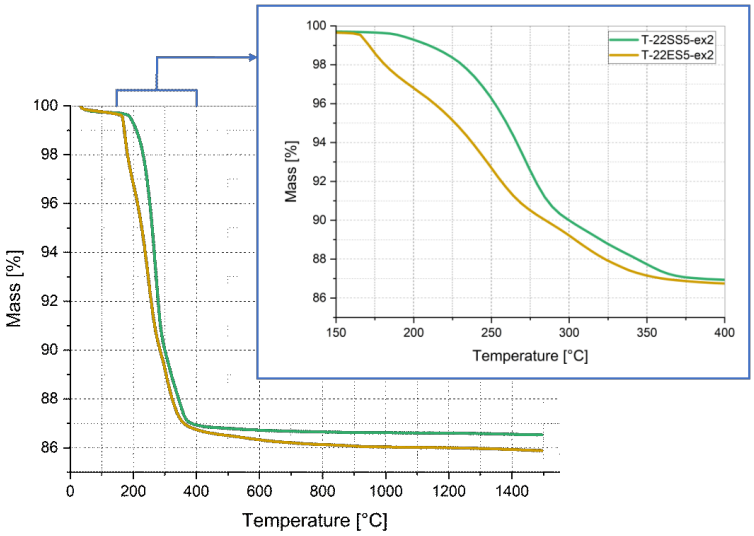

Figure 7-3: Comparison between the thermogravimetric measurements of the electrode tape vs. the electrolyte tape. left) Complete temperature range, right) reduced temperature range.

Both tapes underwent two measurements to assess repeatability (see Figure 7-4). Differences may stem from varying storage durations before measurement, as they are not assessed simultaneously. When discussing differences in binder burnout between electrode and electrolyte tapes, the accuracy of absolute values should be scrutinized. Variations within the same tape across different measurement runs can be comparable in magnitude to differences between tape types.

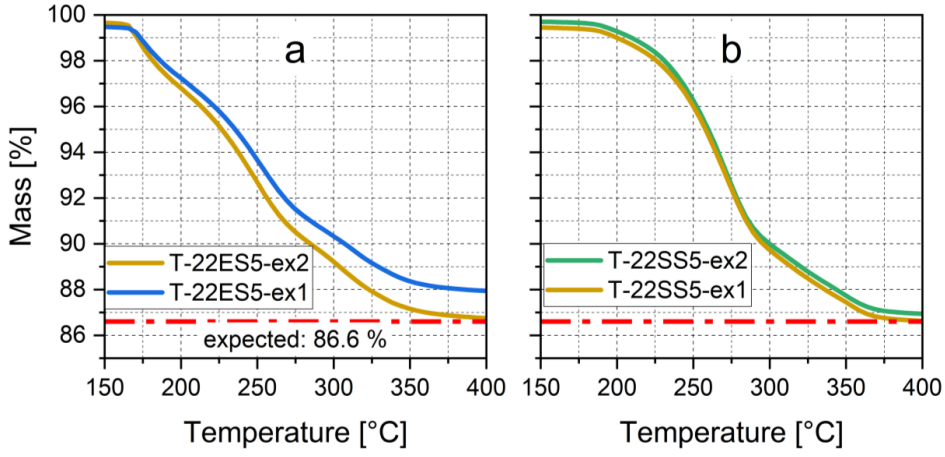

Figure 7-4: a) Thermogravimetric measurement of 22-ES-5-tape, both samples differ in mass loss, b) thermogravimetric measurement of 22-SS-5-tape, both measurements yield very similar results.

To further understand the binder burnout inside the electrolyte, the slurries from the investigation of slurries from minimal-composition and experimentally-derived composition where measured. The mass loss curves for these tapes give important insight into the different contributions of each component. Figure 7-5 compares the minimal-composition tapes; as expected, both ethanol-based slurries show the identical behavior. Also, the MEK/Ethanol based sample shows a similar curve. The absolute difference to the ethanol-based compositions stems from the added dispersant.

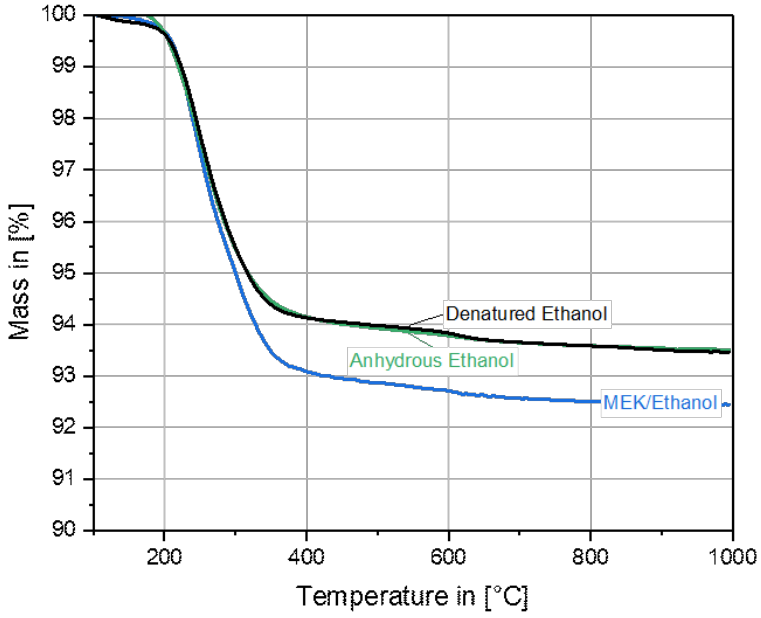

Figure 7-5: Mass loss over temperature for minimal-composition slurries; (note MEK/Ethanol mixture contained dispersant).

Figure 7-6 shows the result for the different empirically-derived compositions. It was observed that the mass loss curve differed notably from that of the initial tape. Notably, a kink just below 250 °C appeared in these measurements whereas the kink is absent in compositions lacking a plasticizer, indicating an interaction between the plasticizer and the powder components. For the reference composition as well as all the empirically-derived compositions, an increase in mass at 800 °C was observed. This increase was neither observed in the measurement of the minimal-composition slurries, nor in those measurements of the single layer tape presented in Figure 7-3. One possible explanation for this phenomenon could be that the added components (PEG 400, 3G8) interacted with the ceramic components and might have even changed the atmosphere which led to the take up of species from the furnace atmosphere which in turn increased the weight.

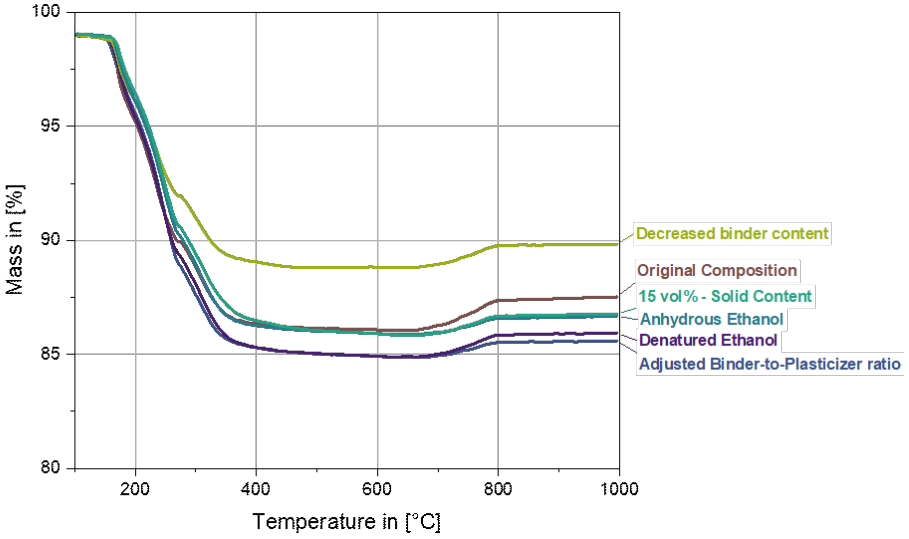

Figure 7-6: Mass loss over temperature for the empirically-derived-slurries, note the kink at 250 °C and the increase in weight at 800 °C.

7.2.4 Conclusion Burnout Characterization

The distinct decomposition behaviors of binders, plasticizers, and dispersants were influenced by their interaction with the ceramic powders. Electrolyte and electrode tapes exhibited unique burnout profiles, highlighting the importance of composition in determining thermal behavior. Mass gain observed in specific compositions at higher temperatures indicated interactions with atmospheric species, suggesting the need for atmospheric control during burnout. These findings underline the necessity of carefully tailored heating schedules to prevent defects such as trapped volatiles and ensure uniform organic removal. The adapted slurry composition did not appear to be changing the burnout behavior.

7.3 Sintering Challenges

Previous chapters have underscored that inadequate particle size and insufficient sintering aid content led to suboptimal densification in ceramic samples. To address this, efforts were made to reduce particle size and increase the sintering aid content to 0.5 wt.-% NiO. Despite these improvements, post-sintering analysis of bilayer assemblies—comprising a BZCY-721 electrolyte and a thicker BZCY-721 + 40 wt.-% NiO electrode layer—revealed persistent challenges in achieving satisfactory sintering results. While sufficient density remained the primary challenge in pellet preparation, half-cell sintering introduced additional complexities, particularly significant warpage and sample fracturing. The fundamental difference between pellets and half-cells lies in their structure: half-cells are multilayered, where the sintering behavior of one layer directly influences the other, often exacerbating shape deformation and fracture during processing.

The initial sintering procedure demonstrated that the majority of half-cell samples fractured or deformed significantly during sintering. These issues necessitated a more thorough investigation into the sintering process to understand and address the root causes. This chapter

approaches the problem in two distinct ways. First, it presents an in-depth characterization of the sintering behavior of tape cast single layers. While previous studies on BZCY sintering often rely on established bulk material behavior, this work highlights the importance of considering manufacturing influences such as microstructure variations, porosity gradients, and geometrical factors inherent to tape cast layers. By focusing on dilatometric measurements of single layers, this approach offers a more precise understanding of the material's sintering kinetics and shrinkage behavior.

The second section takes an empirical approach to address the practical challenges of warpage and sample fracturing. A systematic investigation was conducted to identify the key factors contributing to these defects and to develop optimized sintering setups that minimize warpage. These adjustments aimed to stabilize the multilayer assemblies during sintering, ensuring a degree of structural integrity that allows for accurate measurements and reliable cell production. Together, these two approaches provide both theoretical insights into sintering behavior and practical solutions for mitigating the challenges associated with half-cell sintering.

7.3.1 Warpage during Sintering

As discussed in the theoretical section, multilayer structures are inherently prone to warpage due to the differential shrinkage of the individual layers during sintering. This behavior arises from the distinct sintering kinetics and shrinkage rates of each layer. While both circular and rectangular samples exhibit warpage, the specific deformation patterns differ depending on the geometry of the sample.

For small-scale circular samples with diameters of approximately 20–25 mm, warpage typically manifests as a half-sphere- or U-shaped curvature. In these samples, the center remains relatively stable while the edges curve upwards, creating a concave structure. This behavior is largely due to the uniform distribution of stresses across the circular geometry, where the shrinkage mismatch between layers generates radial tension that results in an evenly curved surface. In contrast, rectangular samples tend to exhibit more pronounced warpage at the edges. Rather than forming a smooth bowl shape, the corners and edges of rectangular samples lift off more prominently, while the central region remains relatively flat. This edge-specific deformation occurs because the rectangular geometry does not allow for the same stress distribution as circular samples.

Figure 7-7 depicts a 5×5 cm^2 bilayer after sintering. Although this sample stayed in one piece without shattering, several typical defects can be seen. The figure includes defects which are directly caused by the sintering (warpage of edges) as well as such defects which stem from the tape casting process (trapped air bubbles). It also includes the typical cracking at the corners where the edge warpage exceeds the mechanical strength of the assembly.

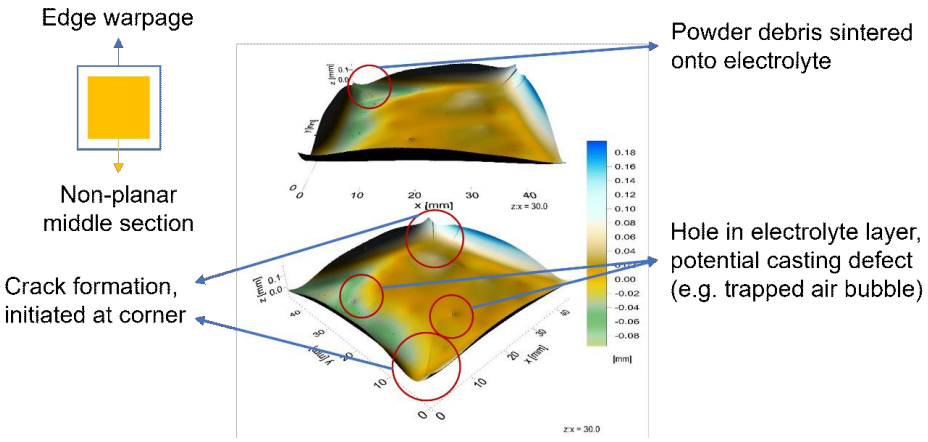

Figure 7-7: Bilayer 5 × 5 cm^2 sample sintered on BZCY/NiO powder bed with observed defects.

Figure 7-8 illustrates the warpage of a circular bilayer tape during sintering. For this, the sample underwent burn-out up to 900 °C and was subsequently sintered following the standard procedure using the TOMMI optical furnace. The bilayer was positioned on a ZrO_2 setter plate with the electrolyte facing upward. Warpage initiated around 1100 °C, as indicated by a slight lifting of the edges. This trend intensified up to 1400 °C, at which point the curvature increased more rapidly. At the maximum sintering temperature of 1550 °C, the warpage reached its peak and persisted during the holding period. The warpage remained unchanged after cooling, preventing the sample from returning to a flat state.

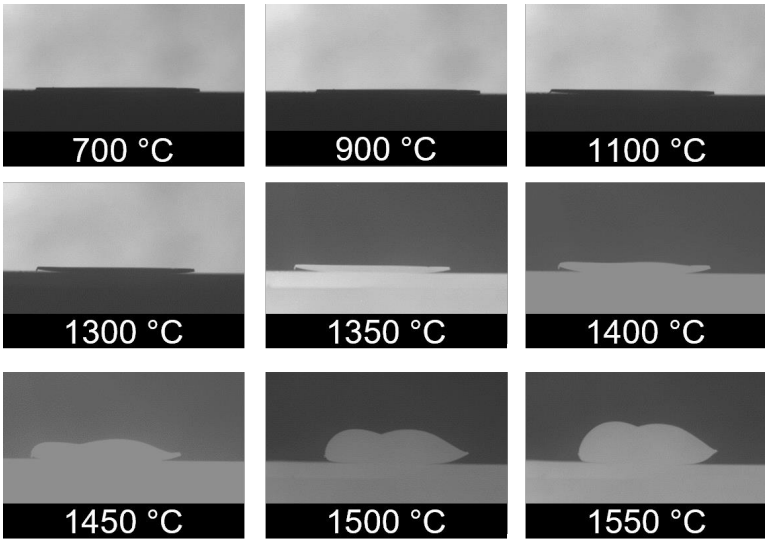

Figure 7-8: TOMMI optical dilatometer measurement of bilayer tape. Burnout of organic components before measurement. Identification of most critical phase between 1400 °C and 1500 °C.

7.4 Investigation of Sintering Behavior

7.4.1 Background and Motivation

Sintering shrinkage and shrinkage rate are critical parameters influencing the warpage of half-cells. These factors determine the dimensional stability of sintered components, particularly in multi-material laminates where differential shrinkage can cause significant deformation. The temperature corresponding to maximal shrinkage rate is especially crucial, as it marks a critical stage in the sintering process, where material diffusion processes are most active, enabling the transition to a fully densified microstructure. Achieving this is essential for ensuring optimal mechanical strength, proton conductivity, gas-tightness and overall functionality of the sintered half-cells.

Furthermore, monitoring changes in specimen dimensions during sintering provides insights into phase transformations. Certain phase changes can result in abrupt volume decreases, potentially inducing internal stresses or structural defects that compromise cell functionality. Understanding these transformations and their influence on shrinkage behavior is, therefore, vital for developing reliable sintering protocols ceramic specimens.

In the following chapter, two different types of dilatometer measurements will be introduced to investigate the sintering behavior of BZCY. The first part focuses on the material-specific behavior observed in pressed pellets made from ceramic base powders, providing insights into the fundamental shrinkage and densification characteristics of the material. The second section discusses measurements performed on single-layer samples, allowing for a more detailed analysis of the sintering behavior in isolation and serving as a reference for the bilayer results.

7.4.2 Sample Preparation and Measurement: Pellet Samples

Four different powders were compared to evaluate their sintering behavior. These include the purchased electrolyte powder 23K1 in its as-received state, the same electrolyte powder with an addition of 0.5 wt.-% NiO (Vogler), the initial sample based on in-house electrolyte powder with 0.25 wt.-% NiO, and the standard electrode powder containing 60 wt.-% NiO. The processing procedure for all powders followed the methodology described in the chapter on powder processing. The samples were pressed into 8 mm diameter pellets to ensure consistent geometry across all measurements. Dilatometry measurements were performed to track the dimensional changes of the samples from room temperature to 1600 °C at a controlled heating rate of 5 K/min in air.

7.4.3 Results and Discussion: Pellet Samples

The dilatometric curves are shown in Figure 7-9. A comparison of the sintering behavior reveals significant differences between the electrolyte pellets made from in-house BZCY powder and the commercially sourced BZCY-721. The sample exhibiting the highest total shrinkage (27 %) consisted of BZCY-721 with an added sintering additive of 0.5 wt.-% NiO. In comparison, the maximum shrinkage for the sample containing 60 wt.-% NiO was 23 %, while the sample without NiO shrank by 9 %, and the SSR-prepared sample demonstrated only 4 % shrinkage. This is on a stark contrast to the investigation by e.g., Chen et al. who documented much smaller shrinkages as seen in Figure 7-9 b). [92] Similarly low total shrinkage can be found in Liu et

al. [76] This highlights the limited comparability of shrinkage data available in the literature. Using overall shrinkage as a sole indicator of sinterability is often misleading. Only when supplemented with additional information, such as the initial and final densities, can overall shrinkage serve as a reliable basis for assessment. In the present case, however, such a comparison was only possible to a limited extent, since reliable final density values could not be determined for all samples. Severe crack formation after dilatometric measurement and interactions between the pellets and the dilatometer setup prevented recovery of intact specimens and thereby restricted the determination and interpretation of the final densities.

This sintering behavior was unexpected, as the pure electrolyte is generally considered very difficult to sinter according to the literature. It is commonly assumed that increasing the amount of NiO in the composition reduces the refractory nature of the electrolyte powder, thereby improving its sinterability. [105] However, as demonstrated above, this did not hold true for the powders investigated in this study. The order of sintering onset temperatures was as follows: the electrolyte made with purchased BZCY and 0.5 wt.-% NiO exhibited the earliest sintering onset, followed by BZCY + 60 wt.-% NiO, then the as-purchased BZCY powder, and finally, the in-house BZCY powder, which displayed the latest sintering onset. Interestingly, the substrate pellet (green curve) exhibited a maximum densification rate at a higher temperature compared to the electrolyte pellets. The electrolyte layer showed its maximal shrinkage rate around 1400 °C, while the substrate pellet peaked just below 1450 °C.

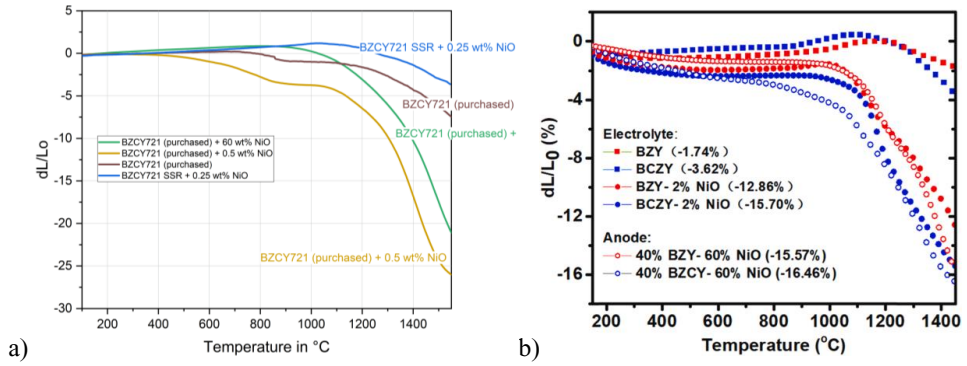

Figure 7-9: a) Dilatometry measurements of the different purchased powders and a comparison sample from earlier powder prepared by SSR, b) similar investigation by Chen et al. (BCZY: $BaZr_{0.1}Ce_{0.7}Y_{0.2}O_{3-\delta}$, BZY: $BaZr_{0.8}Y_{0.2}O_{3-\delta}$). [106]

These differences are noteworthy because the literature typically emphasizes the effects of varying NiO content on sintering shrinkage. However, these results indicate that the manufacturing route—which determines key powder properties such as particle size distribution, surface area, morphology, and green body density—may have a more significant impact on shrinkage behavior than the addition of NiO as a sintering additive alone. The switch to purchased powders significantly enhanced sinterability, as demonstrated by the improved half-cell microstructure described earlier in this chapter. This improvement can now be directly attributed to the enhanced shrinkage behavior of the electrolyte material.

The dilatometry samples were embedded and their microstructures were compared to a similarly sintered half-cell using the same materials to assess the applicability of the shrinkage

curves to the two-layer system. The results are summarized in Figure 7-10 for both the electrolyte and substrate samples.

As observed previously in electrolyte pellets, regions of higher density appear segregated from the surrounding matrix, which is evident in Figure 7-10 (top left). One explanation would be that the higher density of the agglomerates is the cause or the result of this detachment. Interestingly, this phenomenon was not observed in the electrolyte layer of the half-cell, possibly because the agglomerate size exceeds the thickness of the electrolyte layer. Another notable distinction is the markedly improved density of the half-cell electrolyte, which contains only isolated pores, in contrast to the pronounced porosity in the pellet sample. Several explanations could account for this difference. Firstly, the higher green density of the tape cast layer, resulting from the absence of pressing defects such as density gradients, may contribute to the improved sintering. Secondly, the presence of the substrate layer, with its high NiO content, could act as an additional source of sintering aid, potentially influencing the electrolyte layer. This sintering aid may also exert its effect through the gas phase. Lastly, the sintering setup itself may play a role. The half-cell was sintered on a ZrO_2 setter plate with an open top, whereas the pellet was constrained by the Al_2O_3 pushrod and plate in the dilatometric setup, possibly leading to NiO loss to the Al_2O_3 components and interfering with shrinkage behavior.

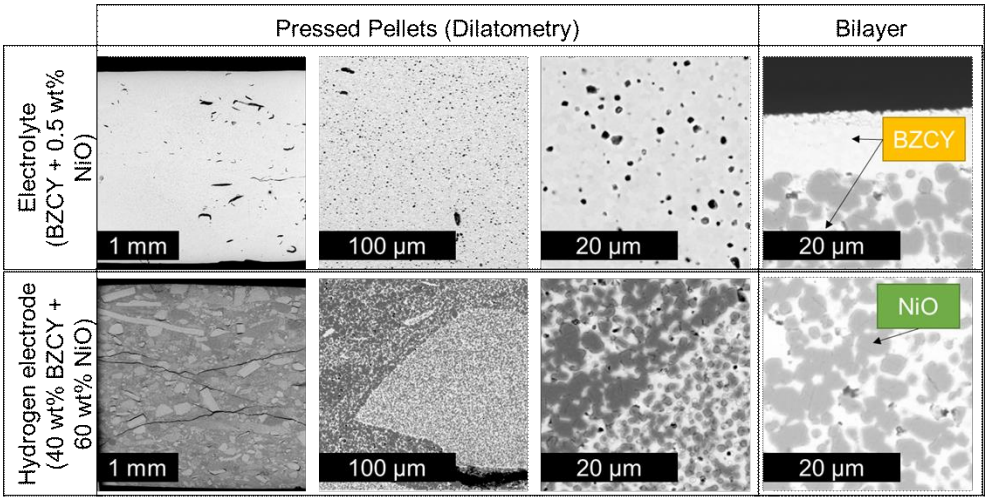

Figure 7-10: Side-by-side comparison at different magnifications between the substrate microstructure when processed as a pellet and when processed inside a bilayer assembly, black = porosity, grey = NiO, white = BZCY.

The microstructure of the substrate pellet used in the dilatometry measurements reveals notable heterogeneity, characterized by two distinct phases appearing as light and dark regions. These regions are not solely indicative of the presence or absence of NiO. Upon closer inspection, both phases are identified as dual-phase composites of BZCY and NiO, with varying ratios and particle sizes. This is in stark contrast to the microstructure of the half-cell substrate, where larger agglomerates of BZCY appear to be predominantly single-phase. Additionally, the NiO particles in the half-cell substrate are generally larger than those observed in the pellet. These differences highlight significant variations between the pellet and half-cell processing

conditions, raising concerns about the reliability of using dilatometry measurements from pellets to predict the shrinkage behavior of the substrate layer in a bilayer assembly.

7.4.4 Conclusion: Sintering of Pellet Samples

The dilatometry results revealed unexpected shrinkage behaviors in both the substrate powder pellets and the electrolyte pellet. Specifically, it was observed that the overall shrinkage of the electrolyte exceeded that of the substrate pellet. Moreover, the onset of shrinkage occurred at lower temperatures for the electrolyte, resulting in a mismatch between the shrinkage behaviors of the two layers within the temperature range of 1400 °C to 1500 °C. This mismatch has been correlated with bending of bilayers observed during TOMMIplus measurements. These findings suggest an opportunity for optimization in this temperature range, potentially by increasing the heating rate to bypass or mitigate the shrinkage mismatch.

The findings for the pellet sample offer valuable insights into the sintering dynamics of individual materials, highlighting the distinct thermal behavior of each. However, their direct applicability to the half-cell system is limited, as the interaction between layers introduces additional complexities. Furthermore, it was observed that the manufacturing route significantly influences the results, underscoring the preference for conducting measurements on tape cast samples rather than pellets to better represent the actual processing conditions.

7.4.5 Materials and Slurry Preparation: Kirigami samples

To test the single layers, special samples shapes were prepared, called Kirigami samples. (Kirigami is the Japanese art of paper cutting to form 3D structures without glue. [107]) The general set-up is pictured in Figure 7-11.

For the measurement of single layers, three different tapes were produced: one for each layer and one prepared without NiO addition to analyze the pure BZCY behavior. Three types of ceramic powders were used: BZCY (Marion Technologies, Batch 23K1), BZCY + 0.5 wt.-% NiO, and a mixture of 40 wt.-% BZCY and 60 wt.-% NiO (Vogler) as the standard electrode/substrate powder. Small quantities of slurry were prepared following the optimized procedure detailed in Chapter 5. The compositions and casting parameters are summarized in Table 7-2.

Table 7-2: Slurry and tape parameters for sintering behavior investigation.

	Pure BZCY	**BZCY-El**	**BZCY-NiO-Su**
Composition	BZCY (Batch 23K1)	BZCY (23K1) + 0.5 wt.-% NiO	40 wt.-% BZCY and 60 wt.-% NiO (Vogler)
Slurry Solvent	Denatured Ethanol		Denatured Ethanol + MEK
Blade Gap	800 µm		
Speed	2.5 mm/s		

7.4.6 Kirigami Sample Preparation

The geometry dimensions are adapted from Mücke, with a length of 13 mm and a width of 8 mm. [95] A connecting notch in the middle of each sample was adjusted to the tape's thickness to ensure maximum stability. The complex cutting process is detailed in Chapter 6. Due to the fragility of samples after burnout, cutting was performed on green-state samples to ensure defect-free results.

Two testing options were evaluated: the first involved assembling and directly measuring the samples using a dilatometer starting from their as-cast green state. The second option involved burning out the green samples before inserting them into the dilatometer as was done in the original procedure by Mücke. The samples following the second option, however, were too fragile after burn-out to handle and were therefore excluded from the analysis.

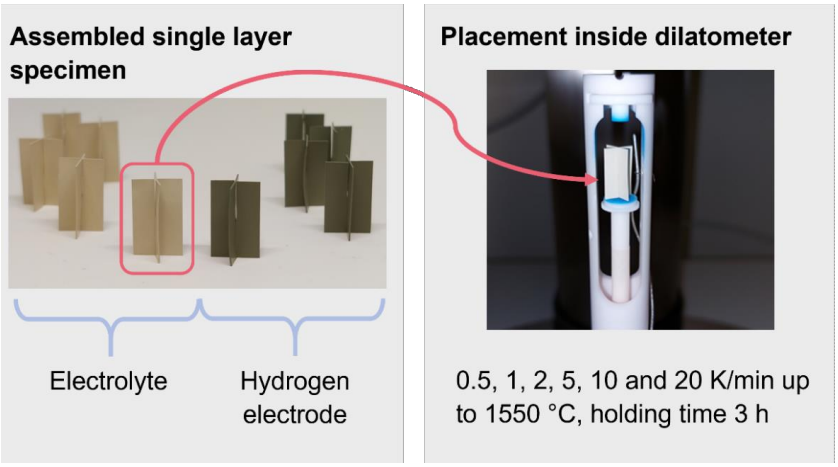

Figure 7-11: Sample configuration for vertical dilatometry, samples were cut in green state, Kirigami samples, after Mücke. [95]

7.4.7 Results and Discussion: Kirigami Samples

All Kirigami samples, starting from the green tape stage, remained intact during testing. To demonstrate the closer resemblance of the sample microstructure to that of bilayer half-cells, cross-sections of the samples were prepared and examined. An in-depth investigation was conducted for samples subjected to a heating rate of 5 K/min. Figure 7-12 presents micrographs of these sample cross-sections, highlighting that their microstructure closely mirrors that of the actual half-cell. However, the electrolyte layer in the single-layer samples exhibits a higher porosity compared to the bilayer assembly. This observation suggests that shrinkage within the electrolyte layer of the bilayer assembly might be even more pronounced than in the single-layer Kirigami samples, likely due to the constrained sintering environment and interactions with NiO inside the hydrogen electrode layer.

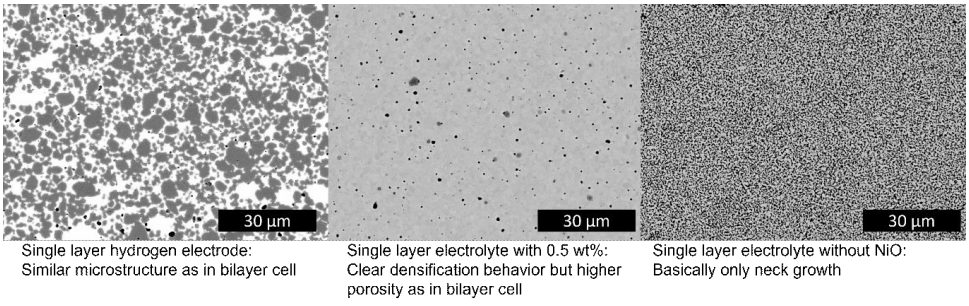

Figure 7-12: Micrographs of three Kirigami samples; hydrogen electrode, electrolyte with and without NiO addition; 5 K/min; 3 h 1550 °C; - 10 K/min.

Figure 7-13 illustrates the results for tapes containing nickel-free BZCY-721. The shrinkage does not display a clear trend with heating rate; however, plotting the sintering rate clarifies this relationship. Higher heating rates correspond to increased sintering rates, with all samples showing a similar onset of sintering just above 1100 °C.

The maximum shrinkage rate is not reached within the measured temperature range (up to 1550 °C), which aligns with literature findings for BZCY without added NiO. [78] Most heating rates result in comparable shrinkage, except for the 0.5 K/min heating rate sample. One possible explanation is that measurements of NiO-containing samples were conducted prior to this experiment, potentially contaminating the furnace. Since NiO is active as a sintering additive through the gas phase, prolonged exposure to this environment may have influenced the observed behavior.

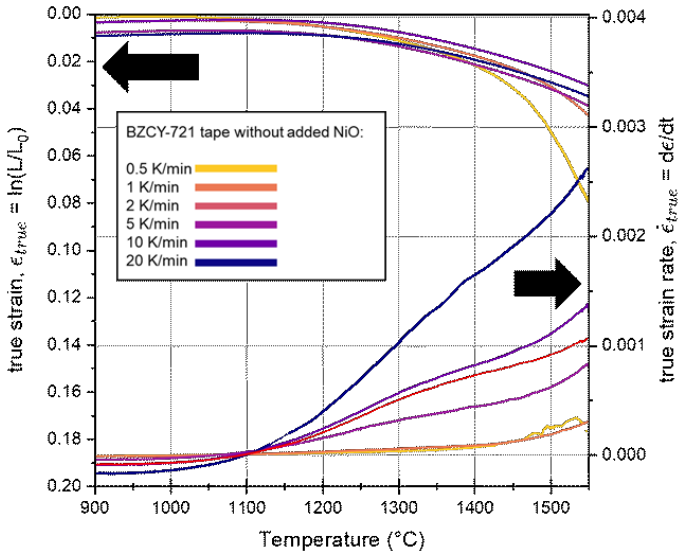

Figure 7-13: Relative shrinkage and sintering rates of Nickel-free BZCY-721 tape (note different scale then diagrams for electrolyte single layer and substrate single layer).

Figure 7-14 and Figure 7-15 show the shrinkage behaviors of the electrolyte and electrode single-layers respectively. Comparing their relative shrinkage dependency on the heating rate reveals that the electrode's overall shrinkage remains unaffected by increased heating rates, whereas the electrolyte's curve shifts to higher temperatures, indicating a kinetic influence on its sintering mechanism. A minimal shift of peak sintering rate temperature < Δ100 °C is not unusual. Mücke found similar results in the original study on YSZ and Ni/YSZ. [95] The more complex behavior observed in the electrolyte curve can be partially attributed to the known occurrence of a transient liquid phase. The formation rate of a secondary phase can only be accelerated to a certain extent, making it significantly influenced by increases in the heating rate.

Most literature on fundamental solid state sintering concepts focuses on single phase material systems such as Al_2O_3 and ZrO_2. [55,84] These systems, in their pure forms, do not undergo liquid-phase sintering. The standard sintering mechanisms of solid-state sintering are only slightly influenced by changes in the heating rate. Generally, the shrinkage rate correlates

linearly with heating rates. Changes in heating rate typically do not—or only to a limited extent—shift the temperature of the maximum shrinkage rate to higher values.

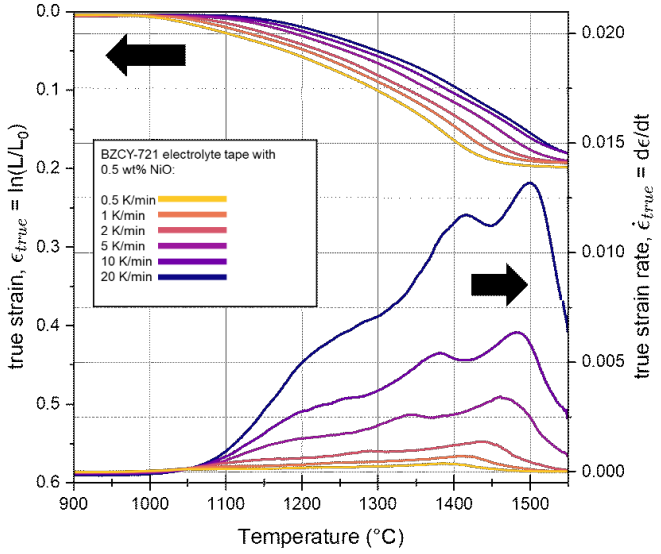

Figure 7-14: Relative shrinkage and sintering rates of the electrolyte single layer depending on heating rate.

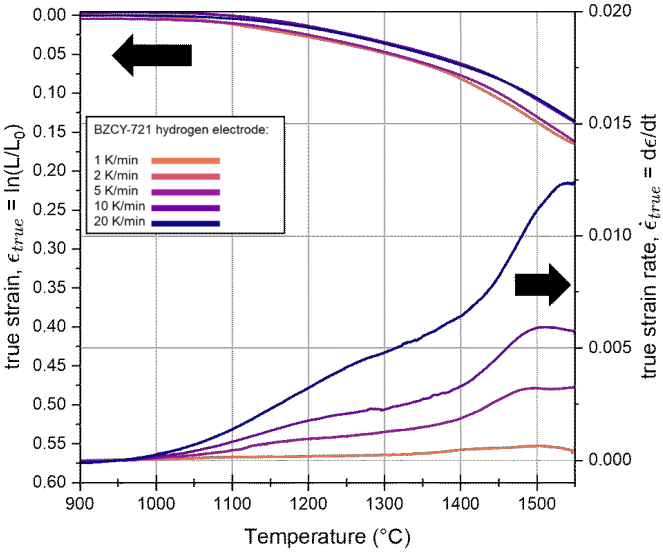

Figure 7-15: Relative shrinkage and sintering rates of the hydrogen electrode single layer depending on heating rate.

However, other mechanisms, such as the formation of secondary phases, particularly transient liquid phases, are known to be kinetically dependent. [108] In the BZCY system, where the formation of a transient liquid phase is a known phenomenon, such a shift is therefore expected. Surprisingly, despite the substantial amount of NiO in the electrode composition, this dependency is not observed in the electrode sample.

Table 7-3: Shrinkage characteristics of electrolyte layer peak, (OriginPro 2024, “Minitool”, manual range selection, local maximum in range of 10 data points).

Heating rate		**20**	**10**	**5**	**2**	**1**	**0.5**	**Range**
		[K/min]						ΔK
Onset	[°C]	1062	1067	1055	1019	982	942	119
1st turning point	[°C]	1209	1195	1178	1133	1097	1051	158
2nd turning point	[°C]	1317	1293	1278	1220	1182	-	>135
2nd highest peak	[°C]	1423	1383	1349	1291	1241	1210	213
Sintering rate	[1/min]	0.0147	0.0066	0.0032	0.0011	-	-	-
Highest peak	[°C]	1502	1487	1462	1442	1410	1386	116
Sintering rate	[1/min]	0.019	0.0088	0.0048	0.0019	0.0010	0.0005	-
Range	**ΔK**	**441**	**420**	**406**	**423**	**428**	**444**	**560**

Comparing the sintering rates of the electrolyte single layer with those of the nickel-free tape shows a slight shift in the onset of sintering to 1050 °C. This shift is attributed to the addition of nickel oxide, which primarily impacts the system by introducing new sintering mechanisms through liquid-phase sintering. The supplementary information includes a TEM micrograph of a pellet sample which exhibits larger Y and Ni segregation at the grain boundaries. This is possibly a sign of the transient liquid phase in the system.

In the sintering results of the electrolyte Kirigami samples as pictured in Figure 7-14, three distinct regions can be identified for the electrolyte layer, each associated with characteristic sintering behaviors. The first region is marked by the sintering onset and a slight decrease in the sintering rate slope, followed by a local maximum that is visible in the 0.5 K/min curve but not distinctly apparent in higher heating rates. By tracking the position of these local maxima (temperature and sintering rate) as well as the turning points within the first region (Inlay Figure 7-16) for each heating rate, trends can be identified. Table 7-3 summarizes the positions of these points across heating rates.

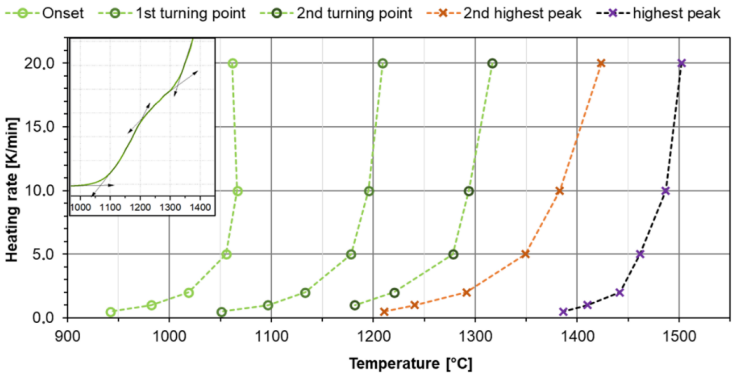

Figure 7-16: Characteristic points and their heating rate dependency. Inlay: schematic for the determination of Onset, 1st and 2nd turning point.

Examining the trend (Figure 7-16) from 0.5 K/min to 20 K/min reveals that the position of the maximum sintering rate of the highest peak shifts from 1386 °C to 1502 °C, corresponding to an increase of approximately 116 K, which is comparable to the shift of the sintering onset temperature by 119 K. In contrast, the second peak exhibits a much larger shift in position by 213 K, moving from 1210 °C to 1423 °C. This significant shift suggests that the sintering mechanism associated with the second peak is highly dependent on the heating rate. The transient liquid phase, believed to form and melt around 1400 °C, might be responsible for the second peak even before its melting.

7.4.8 Consequences for Bilayer Warpage

The shift of maximum sintering rate peaks observed for the electrolyte samples, which remains absent in the hydrogen electrode samples, underscores the pronounced dependence of the strain rate difference on the heating rate. This relationship is depicted in Figure 7-17, where three distinct zones are identified, each corresponding to a layer dominating the warpage behavior. Positive strain rate differences indicate warpage towards the electrolyte side, while negative values signify warpage towards the electrode side.

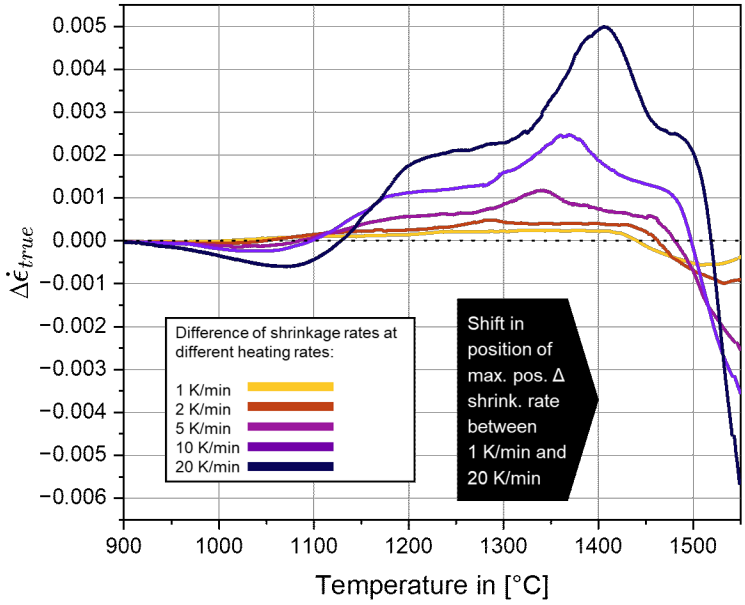

Figure 7-17: Difference between shrinkage rate of the electrolyte layer and the electrode layers for different heating rates.

The first observation from these results suggests that warpage towards the electrode side should occur initially. However, this behavior was not observed in the TOMMIplus images, possibly because the magnitude of this initial warpage was too small to overcome the combined weight of the cell and the friction with the setter plate. This insight offers also a mitigation strategy: by sintering the side prone to greater warpage in direct contact with the setter plate, gravitational forces could counteract the deformation, reducing the impact of the mismatch.

Higher heating rates not only amplify the strain rate differences but also shift the temperature of the largest electrolyte-dominated delta by approximately 150 K, moving from 1 K/min to 20 K/min. This temperature, representing the most critical range for warpage, demands careful consideration in multilayer sintering schedules. The pronounced heating rate dependence of the electrolyte layer compared to the more stable hydrogen electrode layer introduces significant thermal mismatch challenges, as the strain rate mismatch intensifies at higher heating rates.

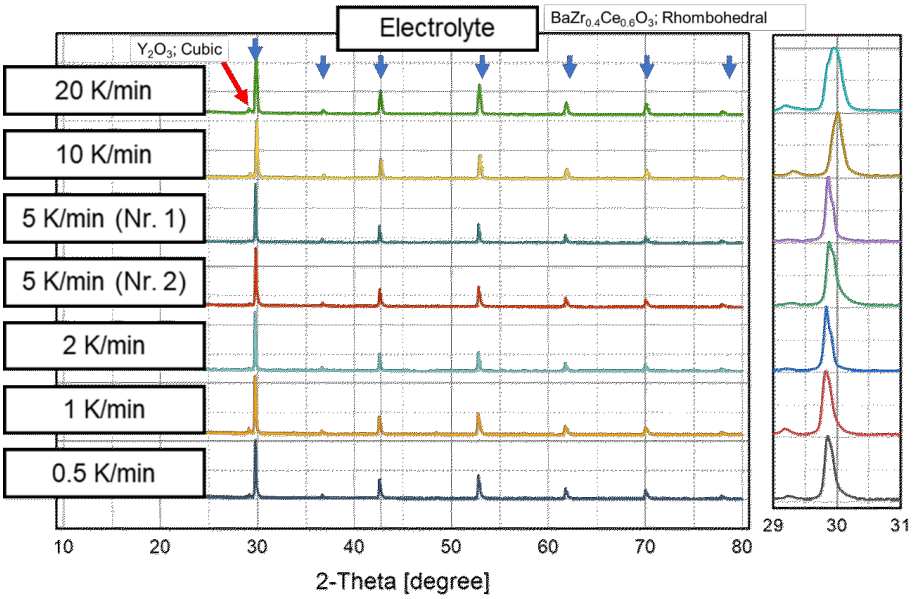

Figure 7-18: XRD results of electrolyte Kirigami samples heated with different rates. Shift in peak position depending on heating rate.

Figure 7-18 illustrates the variation in phase structure of the electrolyte as a function of heating rate. While the overall phase composition remains largely consistent, notable differences are observed in the symmetry, width, and position of the reflections. These variations highlight the sensitivity of the material's crystalline structure to the heating rate during sintering. Such changes can significantly influence the microstructural properties, potentially altering key factors like grain boundary characteristics, defect density, and lattice strain. Although not investigating the impact of the heating rate, Wang et al. also found a wide variability of the precise phase composition depending on sintering conditions. [39] Different mechanisms are introduced as possible explanations, such as thermal reduction of Ce^{4+} to Ce^{3+} might promote the displacement of Ce to the Ba-site which also might support the formation of CeO_2 secondary phases. Consequently, the heating rate not only affects the phase structure but also likely impacts the electrochemical properties, as these are closely tied to the structural integrity and phase distribution of the material.

Figure 7-19 presents the results for the hydrogen electrode Kirigami samples. The phase structure closely resembles that of the electrolyte samples, with the addition of the NiO phase characteristic of the hydrogen electrode. However, unlike the electrolyte layer, the peaks for the hydrogen electrode samples do not exhibit a similar shift in position with varying heating rates. This suggests that the phase structure of the hydrogen electrode is less sensitive to changes in

heating rate, potentially due to the stabilizing influence of the NiO phase. This relative stability in phase structure may contribute to the consistent sintering behavior observed for the hydrogen electrode across different heating rates.

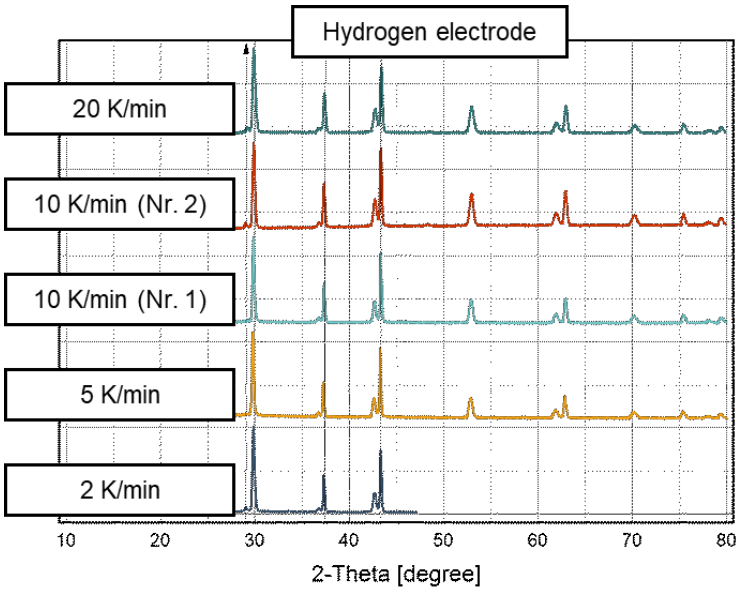

Figure 7-19: XRD results of hydrogen electrode Kirigami samples heated with different rates.

For further analysis, samples were sintered with a heating rate of 5 K/min, and holding experiments were conducted to examine the phase evolution during sintering. Figure 7-20 shows the results of these experiments, in which the sintering process was stopped approximately 50 K above each peak observed at the 5 K/min sintering rate.

The phase composition of the electrolyte at various sintering temperatures reveals a sequence of dynamic phase transitions throughout the process. At 900 °C, corresponding to the end of the burn-out stage, the identified phases were orthorhombic $BaZr_{0.2}Ce_{0.8}O_{3-\delta}$ and cubic $BaZr_{0.9}Y_{0.1}O_{3-\delta}$. At 1210 °C, the composition shifted to cubic $BaZr_{0.9}Ce_{0.1}O_{3-\delta}$ and cubic Y_2O_3. At 1390 °C, rhombohedral $BaZr_{0.6}Ce_{0.4}O_{3-\delta}$ and cubic $BaZrO_3$ emerged. By 1500 °C, cubic $BaZr_{0.9}Ce_{0.1}O_{3-\delta}$ dominated the phase composition. These transitions highlight the temperature-dependent stability of various phases and underline the complex interplay between temperature and material structure.

The electrode phase composition largely mirrored that of the electrolyte, with the addition of cubic NiO as a consistent component. At 900 °C, the phases included cubic NiO, cubic $BaZr_{0.2}Ce_{0.8}O_{3-\delta}$, and cubic $BaZr_{0.9}Y_{0.1}O_{3-\delta}$. At 1210 °C, cubic $BaZrO_3$, rhombohedral $BaZr_{0.6}Ce_{0.4}O_{3-\delta}$, and cubic NiO were identified. At 1390 °C, cubic $Ba_{0.97}Zr_{0.92}Ce_{0.1}O_{3-\delta}$ and rhombohedral $BaZr_{0.6}Ce_{0.4}O_{3-\delta}$ were present alongside cubic NiO. Finally, at 1500 °C, cubic $BaZr_{0.9}Ce_{0.1}O_{3-\delta}$ and cubic NiO dominated the structure.

Surprisingly, despite the high concentration of NiO in the electrode, its influence on the phase development of the BZCY system appears to be limited. This observation challenges the expectation that NiO would significantly alter the phase transitions and suggests that the

interaction between NiO and the BZCY system during sintering is less pronounced than anticipated. Further investigation is warranted to understand the mechanisms governing these interactions and their impact on the final microstructure.

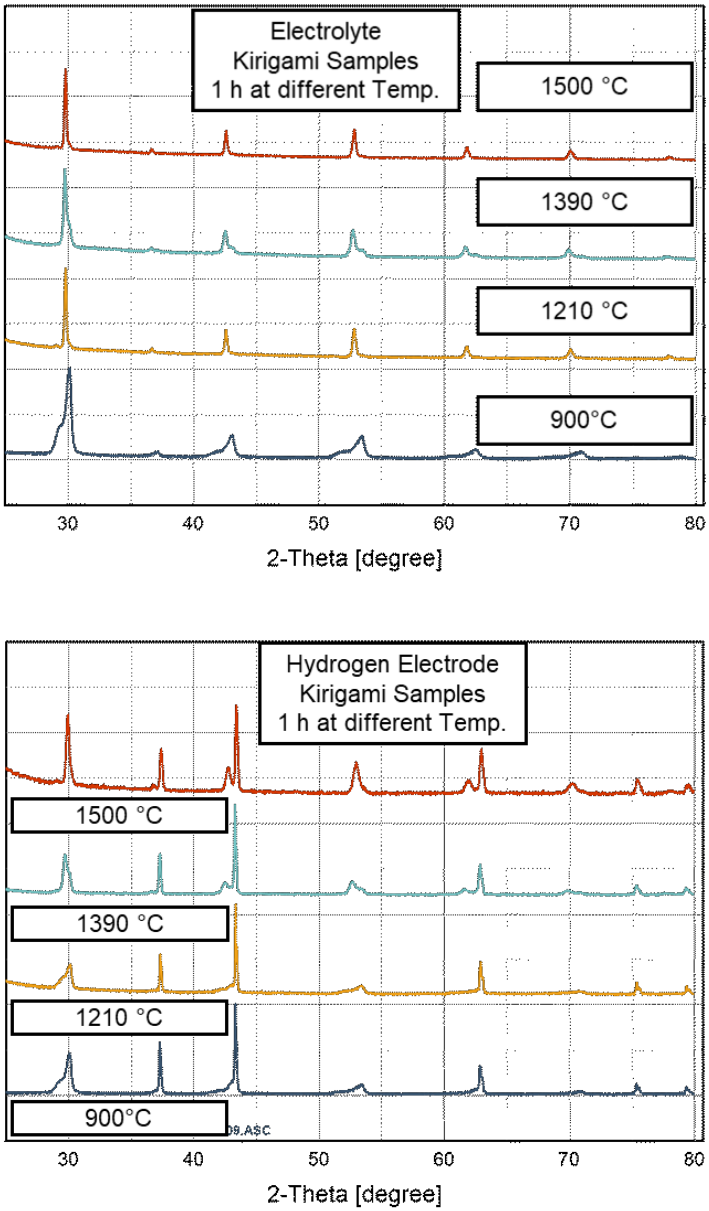

Figure 7-20: XRD spectra for the Kirigami samples held for 1 h at different max. temperatures: top) electrolyte, bottom) hydrogen electrode.

7.4.9 Calculation of Activation Energies

The initial objective of the sintering shrinkage investigation was to identify differences in shrinkage rates and develop an optimized heating schedule. However, it became evident that the shrinkage behavior of both layers is more complex than initially anticipated. Applying standard models to the sintering curves proved ineffective, as many models require a more detailed understanding of the material's internal processes. Given the limited data available for BZCY materials, only general observations could be made.

One approach to determine the activation energy involves deriving master sintering curves from density measurements over the heat-treatment (assuming one dominant mechanism within the observed temperature range). [109] The master sintering curve approach would require tracking changes in sample density throughout sintering. The Kirigami samples provide data only about in-plane shrinkage; to obtain the missing information on tape thickness shrinkage, thin samples were cut and measured in the z-direction. These results, presented in the supplementary section, were ultimately deemed unreliable due to the sensitivity of dilatometry measurements to sample height, which significantly affected data quality. Therefore, the path through the density correlations using the master sintering curve was not chosen. Instead, an isoconversional method was chosen.

The mathematical method of Ozawa-Flynn-Wall assumes a "reaction" which has reached its equilibrium at the end of the heating interval. However, for both BZCY without a sintering aid and the fuel electrode material, the sintering curves indicate that the process has not yet reached full densification by the time the isothermal dwell period begins (see Figure 7-14 and Figure 7-15). This incomplete progression through the sintering stage means that the necessary end-state conditions for calculating activation energy and constructing a reliable model are not met. Consequently, this approach cannot be accurately applied to these materials, as the method's assumptions break down when sintering is ongoing beyond the expected temperature range. Only the shrinkage curves for the heating rates of 0.5, 1 and 2 K/min of the electrolyte samples fulfill this requirement. Therefore, the following calculation of the activation energy is limited to those measurements.

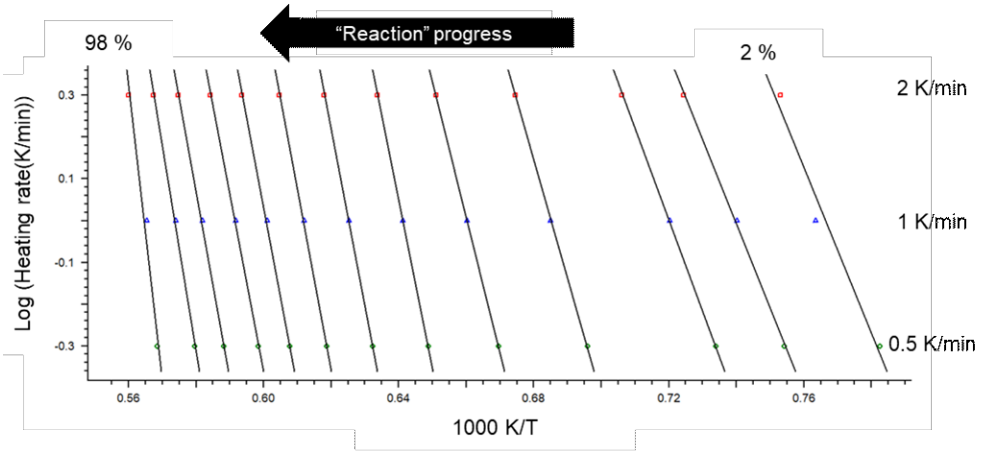

Figure 7-21: Ozawa-Flynn-Wall isoconversional analysis to determine the activation energy for each point in the progress of the sintering process (Software: NETZSCH Thermokinetics).

In Figure 7-21, the outcome of this mathematical treatment is displayed, with distinct shifts in slope readily observable. When the two characteristic aspects of each slope are isolated and plotted in a separate graph, Figure 7-22 is obtained.

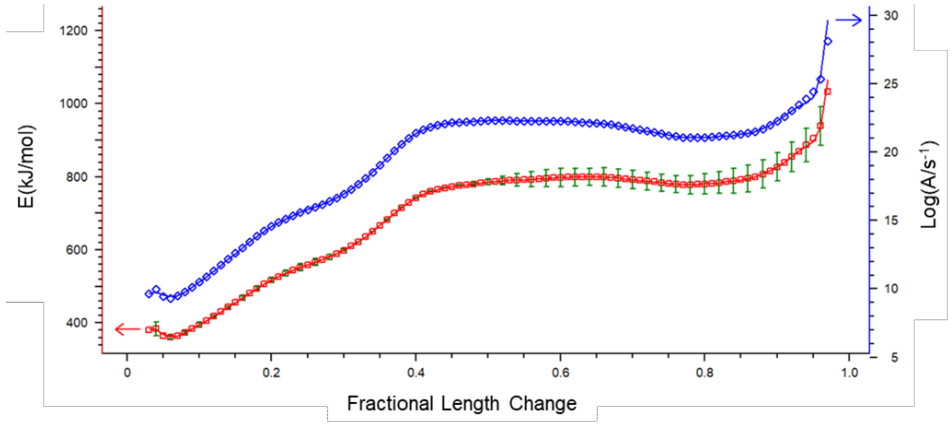

Figure 7-22: Activation energies as calculated based on the Ozawa-Flynn-Wall isoconversional analysis (Software: NETZSCH Thermokinetics).

If the three sections identified visually in the sintering rate diagrams indeed represent distinct, sequential reactions, we would expect to observe three discrete levels in the activation energy plot. A key insight from the OFW analysis is that at least two processes with differing activation energies are present between 40 to 50 % shrinkage, which corresponds to a temperature range of approximately 1350 to 1500 °C, depending on the heating rate. This observation reveals that the activation energy during this stage is notably higher than at the onset of sintering. This finding aligns with the visual analysis, where a shift in the sintering rate peak with varying heating rates was observed.

7.4.10 Conclusion

The study of sintering behavior revealed several critical insights into the shrinkage behavior of the materials used. Initial dilatometry tests on pellets challenged the assumption that increased NiO content always improves sinterability, particularly in the case of hydrogen electrodes. However, it was found that pellet samples do not accurately represent the actual microstructure of bilayer assemblies, necessitating the use of dilatometry tests on single-layer tape-cast samples. Microstructural analysis confirmed that the single-layer test samples closely resemble bilayers, supporting the reliability of single-layer measurements for understanding bilayer behavior.

Three distinct stages of sintering were identified, each characterized by kinetically inhibited mechanisms that shift to higher temperatures with increasing heating rates. The shrinkage behavior of electrode and electrolyte layers exhibited significant differences. While electrode shrinkage showed minimal sensitivity to heating rates, electrolyte shrinkage strongly depended on the heating rate, with the characteristic temperatures of sintering stages shifting to higher values as heating rates increased. These differences are critical for understanding and controlling warpage in multilayer assemblies, as heating rate adjustments can significantly influence shrinkage mismatches.

If one considers any heating rate between 0. 5 K/min and 20 K/min as feasible for a sintering schedule, the entire range from the onset of electrolyte sintering to the maximum shrinkage point offers a window of 560 K. This range allows careful adaptation of the sintering schedule to precisely control sintering mechanisms and effectively mitigate warpage.

Activation energies calculated based on 0.5, 1, and 2 K/min heating rates revealed no clear steps, suggesting significant overlap in the temperature ranges of the underlying mechanisms. This complexity posed challenges for fully identifying the sintering mechanisms, with the mathematical techniques employed reaching their limitations.

Despite these challenges, the findings highlight opportunities for optimization. The pronounced heating rate dependence of the electrolyte layer provides a basis for tailoring sintering schedules, with adjusted heating rates and dwell times offering potential for mitigating warpage and improving structural integrity. These insights lay the groundwork for future research to further refine sintering strategies, enhancing the quality and reliability of multilayer assemblies.

7.5 Investigation of Different Sintering Set-Ups

7.5.1 Background and Motivation

Achieving flat and intact cells during sintering was a persistent challenge throughout this thesis. While the sintering shrinkage experiments provided valuable insights into the behavior of single-layer tapes, they did not offer an easy solution to solve the warpage challenge. Therefore, alternative approaches were explored to mitigate warpage and prevent cell shattering during sintering.

Early on, numerous sintering setups were empirically tested, each aiming to address issues such as warping, cracking, and structural inconsistencies. However, the complexity of the ceramic production process, spanning from raw powder characteristics to post-sintering treatments, introduced a wide range of variables. This variability made it difficult to systematically investigate and optimize the sintering process, as changes in one step of the production chain often influenced the outcomes of others.

Moreover, while some sintering setups yielded promising results for specific cell types, their success could not be reliably reproduced across different cell designs. This lack of uniformity highlighted the need for a standardized cell production process as a foundation for systematic sintering studies. The turning point came with the successful casting of JuCast bilayers, which offered a consistent and scalable base structure. With this development, it became possible to investigate sintering setups systematically, as the cells now shared comparable dimensions and properties.

This following section consolidates the findings from earlier trials and introduces the optimized sintering procedure developed during this thesis. It begins by summarizing key insights from pre-JuCast bilayer experiments, emphasizing how these enabled the identification of critical parameters. The culmination of these efforts is the presentation of a comprehensive sintering setup that integrates the lessons learned into a robust process, capable of reliably producing flat and intact cells. This procedure represents the synthesis of the work conducted and serves as a foundation for future developments in this field.

Table 7-4: List of commodities used in sintering set-up.

	Supplier	Material Specifics	Usage
Setter plates and crucibles			
MgO	Unknown	Unknown	Setter plate and weight
Al_2O_3 crucibles	GTS Keramik	99,7 % purity, dense	Calcination, Sintering of samples in powder beds
ZrO_2 crucibles		8-YSZ	
Y-ZrO_2 setter plate (smooth)	Nikatto	Unknown	Setter plate
Y-ZrO_2 setter plate (rough)	Unknown	Unknown	
Y-ZrO_2 tape	Tape cast in-house	8-YSZ	
ZrO_2 coated Al_2O_3	Kerafol, Keramische Folien GmbH & Co. KG	Unknown	Setter plate and weight
Y_2O_3 coated ZrO_2			
Milling Balls			
d = 1 mm	SiLiBeads, Sigmund Lindner GmbH	YSZ	Milling of powder experiments
d = 3 mm			Standard for milling of powder and homogenization of slurries
d = 10 mm			Needed for large-scale slurry homogenization

7.5.2 Experimental Set-Up

Table 7-4 introduces the commodities used to variate the sintering set-ups. Table 7-5 presents the different sintering strategies.

Table 7-5: Sintering improvement strategies, materials and their corresponding purpose of intervention.

	Material	Purpose of intervention
Material underneath the specimen		
Variation of setter plate material	MgO, Al_2O_3, ZrO_2 (different suppliers), Y_2O_3 coated ZrO_2 plates, ZrO_2 coated Al_2O_3.	Limitation of chemical interaction and change of friction through different roughness
Milling balls as setter material	ZrO_2-milling balls, BZCY/NiO saturated milling balls	Limitation of chemical interaction and change of friction, improved air circulation for binder burnout
Variation of powder bed	BZCY powder, 40 wt.-% BZCY + 60 wt.-% NiO (different coarseness)	Limitation of chemical interaction, change of friction, change of atmosphere (NiO, Ba-Y-NiO, BaO)
Samples as setter plates	Sintered half-cells as setter plates	Limitation of chemical interaction

Material above the specimen		
Setter plates as weights, different weights	MgO, Al_2O_3, ZrO_2 (different suppliers), specialized Al_2O_3 coated ZrO_2 plates, ZrO_2 coated Al_2O_3.	Limit loss of species to the furnace atmosphere, mechanical limit of warpage
Embedding in powder bed	BZCY powder, BZCY + NiO	Limit loss of species to the furnace atmosphere, mechanical limit of warpage,
Increase of sintering temperature		
Increase of max sintering temperature	1500 °C => 1550 °C	Promote densification
Changes to binder burnout procedure		
Separation of Binder burnout and sintering	0.5 K/min to 900 °C then – 2 K/min room temperature, followed by regular sintering run.	Limitation of binder burnout products in the sintering atmosphere
Weighted binder burnout	As above with the addition of a setter plate which was lifted before the second run	Limitation of warpage due to different binder burnout shrinkage.

7.5.3 Results and Discussion of Pre-Tests

Pre-tests on samples of BZCY-622 composition: Due to challenges encountered during tape casting, which hindered the production of cells for testing the sintering setup, cells composed of BZCY-622 were fabricated to evaluate various sintering conditions. Figure 7-23 shows the results for samples sintered on ZrO_2 plates. The excessive warpage and surface defects observed highlight the limitations of this approach. Overall shrinkage was determined as ~ 28 %.

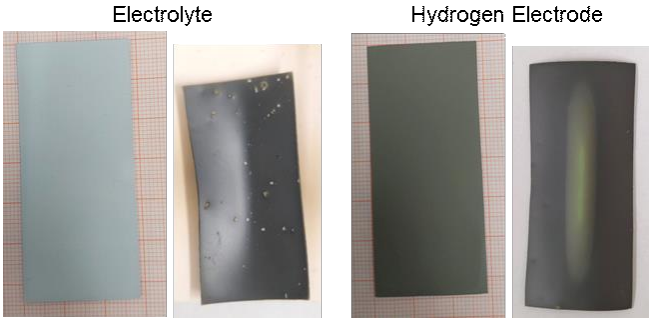

Figure 7-23: BZCY-622 bilayer sintered on YSZ at 1500 °C, before and after sintering. Image sizes of the sintered samples were adjusted to match the scale in the image of the green samples.

The following strategies were tested:

- **Enclosed crucible sintering**: Samples were placed inside an enclosed crucible to prevent debris from the furnace from settling on the surfaces. To enhance binder burnout without restricting gas circulation, samples were supported by ZrO_2 milling balls, with additional milling balls placed on top as weights. However, this setup led to distinct spots of localized interdiffusion where the samples were in contact with the milling balls.

- **Sintering inside and on top of powder beds**: Samples sintered within or directly atop BZCY powder beds continued to exhibit significant warpage. Furthermore, those in direct contact with the BZCY powder lost considerable amounts of NiO, likely due to interdiffusion and reaction at the interface.
- **Modified crucible setup with saturated milling balls**: An alternative arrangement involved placing the samples inside a crucible partially filled with BZCY powder. Above this layer, ZrO_2 milling balls pre-saturated with BZCY/NiO during a prior heat-treatment were added to minimize interdiffusion between the balls and the hydrogen electrode. This setup proved highly promising for the BZCY-622 composition, showing reduced warpage and minimized NiO loss compared to previous configurations.

Set-up transfer to bilayers of BZCY-721: This modified setup was applied to bilayers produced using the improved tape casting compositions from both the JuCast and KaroCast systems. As shown in Figure 7-24, the setup optimized for bilayers of the BZCY-622 composition was not transferable to the BZCY-721 composition with the improved electrolyte slurry. Interestingly, the electrolyte layer of the JuCast half-cells completely delaminated from the hydrogen electrode, whereas samples cut from KaroCast tape exhibited less delamination but showed increased warpage. This warpage was caused by the prolonged influence of the shrinking electrolyte on the multilayer assembly. The resulting warpage stresses in the KaroCast cells led to crack formation perpendicular to the warpage direction. Another approach was explored: using a BZCY/NiO powder bed instead of the saturated milling balls and sintering to 1550 °C. In this setup, the resulting cells still experienced warpage, but the color change to a dark black suggested promising densification.

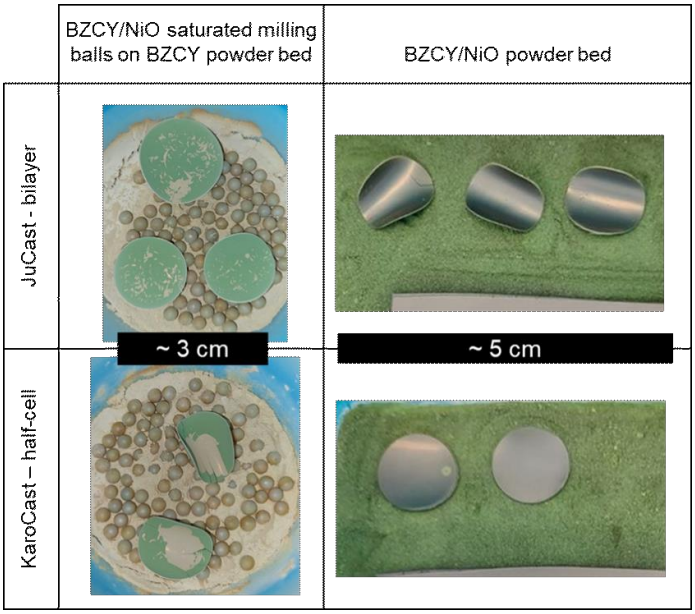

Figure 7-24: left) Transfer of initially optimized sintering set-up for BZCY-622 to BZCY-721 with improved electrolyte slurry (1500 °C), right) sintered on BZCY/NiO powder bed at 1550 °C.

MgO vs. ZrO_2: MgO plates were initially chosen for sintering due to their high-temperature stability, cost efficiency and their usage in literature for sintering BZCY specimens containing low amounts of NiO. [77] Half-cells sintered on MgO generally remained crack-free with minor warpage, yet failed to achieve the targeted electrolyte density. One common observation was difference in discoloration between the color of the sample which was in direct contact with the MgO and the part of the sample which was not due to the lift off. Figure 7-25 shows the comparison between two half-cells when sintered on two types of setter plates: ZrO_2 and MgO. Electrodes in contact with MgO showed less pronounced NiO reflections in XRD spectra compared to those in contact with ZrO_2. Furthermore, the choice of setter plate also influenced the non-contacting electrolyte side. Samples sintered on MgO exhibited a cubic structure of $BaZrO_3$, whereas those on ZrO_2 showed a greater tendency toward the rhombohedral structure of $BaCe_{0.4}Zr_{0.6}O_{3-\delta}$.

Significant nickel loss occurred due to solid solution formation between MgO and NiO, resulting in a depleted nickel area along the electrode/setter plate contact surface. A common method for limiting this loss is the saturation of the setter plate with the NiO. This was not successful, because the setter plate broke during the saturation process before the necessary level of saturation was accomplished. Referring to the phase diagram of MgO and NiO, it becomes evident that MgO and NiO form a solid solution throughout their entire compositional range. [110,111] Consequently, MgO was excluded from large-scale sintering experiments.

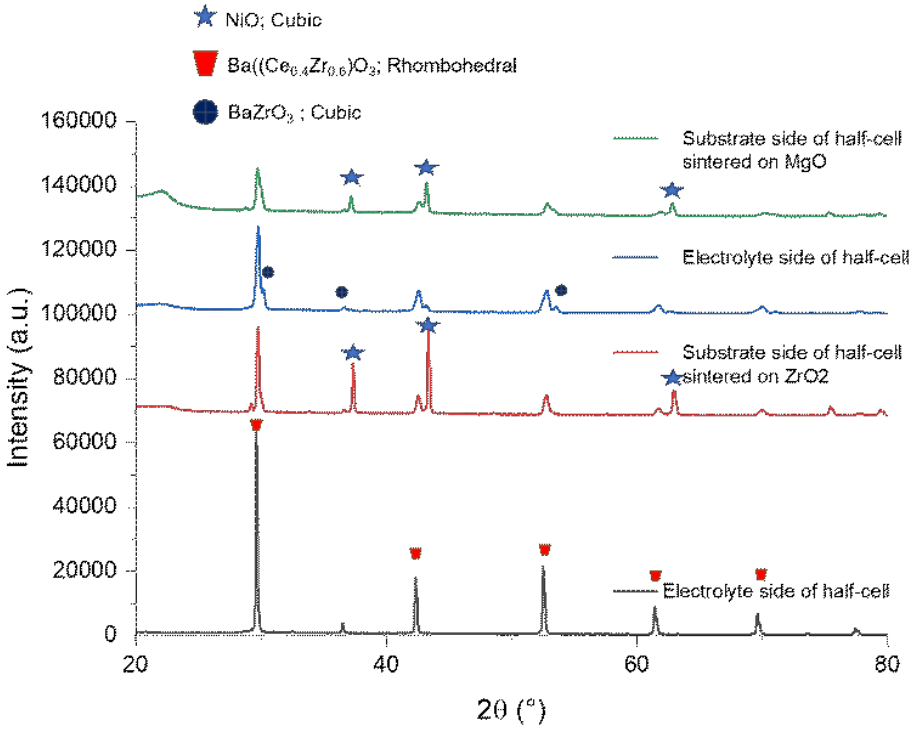

Figure 7-25: Comparison between XRD patterns of the electrolyte and the substrate side of half-cells sintered on top of MgO plates with a half-cell sintered on ZrO_2.

ZrO_2 vs. powder bed BZCY/NiO: Figure 7-26 shows two samples (KaroCast, Bilayer + single layer electrolyte laminated) sintered on different setter materials. The upper was placed inside an Al_2O_3 crucible on a BZCY/NiO powder bed, and another sample was sintered on a YSZ setter plate. The samples were heat-treated at the same time in the same furnace. The porosity of the electrolyte of the sample sintered on the ZrO_2 plate was significantly higher than that of the electrolyte of the sample sintered inside the crucible of sacrificial powder suggesting an atmospheric path of influence of the NiO in the powder bed as additional sintering additive. Additional differences become clear when the bottom side of the samples is investigated more closely. The substrate in contact with the Y- ZrO_2 setter plate loses some of its BZCY, leaving a skeletal structure of NiO and remnants of BZCY. However, at this position inside the structure, the BZCY does not contribute to the functioning of the cell. Only Nickel needs to form a percolating network through the electrode layer to ensure electronic conductivity. These results suggest that both possibilities are promising candidates for the large-scale samples.

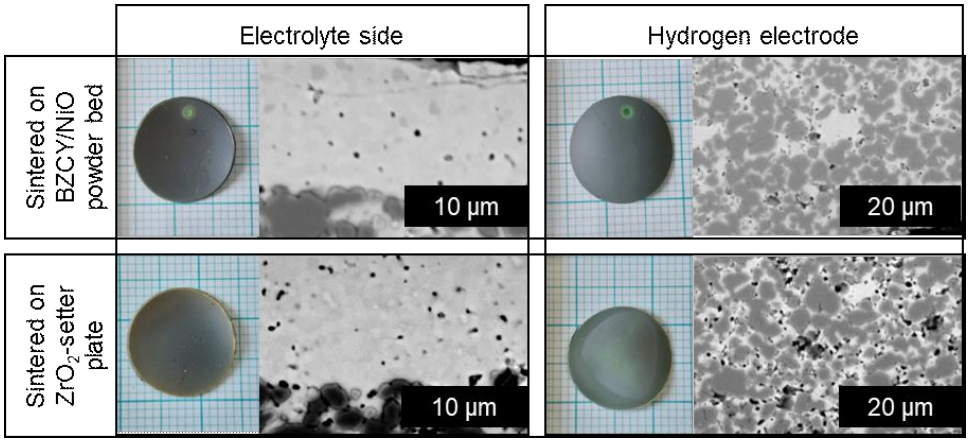

Figure 7-26: top) Sample sintered on BZCY/NiO powder bed showing uniform color but crack formation and surface defect, bottom) sample sintered on ZrO_2 plate with clear discoloration at the edges and on the electrode side where in contact with the setter plate (both KaroCast, Bilayer + single layer electrolyte laminated, 1550 °C).

First sintering of large-scale samples: As a final pretest, four large-scale (6.5 × 6.5 cm^2) bilayer sections with the optimized slurry composition, cast using both the JuCast and KaroCast systems, were sintered inside Al_2O_3 crucibles. One of the crucibles was filled with a BZCY/NiO powder bed. The results, shown in Figure 7-27, indicate a significantly greater extent of shattering for the KaroCast bilayers compared to the JuCast bilayers. This difference suggests that the improved quality of the tapes achieved through the transition to the large-scale JuCast tape caster was indeed successful. Overall, the results confirm the promise of using BZCY/NiO powder beds as a viable approach for achieving shatter-free sintering.

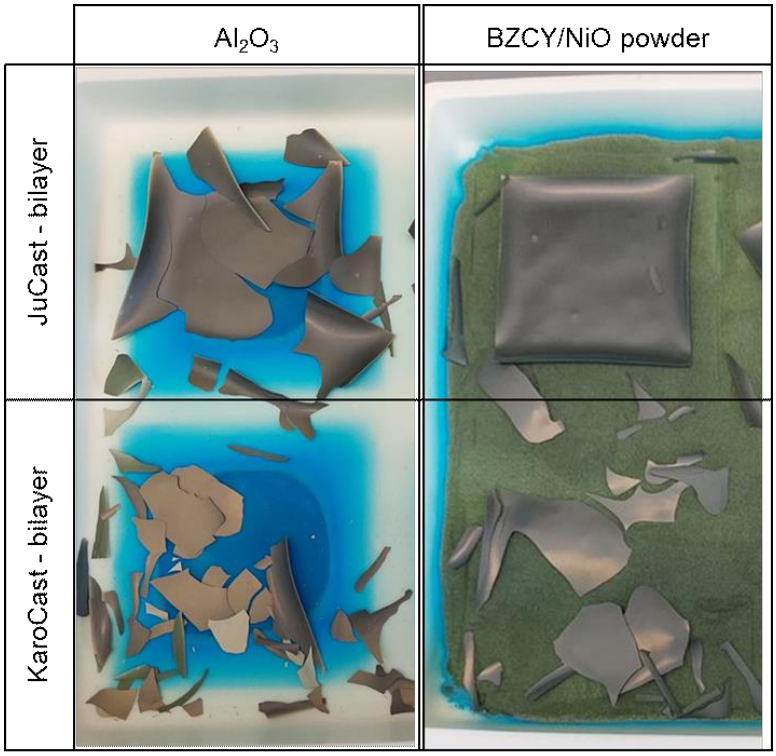

Figure 7-27: Large-scale bilayers sintered on two different setter materials. Differently strong shattering of the bilayer cast on JuCast and on KaroCast.

7.5.4 Conclusion of Pre-Tests

The pretests revealed that even comparable systems may respond unpredictably to changes in the sintering setup. Therefore, it is crucial to conduct tests using samples that closely resemble the final cells to be sintered. It was also emphasized that MgO is unsuitable for this composition due to its detrimental interactions with both sides of the bilayer. The impact of MgO on nickel loss was identified as a key factor contributing to the insufficient densification of the initial cells. In contrast, ZrO_2 and BZCY/NiO powder beds emerged as viable options for improved sintering setups. Another important change to the sintering procedure was the increase of maximum temperature to 1550 °C.

Additionally, it was demonstrated that the choice of setter plate influences electrolyte densification, even in cases where the plate is not in direct contact with the sample. The results further highlighted significant differences in sintering outcomes between bilayers produced via KaroCast and JuCast, underscoring the variability introduced by tape casting methods. Consequently, the subsequent sintering setup variations were conducted exclusively on JuCast bilayers to ensure consistency and reproducibility.

7.5.5 Experimental Set-Up: Warpage Mitigation Tests

For the second phase of the warpage mitigation tests, all prior findings informed the development of the strategies listed in Table 7-6. Several of these techniques performed well

individually; therefore, the second iteration of experiments incorporated combinations of these strategies to enhance their effectiveness.

Table 7-6: Mitigation strategies with their working principles and point of intervention during the processing.

Mitigation strategy	Working principle	Description
Usage of different setter plates or powder beds	Limiting nickel loss, changed sintering atmosphere	Al_2O_3, Y-ZrO_2 Y-ZrO_2 coated Al_2O_3 BZCY-NiO powder bed
Joining two bilayers	Creating of symmetric assembly to counteract shrinkage stresses	Laminated(El|Su + Su|El)
		Laminated(Su|El + El|Su)
Separate binder burnout and sintering	Allowing for furnace ventilation to remove organic residues to not influence furnace atmosphere	Standard binder burnout followed by a cooling to room temperature, followed by a standard sintering run
Combinations		
Joining two bilayers + usage of different setter plates		Laminated(El|Su + Su|El) on Al_2O_3 vs. ZrO_2
Joining two bilayers + different weights		ZrO_2 coated Al_2O_3 on Stacked(Su|El + El|Su) on BZCY/NiO powder bed
Joining four bilayers		Laminated(Su|El + El|Su) on top of Laminated(Su|El + El|Su) on BZCY/NiO powder bed
		Stacked(Su|El + El|Su + Su|El + El|Su) on BZCY/NiO powder bed
Weighted binder-burnout	Suppressing initial warpage due to binder burnout	Adding setter plate as weight on sample during binder burnout and removing weight for the sintering step on BZCY/NiO powder bed and Al_2O_3
Symmetric assembly as setter plate		Su|El on sintered Laminated(El|Su + Su|El) on BZCY/NiO powder bed

All samples underwent a heat-treatment procedure with a heating rate of 0.5 K/min up to 900 °C. For samples where the binder burnout and sintering steps were combined, the temperature was then increased to 1550 °C at a rate of 2 K/min, held for three hours, and subsequently cooled down to room temperature at 2 K/min. Samples with a separate binder burnout step were cooled from 900 °C to room temperature before being subjected to the same sintering procedure again alongside the other samples.

7.5.6 Results and Discussion: Warpage Mitigation Tests

Variation of setter plates: As shown in Figure 7-28, none of the setter plates tested were fully effective on their own. However, each setup exhibited distinct interactions with the bilayer. When the electrolyte side was in contact with the setter plate, it underwent a form of disintegration, completely separating from the electrode layer at the contact points. This behavior was observed for both Al_2O_3 and ZrO_2-coated Al_2O_3 setter plates. In contrast, samples with the electrode side in contact with the setter plate consistently experienced shattering,

regardless of the plate material used. The only setup that remained intact was the bilayer sintered on a BZCY/NiO powder bed. Based on these findings, it can be concluded that, in these cases, the only viable option for sintering is the BZCY/NiO powder bed.

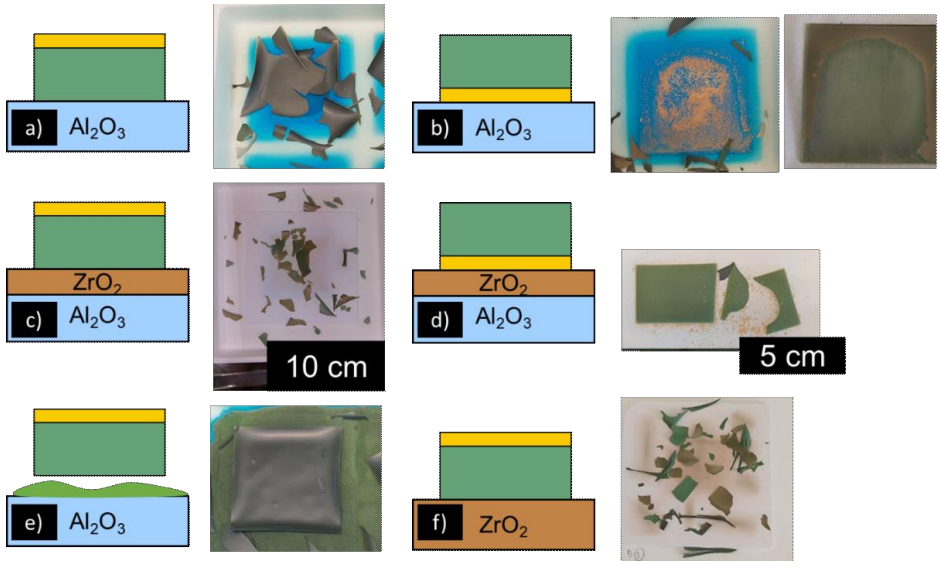

Figure 7-28: Outcome of sintering tests using different setter plates or powder bed.

Separation of binder burnout: On the left-hand side of Figure 7-29, two columns of bilayers are shown. The samples in the left column were first heat-treated to 900 °C for binder burnout, while those in the right column underwent direct sintering without a separate burnout step. It is evident that separating the burnout step improved the sintering success for these samples. However, the samples on the right, which were sintered on Al_2O_3 setter plates, showed an opposite trend. The samples that underwent a separate binder burnout step completely shattered, whereas those that combined the burnout and sintering steps showed fewer fractures.

An additional variation is visible in the rightmost column, where samples were first heat-treated for binder burnout, but with a 50 g setter plate placed on top of four bilayer samples during the burnout stage to suppress differential shrinkage and warpage. The setter plate was removed before the sintering stage. These samples exhibited significantly reduced shattering compared to those that underwent a separate burnout step without being weighted down.

These results demonstrate that the binder burnout procedure has a significant influence on the overall success of the sintering process. It is evident that the use of a setter plate during the binder burnout stage impacts the cell's behavior in the subsequent sintering stage. This finding highlights the potential for optimizing the binder burnout procedure to achieve improved warpage mitigation and overall sintering results.

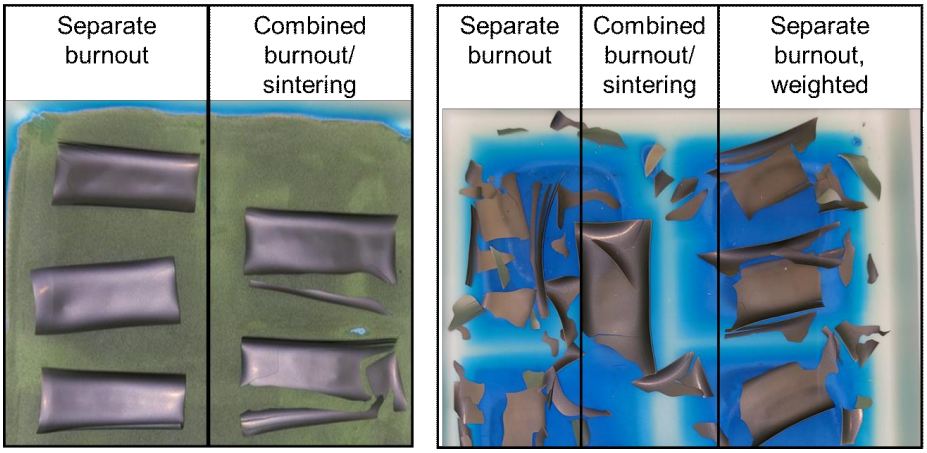

Figure 7-29: Influence of the separation of the burnout step on the sintering success depending on setter material used: left) BZCY/NiO-powder bed, right) Al_2O_3 setter plate.

Results of symmetric assemblies

Laminated (El|Su + Su|El): Samples with this structure consistently remained intact and exceptionally flat after sintering. Both Al_2O_3 and ZrO_2 setter plates ensured the planarity of the cells during sintering. However, as previously noted, the electrolyte layer in contact with Al_2O_3 was not preserved. Subsequent removal of the (compromised) electrolyte layer through grinding was limited by the scale of the cells. While this procedure is commonly used for achieving warpage-free pellets, it is not feasible for scaling, which is the focus of this thesis, for two key reasons: i) Any polishing or grinding step on non-embedded samples of this size introduces a significant risk of NiO contamination; ii) The handling complexity and effort required for such procedures would hinder their applicability in a scalable production process. However, this method of creating flat substrates enables the use of an alternative type of setter plate and weight: El|Su|Su|El assemblies. The use of these was tested, showed promising results and can be found in Supplementary Figure 12-7. Their use within the course of this thesis was however limited because the necessary size for such setter plates needs to be significantly larger than that of the cells in green state.

Stacked (Su|El + El|Su): The final two variations investigated were the tower assemblies. The first variation is shown in Figure 7-30. As demonstrated in previous experiments, a barrier of BZCY/NiO powder was necessary between the electrode and any setter plate to prevent nickel loss. On top of this powder bed, the first bilayer was placed with the electrolyte facing upward. To counteract the expected upward warpage, another bilayer was positioned on top, with its electrolyte layer facing downward. Based on findings from previous attempts with symmetrical cells, it was anticipated that these two layers would not sinter together but would instead delaminate easily.

To increase the weight on the samples and further mitigate warpage, two additional bilayers were stacked on top. As shown in Figure 7-30, not all samples remained intact; however, the extent of warpage was significantly reduced compared to samples sintered without the tower assembly. While the bilayers were not completely warped, the warpage appeared irregular and was attributed to the influence of the powder bed.

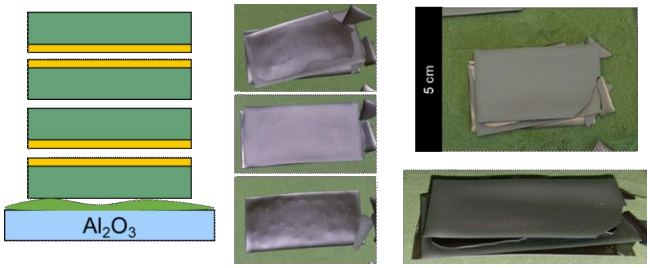

Figure 7-30: Self-weighted assembly of four bilayer samples, alternatingly stacked on a BZCY/NiO powder bed.

Laminated (Su|El + El|Su): To further improve the green stability during sintering and enhance planarity, a variation of the tower assembly was tested. This setup is shown in Figure 7-31, representing the final step in investigating warpage mitigation mechanisms. The key difference in this variation was the use of a warm press to laminate two sets of Su|El + El|Su assemblies prior to stacking them in a tower configuration.

After sintering, the bilayers remained (individually) intact and pairs partially delaminated. They also experienced significant warpage. However, the nature of this warpage differed from that observed in freely sintered samples. The lamination process constrained the middle sections of the bilayer pairs, leaving only the far corners free to warp upward, resulting in a unique shape. Unexpectedly, the maximum peak-to-valley difference for the stacked sample was 630 µm, while the laminated sample exhibited a larger difference of 1130 µm; 1.8 times greater than the stacked sample. The tower assembly without lamination was selected for half-cell processing, as it demonstrated better warpage mitigation and a more uniform sintering outcome.

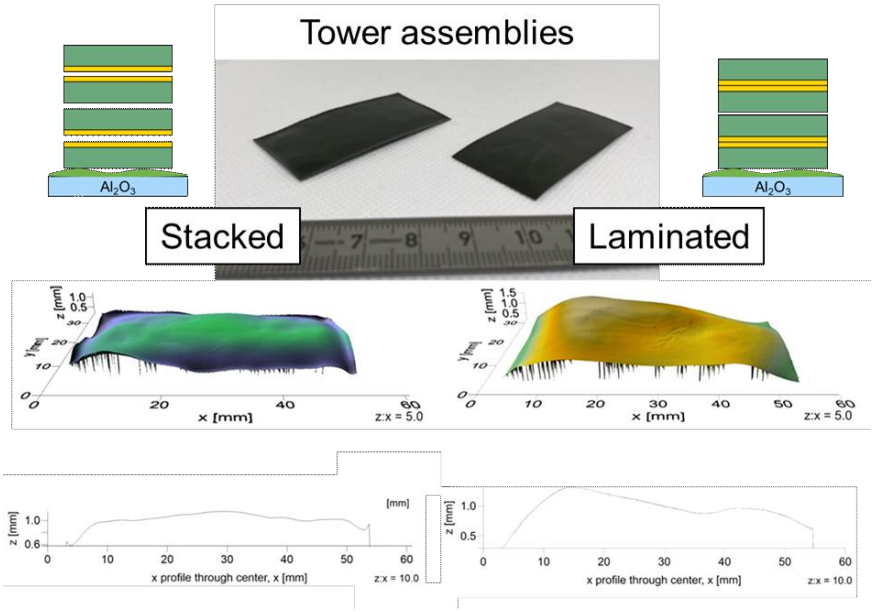

Figure 7-31: Stacked assembly of alternating bilayers of the Su|El + El|Su assembly stacked on top of each other. left) Without a lamination step, right) including a lamination step. (Cyberscan plot, z:x = 5, cross-section z:x = 10).

7.5.7 Conclusion

The warpage mitigation investigation identified three distinct improvements to the process: i) increase of sintering temperature to 1550 °C; ii) sintering on BZCY/NiO powder bed and iii) placing samples in a self-weighted alternatingly stacked tower assembly.

The best strategy to avoid cracking appeared to be to sinter on top of a BZCY/NiO powder bed. This helps with 1) potential Nickel loss to the setter plate, 2) barium loss due to evaporation, 3) BZCY interaction with the setter plate, 4) reducing friction between shrinking sample and setter plate, and 5) enhancing binder burnout due to the improved ventilation to the underside of the hydrogen electrode. However, the powder progressively coarsens and has to be mechanically removed from the crucible, ground and sieved to retain a high level of quality. This increased the experimental effort and the health hazard immensely and was deemed a non-scalable method but sufficient at this point in the development. (See supplementary Figure 12-8)

The most effective strategy for mitigating warpage appears to involve the application of a counteracting mechanical force to suppress deformation. This can be achieved through lamination to create symmetrical assemblies, the use of weights from the same sample, or alternating stacks of samples. The results also indicate an advantage in applying weights up until the completion of the binder burnout stage.

While the number of sintered samples remains low, it is acceptable to maintain a single furnace run that combines the binder burnout and sintering steps into one process. However, separating the binder burnout step and varying its parameters offer significant potential for future optimization.

7.6 Summary of Heat-Treatment Process Improvements and Potentials

This section provides an overview of the heat-treatment process improvements and the remaining potentials for further improvements or research.

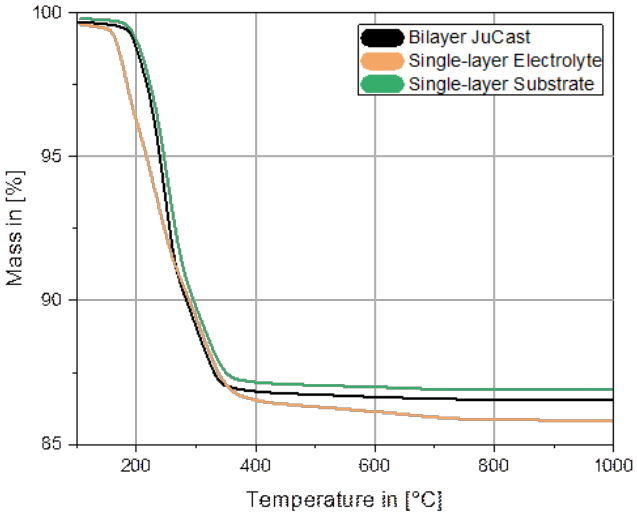

Figure 7-32: Comparison of burnout behavior of bilayer, electrolyte and electrode tapes prepared following the modified slurry preparation route cast on JuCast.

7.6.1 Burnout Optimization Potential

Figure 7-32 illustrates the mass loss curves of the JuCast bilayer, alongside the single-layer electrolyte and hydrogen electrode layer. As established through the thermogravimetric measurements earlier in this chapter, the burnout process is effectively complete by 400 °C.

This finding suggests potential for improving the efficiency of the heat-treatment procedure. Currently, the burnout step is designed to reach 900 °C, following a slow ramp rate of 0.5 K/min. Reducing the burnout temperature to 400 °C would significantly shorten the overall sintering time. Under the current procedure, the heat-treatment takes ~48 hours. By lowering the burnout temperature to 400 °C, the total processing time would be reduced to approximately 36 hours, representing a substantial time-saving and reduce occupancy of high-temperature furnaces while maintaining the necessary processing steps.

7.6.2 Half-Cell Microstructure along the Process

The half-cell undergoes significant microstructural changes during the binder burnout and sintering processes. Figure 7-33 illustrates three stages of the cell: after binder burnout, after sintering, and after reduction, as it would appear under operational conditions. The electrolyte layer experiences approximately 33 % shrinkage between the binder burnout and sintering stages. The density of both the electrolyte and electrode layers remain below 2 % after sintering. Following the reduction step, the electrode porosity increases to 19 %, enabling gas percolation through the layer.

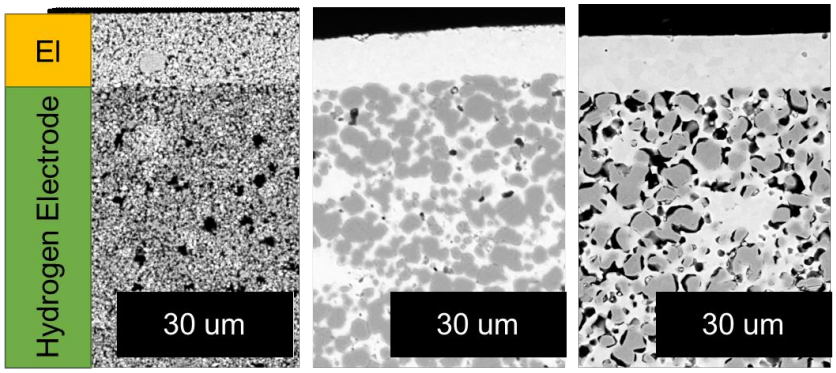

After	Binder burnout	Sintering	Reduction
Electrolyte porosity	Insufficient quality of microstructure image	< 2 %	< 2 %
Substrate porosity		< 2 %	~ 19 %

Figure 7-33: Development of the microstructure of the cell over the course of the heat-treatment.

This observation suggests another potential avenue for optimization: the precise tailoring of porosity content to mitigate warpage and to achieve optimal performance. For instance, pore formers could be added to increase overall porosity, or pore gradients could be introduced to enhance gas distribution. However, any such modification would necessitate a careful

reevaluation of differential shrinkage behavior to ensure structural integrity and performance consistency.

7.6.3 Double vs. Single Half-Cell Sintering

In a final comparison, laminated half-cells of the final structure (El|Su|Su) were sintered either as a stacked assembly (as shown in Figure 7-34 left)) or individually (right) on the ZrO_2 setter plate. The other successful approach using a BZCY/NiO powder bed was reserved for small-scale cells due to the health hazards of manually grinding the sacrificial powder to a functional size.

Figure 7-34 provides a clear depiction of the top and side views of both types of set-ups. Both samples show a significant improvement in warpage and surface quality compared to before the implementation of the optimization process. When comparing the half-cells to the bilayer samples in the section before, it was found that the addition of the substrate layer improved sample stability and also the appearance of irregular warpage.

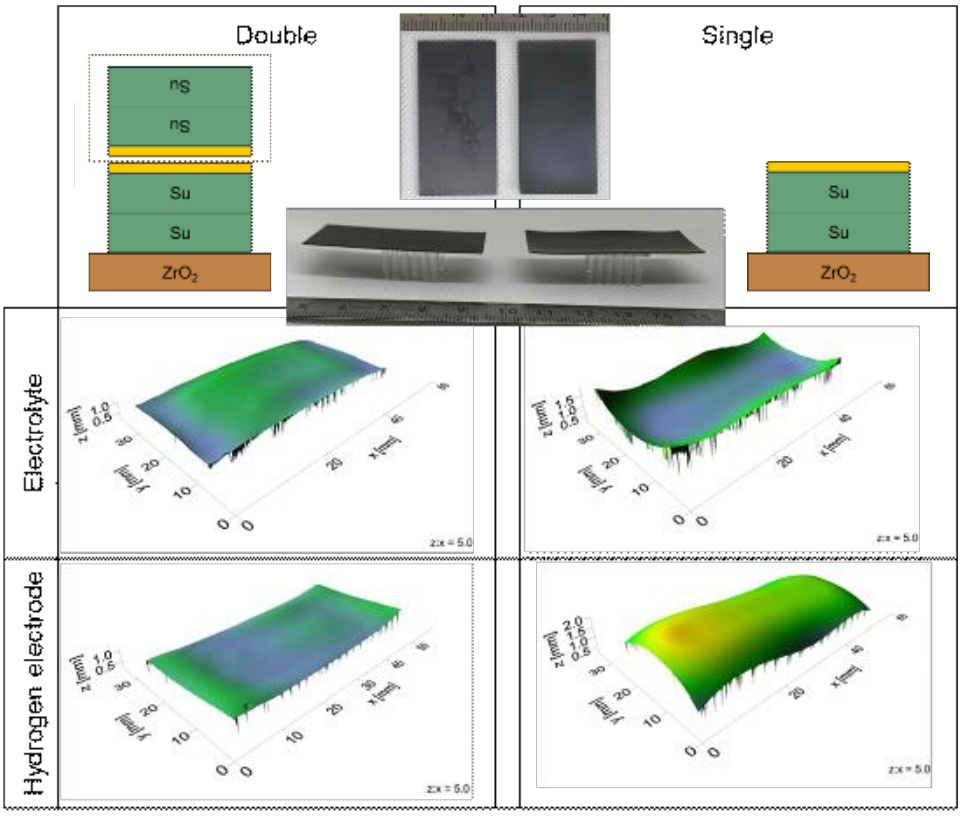

Figure 7-34: left) Half-cell sintered electrolyte facing another electrolyte layer, right) individually sintered.

The sample sintered directly on the YSZ setter plate (procured from Nikatto) without additional weight on top displays edge warpage whereas the stacked sample showed significantly less warpage. However, the image suggests the inversion of warpage tendencies (electrolyte side):

the stacked assembly showing convex and individually sintered samples concave warpage. Another observation was the formation of a surface pattern on the stacked half-cell's electrolyte side presumably due to some bonding of the electrolyte layers facing each other. These visual observations were supported by the quantification results in Figure 7-35.

Figure 7-35 presents the results of five cells sintered on ZrO_2 setter plates. These characteristics are derived from topography measurements of two pairs of stacked half-cells and two half-cells sintered without a cover. The data reveals notable trends. A comparison of maximum heights indicates that the half-cells sintered without a cover exhibit the highest 3D height maximums. Regarding warpage, the measurements clearly demonstrate that the warpage tendency observed in all samples sintered as doubles was reversed, confirming the effectiveness of the stacked assembly technique.

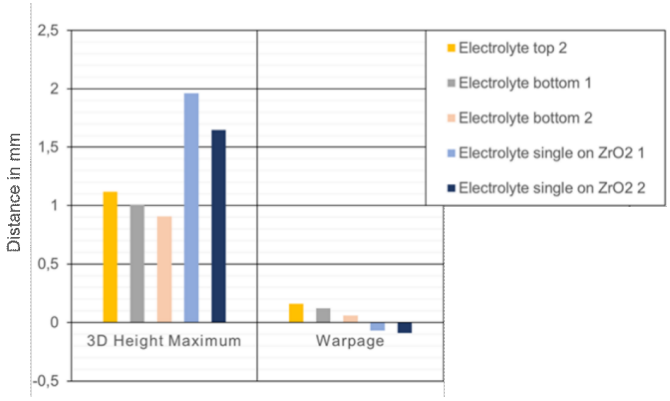

Figure 7-35: Surface quality analysis (Cyberscan) 3D height maximum and warpage.

Direct contact during sintering was further associated with increased surface roughness of the electrolyte. The implications of this observation are not yet fully understood. On the one hand, a rougher surface could enhance adhesion between the steam electrode and the electrolyte, potentially mitigating previously observed issues with electrode adherence. On the other hand, the increased roughness might also point to local defects within the electrolyte layer.

To assess the impact of this surface characteristic, all half-cells underwent ethanol-proofness testing, which serves as an initial indicator of sufficient gas tightness for further evaluations. The results confirmed that all samples met the required gas tightness standards for testing, underscoring the viability of the sintering process under these conditions.

8 Summary of Process Improvements

Based on the findings presented in this thesis, improving the manufacturing process requires several critical steps aimed at increasing the yield of large-scale cells. A final standard operating procedure is provided in the supplementary information. This section summarizes the key improvements across all stages of the process to establish a reliable production route for hydrogen electrode-supported cells.

The primary goal of this research was to develop a scalable and dependable process for producing larger quantities of cells with a target half-cell geometry of 25 × 50 mm^2, based on BZCY-721 electrolytes. Moving beyond the initial method that yielded only individual large-scale cells per production run, the focus shifted to increasing the overall yield while maintaining consistent quality. First of all, here a summary of the limitations of the initial process with regards to the abovementioned goals.

Early on, it became evident that the current in-house powder processing route using the solid-state reaction method produced powders of insufficient quality and quantity, i.e., formation of barium carbonates during milling steps, particle sizes of several µm in diameter, failure to produce single-phase powder. Attempts to scale up powder production revealed significant challenges, such as the capacity limits of available machines and associated peripherals, i.e., maximum loading sizes of mills. These limitations necessitated a reevaluation of powder sourcing strategy.

The preparation of slurries for larger batch sizes introduced additional challenges in maintaining consistent quality. As with the powders, the preparation had to be adjusted to using alternative machines due to insufficient max. allowed loading amounts of initially used devices. This adaptation created challenges with regards to process routes and increased preparation times due to changed dissolution speeds of binders. Increased batch sizes also forced the introduction of a de-airing step which could be omitted with smaller batches.

Furthermore, the tape casting process using the KaroCast tape caster presented issues of tape thickness variability and suboptimal surface quality, which was shown by topographical measurements and which directly impacted sintering success and overall cell yield.

The binder burnout process was shown to appear to be sensitive to the quantity of cells processed in a single furnace run due to the non-negligible amount of emitted organic components to the furnace atmosphere. This underscored the importance of controlling the effects of burnout products on sintering outcomes.

In addition to the initial limitations, the process changes introduced several new problems that also needed to be addressed.

Addressing the limitations in powder production led to a pivotal decision to transition to commercially sourced powders. However, this introduced batch-to-batch inconsistencies, particularly in particle size distribution and specific surface area. These inconsistencies required careful adaptation of slurry compositions, especially regarding dispersant amounts, to account for variations in powder properties. The importance of procuring a larger initial quantity from a single batch of powder became evident during this phase, as it helped reduce variability and enabled more consistent process optimization.

The discontinuation of in-house laser cutting due to safety concerns regarding NiO further complicated the production process. This change increased the necessity of producing cells with minimal warpage directly after sintering, as post-sintering cutting steps were no longer an option. To address this challenge, warpage mitigation strategies were prioritized, significantly altering the demands placed on tape casting and sintering processes.

Issues with the standard sintering set-up also emerged. The use of MgO setter plates, for instance, was found to alter the NiO content in the hydrogen electrode, inhibiting cell shrinkage and limiting the maximum achievable electrolyte density. This resulted in a NiO-depleted interface on the hydrogen electrode and porous electrolytes.

Another critical finding was related to the interaction of slurries based on unreacted SSRS powders, which led to excessive pinhole formation in the electrolyte layer during sequential tape casting. This issue highlighted the need for greater attention to chemical compatibility of the slurries during the casting process. Additionally, differences between the BZCY and BZCYYb systems posed unique challenges to the transfer of preparation processes, such as the formation of barium carbonate during the milling of BZCYYb. These findings underscore the need for tailored approaches to processing different stoichiometries.

Several process enhancements were identified as key contributors to improved outcomes. Scaling up the amounts of powder, slurry, and tape cast material reduced the influence of batch differences, fade-in and fade-out effects, and reservoir filling height variability during tape casting. These adjustments also allowed for more comprehensive quality control, such as viscosity checks, and improved the comparability of cells produced within the same batch. The increased scale enhanced overall efficiency by yielding a higher number of cells per tape.

The adaptation of the electrolyte slurry composition to exclude MEK proved transformative. This adjustment extended the stability of the slurry across a broader range of powders with varying specific surface areas, making it more robust against batch-to-batch differences. This improvement simplified handling and increased the reproducibility of the manufacturing process while at the same time limiting the use of the more harmful chemical MEK.

Using the JuCast tape caster instead of the KaroCast significantly improved tape quality and thickness uniformity, resulting in higher yields of successfully sintered half-cells and providing a greater quantity of usable tape for cell cutting. This upgrade was instrumental in addressing the challenges associated with the earlier tape casting method.

Improving tape quality and eliminating MgO setter plates were critical steps in mitigating sintering issues. These changes enhanced shrinkage behavior, prevented NiO depletion in the hydrogen electrode, and ensured better electrolyte density. Additionally, the adoption of self-weighted symmetrical assemblies effectively reduced warpage, contributing to the production of flatter cells directly after sintering.

This thesis has successfully addressed numerous initial limitations in the production of hydrogen electrode-supported cells and introduced robust solutions for manufacturing at a larger scale. The advancements in powder and slurry management, tape casting techniques, and sintering conditions have established a reliable and scalable production route. These findings not only enhance the immediate manufacturing process but also lay a solid foundation for future research and industrial applications.

9 Outlook

The findings of this thesis demonstrate the general manufacturability of PCECs on a larger scale and in acceptable quantities. Due to the comprehensive nature of investigating the entire preparation process of the cell, several open questions remain, presenting opportunities for further research and process improvements.

One significant area for future exploration is slurry conditioning. As highlighted in Chapter 5, there is substantial potential for optimizing slurry formulations and processing methods. In this work, the development approach relied on adapting the composition optimized for the micro tape caster KaroCast directly to the larger-scale JuCast system. Moving forward, this approach should be reconsidered. The JuCast use case should guide experimenters more closely to account for the shear stresses imposed on the slurry during the tape casting process. This stress state has a fundamental influence on tape quality and is highly dependent on the machine set-up. This information can then define the process shear stress range, informing adjustments to the slurry's viscosity. Moreover, viscosity measurement should become a standard practice during slurry preparation to ensure consistent and reproducible results.

Next, implementing controlled heating profiles is imperative. By carefully adjusting heating rates and temperature profiles during sintering, especially in the critical temperature range of 1400 °C to 1500 °C, where significant shrinkage mismatches have been observed, can reduce warpage further and ensure higher sample integrity. Furthermore, continuous monitoring and evaluation of microstructural changes using advanced microscopy techniques may provide real-time feedback on the effectiveness of these process improvements.

Lastly, validating these enhancements through comprehensive performance testing, including electrochemical measurements, will verify the impact on cell efficiency and durability. By systematically integrating these findings, the manufacturing process can be optimized to achieve higher yield and reliability of large-scale proton-conducting electrolysis cell production.

This thesis establishes a reliable procedure for the production of half-cells that meet the requirements for flatness necessary for screen-printing and electrochemical testing. However, half-cells represent only a step—albeit a significant one—towards the preparation of full cells. Therefore, preparing and testing full cells is the immediate next step. At the time of writing, both small-scale and large-scale half-cells were successfully prepared as full cells by research partners, demonstrating the overall success of the warpage mitigation efforts. Additionally, small-scale cells underwent successful testing (detailed results are not yet available), confirming the viability of the entire process. Following this, the electrochemical performance of the full cells should be systematically characterized. Insights from this characterization can then be used to target specific optimizations, such as refining the microstructure through modifications in powder processing or the incorporation of pore formers.

Another critical area of focus is improving the robustness of the process against variability caused by batch differences, which may lead to unexpected slurry behavior. Achieving this goal requires a deeper understanding of the system to enable tailored adjustments to the slurry and casting parameters. Improved documentation and detailed tracking of casting conditions are

essential, along with efforts to minimize the influence of human factors. This would represent a significant step toward achieving a higher TRL for PCECs.

Moreover, the reproducible fabrication of half-cells developed in this work directly supports electrode development—a current hot topic in the field. Reliable half-cell production enhances the comparability of results and ensures greater consistency in electrode performance.

Further advancements are also required in understanding the sintering processes. As discussed in Chapter 7, several observed sintering phenomena cannot yet be fully attributed to specific mechanisms. For progress in this area, it will be crucial to identify and control these mechanisms, which would significantly enhance the scalability and reliability of the process. Additionally, a deeper investigation into the formation, melting, and partial reintegration of the transient liquid phase in the microstructure is necessary. Advanced techniques such as further TEM analyses could provide valuable insights here.

Overall, this thesis represents a substantial contribution to advancing the technological readiness level of PCECs. It identifies systematic shortcomings in current processes and proposes actionable solutions, providing a solid foundation for future research and development in the field.

10 Acknowledgements

I thank Prof. Dr. Olivier Guillon and Dr. Mariya Ivanova for the opportunity to pursue my doctoral research at the Forschungszentrum Jülich. I also acknowledge financial support from the Helmholtz Innovation Pool "Solar Hydrogen – highly pure and compressed", which made this work possible.

I acknowledge the use of large language models and AI-assisted tools, including ChatGPT, Scite.ai and Perplexity. These tools were used for language refinement and literature exploration. All scientific interpretation and conclusions presented in this thesis remain my own.

Although a PhD thesis carries a single name, it is shaped by many people, ideas and shared experiences. I am grateful to Prof. Dr. Norbert Menzler, as well as to the colleagues in his department, for their openness, long-term experience and the insights they shared on solid oxide cell development. I would particularly like to thank Ralf Kauert for sharing the challenges of temperamental tape casting machines and for his practical understanding, which often resolved problems faster than any literature search.

Thanks are due to the many fellow PhD students, technical staff and senior researchers (within and beyond Forschungszentrum Jülich) who contributed through discussions, feedback and shared attempts at solving problems. In particular, I would like to thank Dr. Yuan Zeng for honest, direct and consistently constructive feedback, and for keeping discussions focused without ever discouraging them. My sincere thanks go to Dr. Denise Ramler and Dr. Franziska Winterhalder, whose shared engineering perspective and openness to different approaches were especially valuable and who were always willing to listen—to research challenges as well as the latest developments in our Pen and Paper campaign. I also thank Dr. Johannes-Christian Schmitt, the best office mate one could hope for, for his support and good humor throughout this time.

All colleagues and students whom I had the opportunity to teach also deserve my thanks. Teaching proved to be an effective way of testing and refining the ideas developed in this thesis and, importantly, it was fun. I would like to thank Sascha Shardimgaliev for his engagement and contribution during this time.

Particular gratitude goes to Dr. Hans-Peter Buchkremer for his consistent support, for listening when perspective was needed and for his dependable willingness to advocate and facilitate the right connections at the right time.

I would also like to thank Ebru Gyoktepeliler Akin and Pascal Zahler for their support during the final phases of this work. Simply working alongside each other, mostly in silence, created a shared sense of accountability that made this phase significantly easier to navigate.

Finally, I thank my parents, Anke and Konrad Schäfer, my grandparents, Marliese and Kurt Schäfer and Karin Rauscher for their unwavering encouragement, patience and genuine interest in my work. My family has supported me in every endeavor I set my mind to, be it time spent abroad, multiple changes of university, or a stubborn childhood conviction that I wanted to pursue a PhD long before I even knew in which discipline.

11 Literature

[1] H. Ding, W. Wu, C. Jiang, Y. Ding, W. Bian, B. Hu, P. Singh, C.J. Orme, L. Wang, Y. Zhang, D. Ding, Self-Sustainable Protonic Ceramic Electrochemical Cells Using a Triple Conducting Electrode for Hydrogen and Power Production, Nature Communications 11 (2020). https://doi.org/10.1038/s41467-020-15677-z.

[2] M. Wang, W. Wu, Y. Lin, W. Tang, G. Gao, H. Li, F.F. Stewart, L.-C. Wang, Y. Yang, D. Ding, Improved Solid-State Reaction Method for Scaled-Up Synthesis of Ceramic Proton-Conducting Electrolyte Materials, Acs Applied Energy Materials 6 (2023) 8316–8326. https://doi.org/10.1021/acsaem.3c01423.

[3] S. Ricote, N. Bonanos, A. Manerbino, N. P. Sullivan, W. G. Coors, Effects of the fabrication process on the grain-boundary resistance in $BaZr_{0.9}Y_{0.1}O_{3-\delta}$, Journal of Materials Chemistry A 2 (2014) 16107–16115. https://doi.org/10.1039/C4TA02848A.

[4] W. Deibert, M.E. Ivanova, Y. Huang, R. Merkle, J. Maier, W.A. Meulenberg, Fabrication of multi-layered structures for proton conducting ceramic cells, J. Mater. Chem. A (2021) 10.1039.D1TA05240C. https://doi.org/10.1039/D1TA05240C.

[5] K. Leonard, Y. Okuyama, Y. Takamura, Y.-S. Lee, K. Miyazaki, M.E. Ivanova, W.A. Meulenberg, H. Matsumoto, Efficient intermediate-temperature steam electrolysis with Y : $SrZrO_3$–$SrCeO_3$ and Y : $BaZrO_3$–$BaCeO_3$ proton conducting perovskites, J. Mater. Chem. A 6 (2018) 19113–19124. https://doi.org/10.1039/C8TA04019B.

[6] W. Deibert, M.E. Ivanova, Entwicklung von protonenleitenden Membranen mit optimierter Mikrostruktur und verbesserten Transporteigenschaften für Energie- und Wasserstoffseparationsanwendungen - ProtoMem : Schlussbericht zum Teilprojekt : Projektlaufzeit: 01.07.2016-30.06.2019, [Forschungszentrum Jülich], 2019. https://doi.org/10.2314/KXP:1689694440.

[7] Directorate-General for Energy (European Commission), Guidehouse, Tractebel Impact, J. Jens, J. Cihlar, K. van der Leun, F. Melgar, P. Rio, A. Villar Lejarreta, A. Wang, Hydrogen generation in Europe: overview of costs and key benefits, Publications Office of the European Union, LU, 2020. https://data.europa.eu/doi/10.2833/122757 (accessed August 8, 2021).

[8] J. Andersson, S. Grönkvist, Large-scale storage of hydrogen, International Journal of Hydrogen Energy 44 (2019) 11901–11919. https://doi.org/10.1016/j.ijhydene.2019.03.063.

[9] N. Shimoda, Y. Kobayashi, Y. Kimura, G. Nakagawa, S. Satokawa, Electrochemical synthesis of ammonia using a proton conducting solid electrolyte and nickel cermet electrode, J. Ceram. Soc. Japan 125 (2017) 252–256. https://doi.org/10.2109/jcersj2.16286.

[10] A. Hauch, R. Küngas, P. Blennow, A.B. Hansen, J.B. Hansen, B.V. Mathiesen, M.B. Mogensen, Recent advances in solid oxide cell technology for electrolysis, Science 370 (2020) eaba6118. https://doi.org/10.1126/science.aba6118.

[11] M.E. Ivanova, R. Peters, M. Müller, S. Haas, M.F. Seidler, G. Mutschke, K. Eckert, P. Röse, S. Calnan, R. Bagacki, R. Schlatmann, C. Grosselindemann, L.-A. Schäfer, N.H. Menzler, A. Weber, R. van de Krol, F. Liang, F.F. Abdi, S. Brendelberger, N. Neumann, J. Grobbel, M. Roeb, C. Sattler, I. Duran, B. Dietrich, M.E.C. Hofberger, L. Stoppel, N. Uhlenbruck, T. Wetzel, D. Rauner, A. Hecimovic, U. Fantz, N. Kulyk, J. Harting, O. Guillon, Technological Pathways to Produce Compressed and Highly Pure Hydrogen

from Solar Power, Angewandte Chemie International Edition 62 (2023) e202218850. https://doi.org/10.1002/anie.202218850.

[12] Ministerial Council on Renewable Energy - Hydrogen and Related Issues, Basic Hydrogen Strategy, 2017.

[13] E. Vøllestad, R. Strandbakke, M. Tarach, D. Catalán-Martínez, M.-L. Fontaine, D. Beeaff, D.R. Clark, J.M. Serra, T. Norby, Mixed proton and electron conducting double perovskite anodes for stable and efficient tubular proton ceramic electrolysers, Nature Materials 18 (2019) 752–759. https://doi.org/10.1038/s41563-019-0388-2.

[14] Hydrogen as fuel for fuel cell electric vehicles, (n.d.). https://www.ieafuelcell.com/index.php?id=33 (accessed December 19, 2024).

[15] European Commission. Joint Research Centre., EU harmonised terminology for hydrogen generated by electrolysis., Publications Office, LU, 2021. https://data.europa.eu/doi/10.2760/732809 (accessed August 11, 2021).

[16] H.-I. Ji, J.-H. Lee, J.-W. Son, K.J. Yoon, S. Yang, B.-K. Kim, Protonic ceramic electrolysis cells for fuel production: a brief review, J. Korean Ceram. Soc. 57 (2020) 480–494. https://doi.org/10.1007/s43207-020-00059-4.

[17] K.-D. Kreuer, Proton-Conducting Oxides, Annu. Rev. Mater. Res. 33 (2003) 333–359. https://doi.org/10.1146/annurev.matsci.33.022802.091825.

[18] J.-C. Grenier, Proton Transport Mechanism, in: Proton-Conducting Ceramics: From Fundamentals to Applied Research, Pan Stanford Publishing, Singapore, 2016: pp. 9–12.

[19] W. Münch, G. Seifert, K.D. Kreuer, J. Maier, A quantum molecular dynamics study of proton conduction phenomena in BaCeO3, Solid State Ionics 86–88 (1996) 647–652. https://doi.org/10.1016/0167-2738(96)00229-9.

[20] W. Münch, K.D. Kreuer, S. Adams, G. Seifert, J. Maier, The relation between crystal structure and the formation and mobility of protonic charge carriers in perovskite-type oxides: A case study of Y-doped BaCeO3 and SrCeO3, Phase Transitions 68 (1999) 567–586. https://doi.org/10.1080/01411599908224535.

[21] D. Poetzsch, R. Merkle, J. Maier, Proton conductivity in mixed-conducting BSFZ perovskite from thermogravimetric relaxation, Phys. Chem. Chem. Phys. 16 (2014) 16446–16453. https://doi.org/10.1039/C4CP00459K.

[22] J.A. Wrubel, J. Gifford, Z. Ma, H. Ding, D. Ding, T. Zhu, Modeling the performance and faradaic efficiency of solid oxide electrolysis cells using doped barium zirconate perovskite electrolytes, Int. J. Hydrog. Energy 46 (2021) 11511–11522. https://doi.org/10.1016/j.ijhydene.2021.01.043.

[23] D. Poetzsch, R. Merkle, J. Maier, Proton uptake in the H^+-SOFC cathode material $Ba_{0.5}Sr_{0.5}Fe_{0.8}Zn_{0.2}O_{3-\delta}$: transition from hydration to hydrogenation with increasing oxygen partial pressure, Faraday Discuss. 182 (2015) 129–143. https://doi.org/10.1039/C5FD00013K.

[24] M. Papac, V. Stevanović, A. Zakutayev, R. O'Hayre, Triple ionic–electronic conducting oxides for next-generation electrochemical devices, Nature Materials 20 (2021) 301–313. https://doi.org/10.1038/s41563-020-00854-8.

[25] H. Zhu, S. Ricote, W.G. Coors, R.J. Kee, Interpreting equilibrium-conductivity and conductivity-relaxation measurements to establish thermodynamic and transport properties for multiple charged defect conducting ceramics, Faraday Discuss. 182 (2015) 49–74. https://doi.org/10.1039/C5FD00012B.

[26] C. Duan, R. Kee, H. Zhu, N. Sullivan, L. Zhu, L. Bian, D. Jennings, R. O'Hayre, Highly efficient reversible protonic ceramic electrochemical cells for power generation and fuel production, Nature Energy 4 (2019) 230–240. https://doi.org/10.1038/s41560-019-0333-2.

[27] R.J. Braun, A. Dubois, K. Ferguson, C. Duan, C. Karakaya, R.J. Kee, H. Zhu, N.P. Sullivan, E. Tang, M. Pastula, A. Wood, T. Joia, R. O'Hayre, Development of kW-Scale Protonic Ceramic Fuel Cells and Systems, ECS Trans. 91 (2019) 997. https://doi.org/10.1149/09101.0997ecst.

[28] M. Ni, M.K.H. Leung, D.Y.C. Leung, Technological development of hydrogen production by solid oxide electrolyzer cell (SOEC), International Journal of Hydrogen Energy 33 (2008) 2337–2354. https://doi.org/10.1016/j.ijhydene.2008.02.048.

[29] R. Hino, K. Haga, H. Aita, K. Sekita, 38. R&D on hydrogen production by high-temperature electrolysis of steam, Nuclear Engineering and Design 233 (2004) 363–375. https://doi.org/10.1016/j.nucengdes.2004.08.029.

[30] M. Kemm, C. Stiller, A. Selimovic, B. Thorud, T. Torisson, O. Holland, Planar and Tubular Solid Oxide Fuel Cells: A Comparison of Transient Process Behaviors, ECS Proceedings Volumes 2005–07 (2005) 659–669. https://doi.org/10.1149/200507.0659PV.

[31] W. Schafbauer, F. Schulze-Küppers, S. Baumann, W.A. Meulenberg, N.H. Menzler, H.P. Buchkremer, D. Stöver, Tape Casting as a Multi Purpose Shaping Technology for Different Applications in Energy Issues, Materials Science Forum 706–709 (2012) 1035–1040. https://doi.org/10.4028/www.scientific.net/MSF.706-709.1035.

[32] N.H. Menzler, F. Tietz, S. Uhlenbruck, H.P. Buchkremer, D. Stöver, Materials and manufacturing technologies for solid oxide fuel cells, J Mater Sci 45 (2010) 3109–3135. https://doi.org/10.1007/s10853-010-4279-9.

[33] N.H. Menzler, J. Malzbender, P. Schoderböck, R. Kauert, H.P. Buchkremer, Sequential Tape Casting of Anode-Supported Solid Oxide Fuel Cells, Fuel Cells 14 (2014) 96–106. https://doi.org/10.1002/fuce.201300153.

[34] M. Shirpour, R. Merkle, J. Maier, Evidence for space charge effects in Y-doped $BaZrO_3$ from reduction experiments, Solid State Ionics 216 (2012) 1–5. https://doi.org/10.1016/j.ssi.2011.09.006.

[35] J. Lü, L. Wang, L. Fan, Y. Li, L. Dai, H. Guo, Chemical stability of doped $BaCeO_3$-$BaZrO_3$ solid solutions in different atmospheres, Journal of Rare Earths 26 (2008) 505–510. https://doi.org/10.1016/S1002-0721(08)60127-1.

[36] T. Das, J.D. Nicholas, B.W. Sheldon, Y. Qi, Anisotropic chemical strain in cubic ceria due to oxygen-vacancy-induced elastic dipoles, Phys. Chem. Chem. Phys. 20 (2018) 15293–15299. https://doi.org/10.1039/C8CP01219A.

[37] L. Yang, S. Wang, K. Blinn, M. Liu, Z. Liu, Z. Cheng, M. Liu, Enhanced sulfur and coking tolerance of a mixed ion conductor for SOFCs: $BaZr_{0.1}Ce_{0.7}Y_{0.2-x}Yb_xO_{3-\delta}$, Science 326 (2009) 126–129. https://doi.org/10.1126/science.1174811.

[38] S. Choi, C.J. Kucharczyk, Y. Liang, X. Zhang, I. Takeuchi, H.-I. Ji, S.M. Haile, Exceptional power density and stability at intermediate temperatures in protonic ceramic fuel cells, Nature Energy 3 (2018) 202–210. https://doi.org/10.1038/s41560-017-0085-9.

[39] Z. Wang, Z. Luo, H. Xu, T. Zhu, D. Guan, Z. Lin, T.-S. Chan, Y.-C. Huang, Z. Hu, S.P. Jiang, Z. Shao, New Understanding and Improvement in Sintering Behavior of Cerium-

Rich Perovskite-Type Protonic Electrolytes, Advanced Functional Materials 34 (2024) 2402716. https://doi.org/10.1002/adfm.202402716.

[40] D. Jennings, J.N. Ebert, H. Du, Q. Ma, L.-A. Schäfer, D. Sebold, J. Mayer, W. Rheinheimer, The Formation of Stacking Faults in Barium Zirconate-Type Perovskites, Chem. Mater. 35 (2023) 8382–8396. https://doi.org/10.1021/acs.chemmater.3c00787.

[41] M. Balaguer, Y.J. Sohn, D. Kobertz, S. Kasatikov, A. Fantin, M. Müller, N.H. Menzler, O. Guillon, M.E. Ivanova, Characterization of Y and Mn co-substituted $BaZrO_3$ ceramics: Material properties as a function of the substituent concentration, Solid State Ionics 382 (2022) 115959. https://doi.org/10.1016/j.ssi.2022.115959.

[42] S. Nikodemski, J. Tong, R. O'Hayre, Solid-state reactive sintering mechanism for proton conducting ceramics, Solid State Ionics 253 (2013) 201–210. https://doi.org/10.1016/j.ssi.2013.09.025.

[43] J. Li, C. Wang, X. Wang, L. Bi, Sintering aids for proton-conducting oxides – A double-edged sword? A mini review, Electrochemistry Communications 112 (2020) 106672. https://doi.org/10.1016/j.elecom.2020.106672.

[44] H.-I. Ji, B.-K. Kim, J.-W. Son, K.J. Yoon, J.-H. Lee, Influence of sintering activators on electrical property of $BaZr_{0.85}Y_{0.15}O_{3-\delta}$ proton-conducting electrolyte, Journal of Power Sources 507 (2021) 230296. https://doi.org/10.1016/j.jpowsour.2021.230296.

[45] C.A. Goulart, L.A.V. Boas, M.R. Morelli, D.P.F. de Souza, Reactive sintering of yttrium-doped barium zirconate ($BaZr_{0.8}Y_{0.2}O_{3-\delta}$) without sintering aids, Ceramics International 47 (2021) 2565–2571. https://doi.org/10.1016/j.ceramint.2020.09.102.

[46] H. Matsumoto, T. Sakai, Y. Okuyama, Proton-conducting oxide and applications to hydrogen energy devices, Pure and Applied Chemistry 85 (2012) 427–435. https://doi.org/10.1351/PAC-CON-12-07-11.

[47] K. Leonard, M.E. Ivanova, A. Weber, W. Deibert, W.A. Meulenberg, T. Ishihara, H. Matsumoto, Anode supported planar 5 × 5 cm^2 $SrZr_{0.5}Ce_{0.4}Y_{0.1}O_{2.95}$ based solid oxide protonic fuel cells via sequential tape-casting, Solid State Ionics 379 (2022) 115918. https://doi.org/10.1016/j.ssi.2022.115918.

[48] L. Lei, J. Zhang, Z. Yuan, J. Liu, M. Ni, F. Chen, Progress Report on Proton Conducting Solid Oxide Electrolysis Cells, Adv. Funct. Mater. 29 (2019) 1903805. https://doi.org/10.1002/adfm.201903805.

[49] Y. Zhou, E. Liu, Y. Chen, Y. Liu, L. Zhang, W. Zhang, Z. Luo, N. Kane, B. Zhao, L. Soule, Y. Niu, Y. Ding, H. Ding, D. Ding, M. Liu, An Active and Robust Air Electrode for Reversible Protonic Ceramic Electrochemical Cells, ACS Energy Lett. 6 (2021) 1511–1520. https://doi.org/10.1021/acsenergylett.1c00432.

[50] S. Choi, T.C. Davenport, S.M. Haile, Protonic ceramic electrochemical cells for hydrogen production and electricity generation: exceptional reversibility, stability, and demonstrated faradaic efficiency, Energy Environ. Sci. 12 (2019) 206–215. https://doi.org/10.1039/C8EE02865F.

[51] M. Choi, S.J. Kim, W. Lee, Effects of water atmosphere on chemical degradation of $PrBa_{0.5}Sr_{0.5}Co_{1.5}Fe_{0.5}O_{5+\delta}$ electrodes, Ceramics International 47 (2021) 7790–7797. https://doi.org/10.1016/j.ceramint.2020.11.124.

[52] L. Zhang, W. Yang, High-performance low-temperature solid oxide fuel cells using thin proton-conducting electrolyte with novel cathode, International Journal of Hydrogen Energy 37 (2012) 8635–8640. https://doi.org/10.1016/j.ijhydene.2012.02.140.

[53] R. Strandbakke, E. Vøllestad, S.A. Robinson, M.-L. Fontaine, T. Norby, $Ba_{0.5}Gd_{0.8}La_{0.7}Co_2O_{6-\delta}$ Infiltrated in Porous $BaZr_{0.7}Ce_{0.2}Y_{0.1}O_3$ Backbones as Electrode Material for Proton Ceramic Electrolytes, J. Electrochem. Soc. 164 (2017) F196. https://doi.org/10.1149/2.0141704jes.

[54] Q. Liu, C. Yang, X. Dong, F. Chen, Perovskite $Sr_2Fe_{1.5}Mo_{0.5}O_{6-\delta}$ as electrode materials for symmetrical solid oxide electrolysis cells, International Journal of Hydrogen Energy 35 (2010) 10039–10044. https://doi.org/10.1016/j.ijhydene.2010.08.016.

[55] Salmang, Scholze, Keramik, Springer Berlin Heidelberg, 2007. https://doi.org/10.1007/978-3-540-49469-0.

[56] J. Tong, D. Clark, L. Bernau, M. Sanders, R. O'Hayre, Solid-state reactive sintering mechanism for large-grained yttrium-doped barium zirconate proton conducting ceramics, J. Mater. Chem. 20 (2010) 6333–6341. https://doi.org/10.1039/C0JM00381F.

[57] M. Marrony, ed., Proton-conducting ceramics: from fundamentals to applied research, Pan Stanford Publishing, Singapore, 2016.

[58] M. Klee, Concise encyclopedia of advanced ceramic materials. Edited by R. J. Brook, Pergamon, Oxford 1991, 588 pp., hardcover, £ 110, ISBN 0-08-034720-78, Advanced Materials 4 (1992) 826–827. https://doi.org/10.1002/adma.19920041217.

[59] M.N. Rahaman, Ceramic processing, Second edition, Taylor & Francis, CRC Press, Boca Raton, 2017.

[60] S.J. Glass, K.G. Ewsuk, Ceramic Powder Compaction, MRS Bulletin 22 (1997) 24–28. https://doi.org/10.1557/S0883769400034709.

[61] J.S. Reed, Principles of ceramics processing, 2nd ed, Wiley, New York, 1995.

[62] W. Schafbauer, Entwicklung und Herstellung von foliengegossenen, anodengestützten Festoxidbrennstoffzellen, Forschungszentrum Jülich, Jülich, 2010.

[63] R.E. Mistler, E.R. Twiname, Tape casting: theory and practice, American Ceramic Society, Westerville, OH, 2000.

[64] A. Demarbaix, F. Ducobu, N. Preux, F. Petit, E. Rivière-Lorphèvre, Green Ceramic Machining: Influence of the Cutting Speed and the Binder Percentage on the Y-TZP Behavior, Journal of Manufacturing and Materials Processing 4 (2020) 50. https://doi.org/10.3390/jmmp4020050.

[65] R.E. Mistler, The principles of tape casting and tape casting applications, in: R.A. Terpstra, P.P.A.C. Pex, A.H. de Vries (Eds.), Ceramic Processing, Springer Netherlands, Dordrecht, 1995: pp. 147–173. https://doi.org/10.1007/978-94-011-0531-6_5.

[66] D.J. Shanefield, Organic Additives and Ceramic Processing, Springer US, Boston, MA, 1995. https://doi.org/10.1007/978-1-4757-6103-0.

[67] M. Jabbari, R. Bulatova, A.I.Y. Tok, C.R.H. Bahl, E. Mitsoulis, J.H. Hattel, Ceramic tape casting: A review of current methods and trends with emphasis on rheological behaviour and flow analysis, Materials Science and Engineering: B 212 (2016) 39–61. https://doi.org/10.1016/j.mseb.2016.07.011.

[68] G.G. Stokes, On the Theories of the Internal Friction of Fluids in Motion, and of the Equilibrium and Motion of Elastic Solids, in: M.A. Pelissier, H. Hoeber, N. van de Coevering, I.F. Jones, D.A. Ebrom, M.A. Pelissier (Eds.), Classics of Elastic Wave Theory, Society of Exploration Geophysicists, 2007: p. 0. https://doi.org/10.1190/1.9781560801931.ch3e.

[69] S. Masia, P.D. Calvert, W.E. Rhine, H.K. Bowen, Effect of oxides on binder burnout during ceramics processing, J Mater Sci 24 (1989) 1907–1912. https://doi.org/10.1007/BF02385397.

[70] P. Vozdecky, A. Roosen, Q. Ma, F. Tietz, H.P. Buchkremer, Properties of tape-cast Y-substituted strontium titanate for planar anode substrates in SOFC applications, J Mater Sci 46 (2011) 3493–3499. https://doi.org/10.1007/s10853-011-5255-8.

[71] Z. Fu, P. Polfer, T. Kraft, A. Roosen, Correlation Between Anisotropic Green Microstructure of Spherical-Shaped Alumina Particles and Their Shrinkage Behavior, Journal of the American Ceramic Society 98 (2015) 3438–3444. https://doi.org/10.1111/jace.13567.

[72] P. Fedeli, F. Drago, F. Schulze-Küppers, S. Baumann, Asymmetric LSCF Membranes Utilizing Commercial Powders, Materials 13 (2020) 614. https://doi.org/10.3390/ma13030614.

[73] M.N. Rahaman, Sintering of Ceramics, CRC Press, Boca Raton, 2013. https://doi.org/10.1201/b15869.

[74] D.S. Wilkinson, M.F. Ashby, The Development of Pressure Sintering Maps, in: G.C. Kuczynski (Ed.), Sintering and Catalysis, Springer US, Boston, MA, 1975: pp. 473–492. https://doi.org/10.1007/978-1-4684-0934-5_37.

[75] H. Salmang, H. Scholze, R. Telle, eds., Sintern, in: Keramik, Springer, Berlin, Heidelberg, 2007: pp. 313–380. https://doi.org/10.1007/978-3-540-49469-0_4.

[76] Z. Liu, X. Wang, M. Liu, J. Liu, Enhancing sinterability and electrochemical properties of $Ba(Zr_{0.1}Ce_{0.7}Y_{0.2})O_{3-\delta}$ proton conducting electrolyte for solid oxide fuel cells by addition of NiO, International Journal of Hydrogen Energy 43 (2018) 13501–13511. https://doi.org/10.1016/j.ijhydene.2018.05.089.

[77] Y. Huang, R. Merkle, J. Maier, Effects of NiO addition on sintering and proton uptake of $Ba(Zr,Ce,Y)O_{3-\delta}$, Journal of Materials Chemistry A 9 (2021) 14775–14785. https://doi.org/10.1039/D1TA02555D.

[78] S. Ricote, N. Bonanos, Enhanced sintering and conductivity study of cobalt or nickel doped solid solution of barium cerate and zirconate, Solid State Ionics 181 (2010) 694–700. https://doi.org/10.1016/j.ssi.2010.04.007.

[79] R.M. German, P. Suri, S.J. Park, Review: liquid phase sintering, J Mater Sci 44 (2009) 1–39. https://doi.org/10.1007/s10853-008-3008-0.

[80] D.J. Green, O. Guillon, J. Rödel, Constrained sintering: A delicate balance of scales, Journal of the European Ceramic Society 28 (2008) 1451–1466. https://doi.org/10.1016/j.jeurceramsoc.2007.12.012.

[81] D.J. Green, An Introduction to the Mechanical Properties of Ceramics, 1st ed., Cambridge University Press, 1998. https://doi.org/10.1017/CBO9780511623103.

[82] M. Choi, J. Paik, D. Kim, D. Woo, J. Lee, S.J. Kim, J. Lee, W. Lee, Exceptionally high performance of protonic ceramic fuel cells with stoichiometric electrolytes, Energy Environ. Sci. 14 (2021) 6476–6483. https://doi.org/10.1039/D1EE01497H.

[83] O. Guillon, Constrained sintering of ceramic materials, (2011). https://tubiblio.ulb.tu-darmstadt.de/57683/ (accessed June 21, 2023).

[84] W.D. Kingery, H.K. Bowen, D.R. Uhlmann, Introduction to Ceramics, Wiley, 1976.

[85] J.H. Flynn, L.A. Wall, General treatment of the thermogravimetry of polymers, J. RES. NATL. BUR. STAN. SECT. A. 70A (1966) 487. https://doi.org/10.6028/jres.070A.043.

[86] T. Ozawa, A New Method of Analyzing Thermogravimetric Data, Bulletin of the Chemical Society of Japan 38 (1965) 1881–1886. https://doi.org/10.1246/bcsj.38.1881.

[87] C.D. Doyle, Estimating isothermal life from thermogravimetric data, Journal of Applied Polymer Science 6 (1962) 639–642. https://doi.org/10.1002/app.1962.070062406.

[88] DIN EN ISO 13383-1:2016-11, Hochleistungskeramik_- Mikrostrukturelle Charakterisierung_- Teil_1: Bestimmung der Korngröße und der Korngrößenverteilung (ISO_13383-1:2012); Deutsche Fassung EN_ISO_13383-1:2016, Beuth Verlag GmbH, n.d. https://doi.org/10.31030/2482451.

[89] 2-Säulen Laborpressen manuell - P/O/WEBER Laborpresstechnik, (n.d.). https://t1p.de/s4qri (accessed June 16, 2024).

[90] HUBERLAB, Pasteur Pipetten aus PE | Transfer- und Pasteurpipetten | Pipettieren | Liquid Handling | Laborbedarf & Laborgeräte | Sortiment | HUBERLAB., (n.d.). https://t1p.de/mzj55 (accessed August 1, 2024).

[91] Y. Huang, Proton conducting electrolytes for ceramic fuel cells, (2020). https://doi.org/10.18419/OPUS-11110.

[92] W. Deibert, Entwicklung von geträgerten protonenleitenden Dünnschichtmembranen für die Wasserstoffabtrennung, Forschungszentrum Jülich GmbH, Zentralbibliothek, 2015.

[93] S. Bhattacharjee, M.K. Paria, H.S. Maiti, Polyvinyl butyral as a dispersant for barium titanate in a non-aqueous suspension, J Mater Sci 28 (1993) 6490–6495. https://doi.org/10.1007/BF01352219.

[94] P. Sachnik, S.E. Hoque, W. Volk, Burr-free cutting edges by notch-shear cutting, Journal of Materials Processing Technology 249 (2017) 229–245. https://doi.org/10.1016/j.jmatprotec.2017.06.003.

[95] R. Mücke, Sinterung von Zirkoniumdioxid-Elektrolyten im Mehrlagenverbund der oxidkeramischen Brennstoffzelle (SOFC), Forschungszentrum Zentralbibliothek, Jülich, 2008.

[96] Butvar® B-98 | TDS | Eastman Chemical Company, (n.d.). https://productcatalog.eastman.com/tds/ProdDatasheet.aspx?product=71095422 (accessed December 12, 2024).

[97] A.K. Dhaliwal, J.N. Hay, The characterization of polyvinyl butyral by thermal analysis, Thermochimica Acta 391 (2002) 245–255. https://doi.org/10.1016/S0040-6031(02)00187-9.

[98] M. Cavazzuti, Design of Experiments, in: M. Cavazzuti (Ed.), Optimization Methods: From Theory to Design Scientific and Technological Aspects in Mechanics, Springer, Berlin, Heidelberg, 2013: pp. 13–42. https://doi.org/10.1007/978-3-642-31187-1_2.

[99] G. Abbas, R. Raza, M. Ashfaq, M.A. Chaudhry, A. Khan, I. Ahmad, B. Zhu, Electrochemical study of nanostructured electrode for low-temperature solid oxide fuel cell (LTSOFC), International Journal of Energy Research 38 (2014) 518–523. https://doi.org/10.1002/er.3090.

[100] S. Pirou, Q. Wang, P. Khajavi, X. Georgolamprou, S. Ricote, M. Chen, R. Kiebach, Planar proton-conducting ceramic cells for hydrogen extraction: Mechanical properties, electrochemical performance and up-scaling, International Journal of Hydrogen Energy 47 (2022) 6745–6754. https://doi.org/10.1016/j.ijhydene.2021.12.041.

[101] J. Schindelin, I. Arganda-Carreras, E. Frise, V. Kaynig, M. Longair, T. Pietzsch, S. Preibisch, C. Rueden, S. Saalfeld, B. Schmid, J.-Y. Tinevez, D.J. White, V. Hartenstein, K. Eliceiri, P. Tomancak, A. Cardona, Fiji: an open-source platform for biological-image analysis, Nat Methods 9 (2012) 676–682. https://doi.org/10.1038/nmeth.2019.

[102] ICSC 0179 - METHYL ETHYL KETONE, (n.d.). https://www.ilo.org/dyn/icsc/showcard.display?p_version=2&p_card_id=0179 (accessed August 11, 2022).

[103] PubChem, Ethanol, (n.d.). https://pubchem.ncbi.nlm.nih.gov/compound/702 (accessed August 11, 2022).

[104] E. Karaoglu, H. Deligoz, H. Sözeri, A. Baykal, M. Toprak, Hydrothermal Synthesis and Characterization of PEG-Mn_3O_4 Nanocomposite, Nano-Micro Letters 3 (2011) 25–33. https://doi.org/10.5101/nml.v3i1.p25-33.

[105] B. Wang, L. Bi, X.S. Zhao, Exploring the role of NiO as a sintering aid in $BaZr_{0.1}Ce_{0.7}Y_{0.2}O_{3-\delta}$ electrolyte for proton-conducting solid oxide fuel cells, Journal of Power Sources 399 (2018) 207–214. https://doi.org/10.1016/j.jpowsour.2018.07.087.

[106] M. Chen, M. Zhou, Z. Liu, J. Liu, A comparative investigation on protonic ceramic fuel cell electrolytes $BaZr_{0.8}Y_{0.2}O_{3-\delta}$ and $BaZr_{0.1}Ce_{0.7}Y_{0.2}O_{3-\delta}$ with NiO as sintering aid, Ceramics International 48 (2022) 17208–17216. https://doi.org/10.1016/j.ceramint.2022.02.278.

[107] F. Temko, Kirigami: The Creative Art of Paper Cutting, Platt & Munk, 1962.

[108] R. de Oro Calderon, C. Gierl-Mayer, H. Danninger, Fundamentals of Sintering: Liquid Phase Sintering, in: F.G. Caballero (Ed.), Encyclopedia of Materials: Metals and Alloys, Elsevier, Oxford, 2022: pp. 481–492. https://doi.org/10.1016/B978-0-12-819726-4.00127-7.

[109] T. Frueh, I.O. Ozer, S.F. Poterala, H. Lee, E.R. Kupp, C. Compson, J. Atria, G.L. Messing, A critique of master sintering curve analysis, Journal of the European Ceramic Society 38 (2018) 1030–1037. https://doi.org/10.1016/j.jeurceramsoc.2017.12.025.

[110] A. Jakobsson, D. Sichen, S. Seetharama, Thermodynamic study of the NiO-MgO System in the temperature range 1073 to 1473 K by a galvanic cell technique, Metall Trans B 24 (1993) 1023–1030. https://doi.org/10.1007/BF02660993.

[111] V. Prostakova, J. Chen, E. Jak, S. Decterov, Experimental study and thermodynamic optimization of the CaO–NiO, MgO–NiO and NiO–SiO_2 systems, Calphad 37 (2012) 1–10. https://doi.org/10.1016/j.calphad.2011.12.009.

12 Supplementary Information

Standard Operating Procedure

The following additions supplement the explanations provided in this thesis and should be applied when preparing half-cells using the optimized procedure.

Required preparation time: 3 weeks

1. Material Preparation

- **Powders**: Use 23K1 BZCY-721 (Marion Technologies) (or similar) and Vogler NiO. Refer to Table 4-1 for particle size and specific surface area.
- **Storage**: Ensure powders are dry and free of contaminants before use.
- Prepare electrolyte powder by adding 0.5 wt.-% NiO to the base 23K1, homogenization as detailed in Chapter 4.1.

2. Slurry Preparation

- **Electrolyte Slurry:**
  - Composition: Ethanol-based (see Table 12-1 and Chapter 5.4-5.5).
  - Use the Thinky mixer for homogeneous dispersion (Chapter 5.1).
    - For safety reasons, it is very important to let the container cool down before proceeding with the weighing process. During the mixing step, the high velocity and differential movement of the milling balls will increase the slurry temperature significantly. This will lead to the evaporation of the solvent which in turn increases the pressure inside the container. Opening the container before fully cooling down can result in a “splashing” of NiO containing slurry across the fume hood up to face height posing a very significant safety hazard.
  - Measure viscosity to ensure consistency (see Chapter 5.6.3)
- **Substrate Slurries**:
  - Composition: see Table 12-1 (and Chapter 5.1).
  - In contrast to the electrolyte slurry, ceramic powders, dispersant and solvent are added and first homogenized on the Turbular mixer. 3G8 (1 h), PVB, and PEG 400 (1 h) are added and homogenized individually.
  - Use the Turbular mixer for improved dissolution of PVB. PVB dissolution can require up to 7 h. Process can be stopped at night and started in the next morning for ~1h.
  - Prepare two substrate slurries for bilayer casting and one for the support layer.

Table 12-1: Final composition of slurries for bilayer tape casting using the JuCast.

	Final Substrate Slurry Composition	**Final Electrolyte Slurry Composition**	
	Wt.-%		
BZCY-721	26.21	BZCY-721 + 0.5 wt.-% NiO	64.79
NiO	39.31		
Ethanol	8.27	24.85	
MEK	16.05	N/A	
Nuosperse FX9086	0.98	1.30	
PVB 98	4.59	4.54	
3G8 Ester	2.29	2.27	
PEG-400	2.29	2.27	

3. Tape Casting

- **Caster**: Operate the JuCast tape caster to match final conditions. Avoid the Micro-tape caster to prevent discrepancies in shear and drying conditions.
- **Parameters**: Set casting parameters for optimal layer thickness. The current maximum blade gap was found to be 1200 µm for this viscosity.
- **Drying Times**:
  - Allow the electrolyte layer to dry for 4 hours before applying the second layer.
  - Cast the single-layer substrate tape separately.

4. Handling and Cutting

- **Tape Removal**:
  - Detach tapes in sections. Handle flat to prevent deformation.
  - Cover with foil to avoid contamination.
- **Pre-sectioning**: Cut tapes manually into 7 × 7 cm^2 squares before lamination.

5. Lamination and Final Shaping

- **Lamination**: Use a hydraulic press to laminate layers under uniform pressure. Allow tapes to cool before further handling. (Settings see Chapter 6.4.4)
- **Final Cutting**: Shape tapes into 3.25 × 6.5 cm^2 rectangles using the Silhouette Cameo 4 cutter. Settings to be adjusted for each tape thickness.

6. Stacking and Assembly

- Use 15 × 15 cm^2 Al_2O_3 crucibles, place ZrO_2 plate inside.
- **Stacking**: Place samples electrolyte-side-to-electrolyte-side on ZrO_2 plates (supplier Nikatto).
- **Outcome**: This method increases the success rate of functional cells to ~60 % - 90 % (depending on size).

7. Sintering Process

- **Setup**:
    - Position a cover close to the samples to ensure uniform temperature distribution during sintering.
    - Avoid fully closing the crucible to allow binder burnout gases to escape, minimizing atmospheric effects on material sintering behavior.
    - The procedure is as follows: ramp up at 0.5 K/min to 900 °C, then 2 K/min to 1550 °C, with a three-hour holding period, followed by cooling at 2 K/min.
- **Controlled Cooling**:
    - Ensure a controlled cooling rate to prevent thermal stress and maintain material integrity

8. Quality Control

- Preparation of cross-sections: best results for the cross-section preparation are achieved when using samples embedded in Epoxy Resin, using water for the grinding steps up to sanding paper grade 2400 and switching to alcohol-based lubricants for the finer steps as well as polishing. Due to the brittleness of low porosity samples, it is advised to grind the individual samples by hand during the fine grinding steps to avoid scratching other samples when breakouts occur.

Comparison of XRD Spectra for different BZCY Powder Batches

Purchased BZCY-721 Batch 22K2

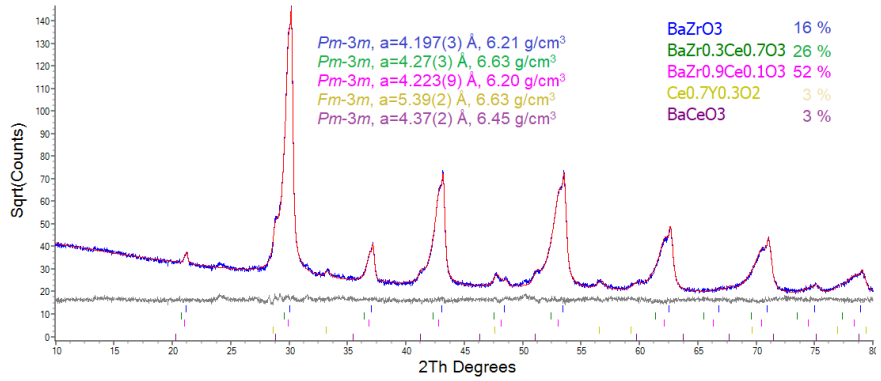

Purchased BZCY-721 Batch 22K4

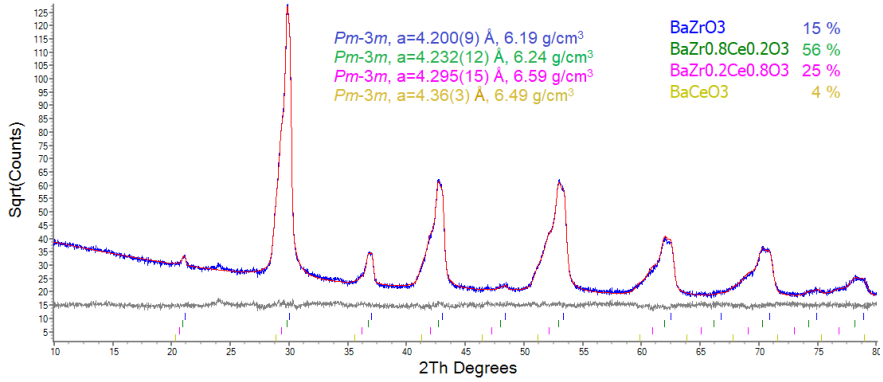

In-house (Batch B6, calcined 1300 °C)

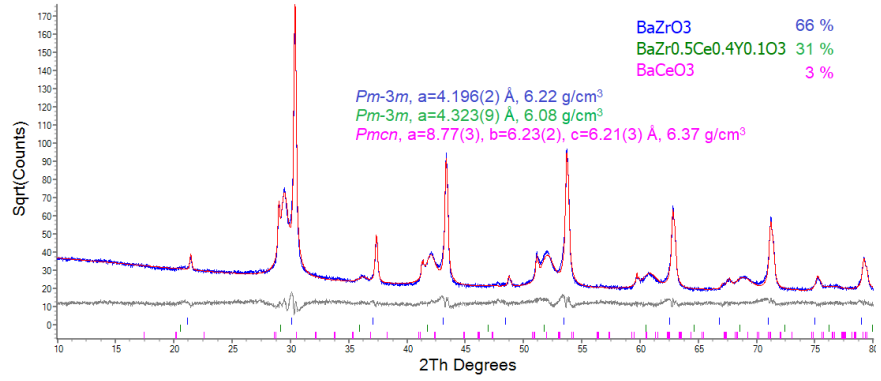

Figure 12-1: Rietveld analysis of different purchased powder batches and in-house synthesized BZCY. Phase compositions only to be understood as potential due to very large ambiguities.

Sedimentation Experiments

The dispersions were prepared by mixing the abovementioned dispersants with the MEK/Ethanol mixture in 50-ml PE bottles with 15 ml of 3 mm yttrium-stabilized ZrO_2 milling balls. First, the mixtures were manually homogenized to ensure the dispersant was dispersed in the solvent. Afterward, the powders were added. The PE bottles were covered with sealing tape to limit solvent evaporation. The mixtures were homogenized using the tumble mixer (4 h, 67 rpm). To ensure the comparability of the settlement results, particle size measurements were carried out for each sample. For each of the mixtures, 5 ml was taken and transferred into DIN standardized measuring cylinders (5 ml, 10 ml, 25 ml). Volume differences were due to availability in the laboratory. The reference sample Nr. 1 and the mixtures with Nuosperse FX 9086 were transferred to 5 ml measuring cylinders, BYK 220S mixtures to 10 ml cylinders, and all other samples to 25 ml cylinders. The containers were sealed using sealant tape to limit the evaporation of the solvent.

Table 12-2: Additional information on the sedimentation compositions

ID	Name	Powder	Dispersant	Dispers. amount	MEK/ Ethanol	Powder	Actual dispers.	Target dispers.	D10	D50	D90
				g	g	g					
1	22K4-Reference	22K4	Nuosperse FX 9086	0,00	19,95	10,00	0,0%	0,0%	0,387	0,726	1,611
2	22K4-Nuos-0.5	22K4	Nuosperse FX 9086	0,07	20,00	10,00	0,7%	0,5%	0,387	0,758	1,716
3	22K4-Nuos-1.0	22K4	Nuosperse FX 9086	0,10	20,00	10,35	1,0%	1,0%	0,339	0,666	1,686
4	22K4-Nuos-1.5	22K4	Nuosperse FX 9086	0,15	20,01	9,97	1,5%	1,5%	0,322	0,632	1,506
5	22K4-Nuos-2.0	22K4	Nuosperse FX 9086	0,20	20,04	10,00	2,0%	2,0%	0,324	0,650	1,634
6	22K4-Nuos-2.5	22K4	Nuosperse FX 9086	0,25	19,95	9,98	2,5%	2,5%	0,334	0,649	1,506
7	22K4-BYK-0.5	22K4	BYK 220S	0,05	19,90	9,86	0,5%	0,5%	0,363	0,690	1,589
8	22K4-BYK-1.0	22K4	BYK 220S	0,10	20,31	10,17	1,0%	1,0%	0,363	0,700	1,713
9	22K4-BYK-1.5	22K4	BYK 220S	0,15	20,02	9,98	1,5%	1,5%	0,351	0,685	1,651
10	22K4-BYK-2.0	22K4	BYK 220S	0,19	20,00	9,98	2,0%	2,0%	0,350	0,679	1,615
11	22K4-BYK-2.5	22K4	BYK 220S	0,27	20,22	10,08	2,7%	2,5%	0,381	0,716	1,724
12	175-El-Nuos-1.5	BZCY 625 20 175 + 0.5 wt.-% NiO	Nuosperse FX 9086	0,09	12,63	6,26	1,5%	1,5%	0,469	1,366	3,197
13	22K2-El-Nuos-1.5	22K2 + 0,5 wt.-% NiO	Nuosperse FX 9086	0,09	12,09	6,01	1,5%	1,5%	0,379	0,854	2,202
14	MT-Ki-Nuos-1.5	MT Kindelmann as received	Nuosperse FX 9086	0,09	11,10	5,78	1,5%	1,5%	0,277	0,632	1,739
15	22K4-El-Nuos-1.5	22K4 + 0,5 wt.-% NiO	Nuosperse FX 9086	0,09	12,29	6,10	1,5%	1,5%	0,290	0,597	1,672

Table 12-3: Description of supernatant liquid after seven days of rest.

ID	Sample name	Appearance of supernatant liquid
1	22K4-Reference	Clear
2	22K4-Nuos-0.5	Cloudy
3	22K4-Nuos-1.0	Cloudy, gradual transition between 2 ml and 3 ml
4	22K4-Nuos-1.5	Cloudy
5	22K4-Nuos-2.0	Cloudy
6	22K4-Nuos-2.5	Cloudy
7	22K4-BYK-0.5	Soft transition, three layers with separation lines at 1.4 ml and 2.8 ml
8	22K4-BYK-1.0	Cloudy
9	22K4-BYK-1.5	Cloudy
10	22K4-BYK-2.0	Cloudy
11	22K4-BYK-2.5	Very clear separation line, very clear
12	175-El-Nuos-1.5	Cloudy
13	22K2-El-Nuos-1.5	Cloudy
14	MT-Ki-Nuos-1.5	Cloudy
15	22K4-El-Nuos-1.5	Cloudy

Comparison of Viscosity of BZCY vs. YSZ based Substrate Slurries

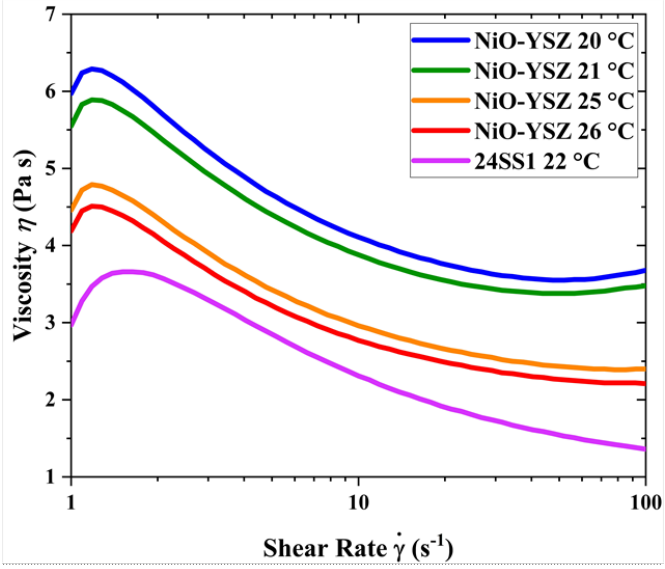

Figure 12-2: Viscosity measurements of the electrode slurry 24SS1 in comparison with the standard SOC NiO-YSZ slurries at different temperatures. It can be seen that the overall viscosity of the slurry is less viscous for the BZCY-721. However, the maximum of the curve is shifted to higher shear rates. This means that it becomes closer to the range of tape casting. Shear thickening behavior in the shear rate range of tape casting would be very detrimental and causes streaks and defects in the tape. Therefore, this behavior needs to be avoided through careful slurry conditioning.

Additional Information on Lamination Parameter Study

Table 12-4 presents the parameter combinations of each lamination run. The order of the runs was randomized.

Table 12-4: Parameter combinations for each lamination run.

Duration in s	Temperature in °C	Pressure in MPa	Allowed compression of initial thickness
60	90	8	-5 %
130	85	6	-10 %
60	80	8	-15 %
200	90	4	-5 %
200	80	8	-5 %
200	80	4	-15 %
200	90	8	-15 %
130	85	6	-10 %
60	90	4	-15 %
60	80	4	-5 %

Measurements of Single Layers in z-Direction

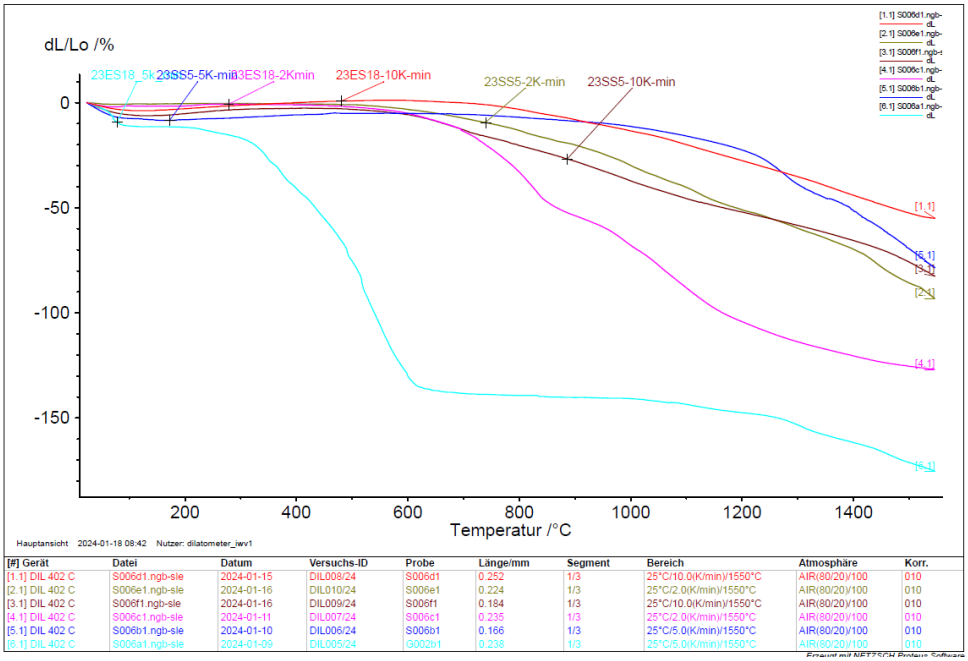

Figure 12-3: Measurement of single layer tapes to determine shrinkage in z-direction. Samples are severely bent and/or broken during the measurement. In contrast to the Kirigami samples, no trend is discernable.

Microstructure of Bilayer after Burnout

Figure 12-4 shows the microstructure of a bilayer after the burnout process. Due to the fragility of the sample and its high porosity, significant influence from the cross-section preparation—through embedding and polishing—was anticipated. The micrograph clearly reveals large BZCY agglomerates within the substrate, along with a zone of increased porosity near the electrolyte-electrode interface. However, this localized porosity did not have a significant impact on the overall porosity of the substrate after sintering.

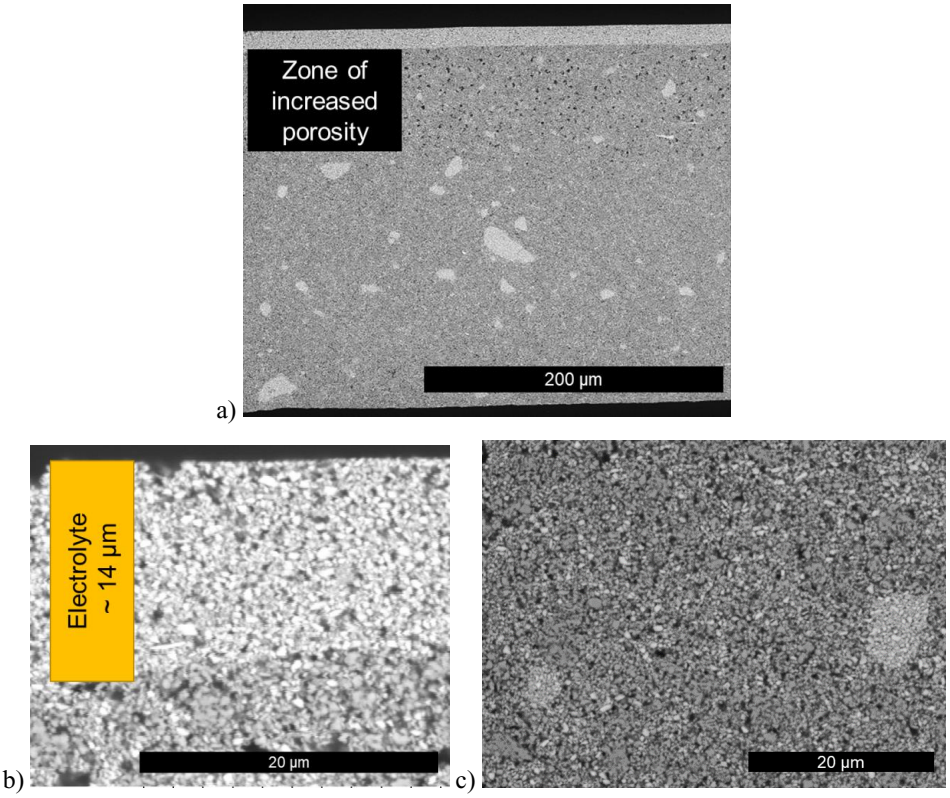

Figure 12-4: Microstructure of sample after binder burnout (900 °C), JuCast bilayer tape 23-ES-17-SS-4; a) entire cross-section with large agglomerates and zone of increased porosity at the electrolyte interface region, b) electrolyte, c) electrode layer with agglomerates. Thresholding issue: density of electrolyte between 53 % and 90 % => unreliable, after sintering 99 %.

Additional TEM Micrographs

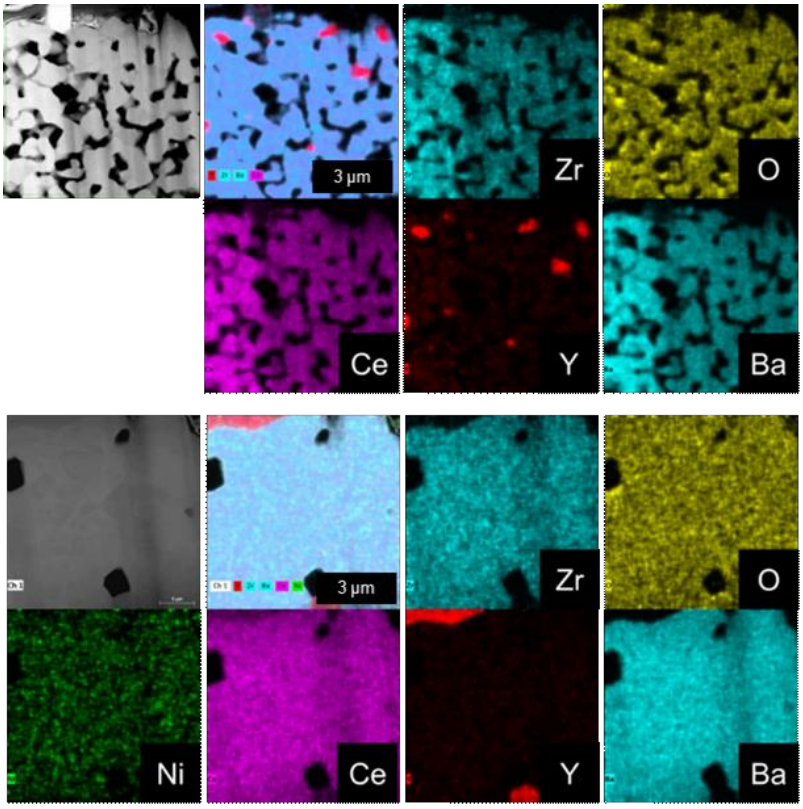

Figure 12-5: EDX measurement of top) BZCY-721 Pellets (22K4 without NiO), bottom) with 0.5 wt.-% NiO (Philipps University Marburg). Although not found in the XRD analysis, the EDX clearly shows the existence of a Ce-Y-Oxide phase.

The addition of nickel oxide is expected to create a liquid phase, introducing additional sintering mechanisms such as particle rearrangement. Figure 12-6 presents analysis results from Philipps-University Marburg, showing clear segregation of nickel and yttrium at the grain boundaries. This could be an indication of the formation of the transient liquid phase.

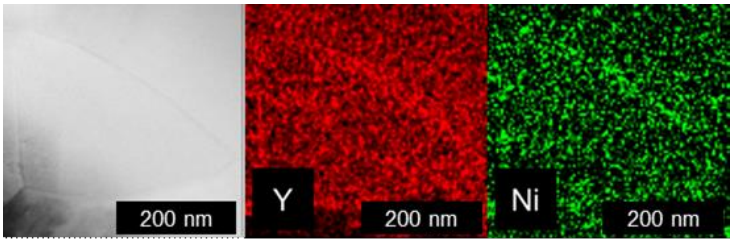

Figure 12-6: Grain in a pellet of BZCY-721 with NiO as sintering aid, with traces of nickel and yttrium along the grain boundary suggesting the formation of a secondary phase, possibly remnants of the transient liquid phase which assists in sintering.

Usage of Symmetrical Assemblies

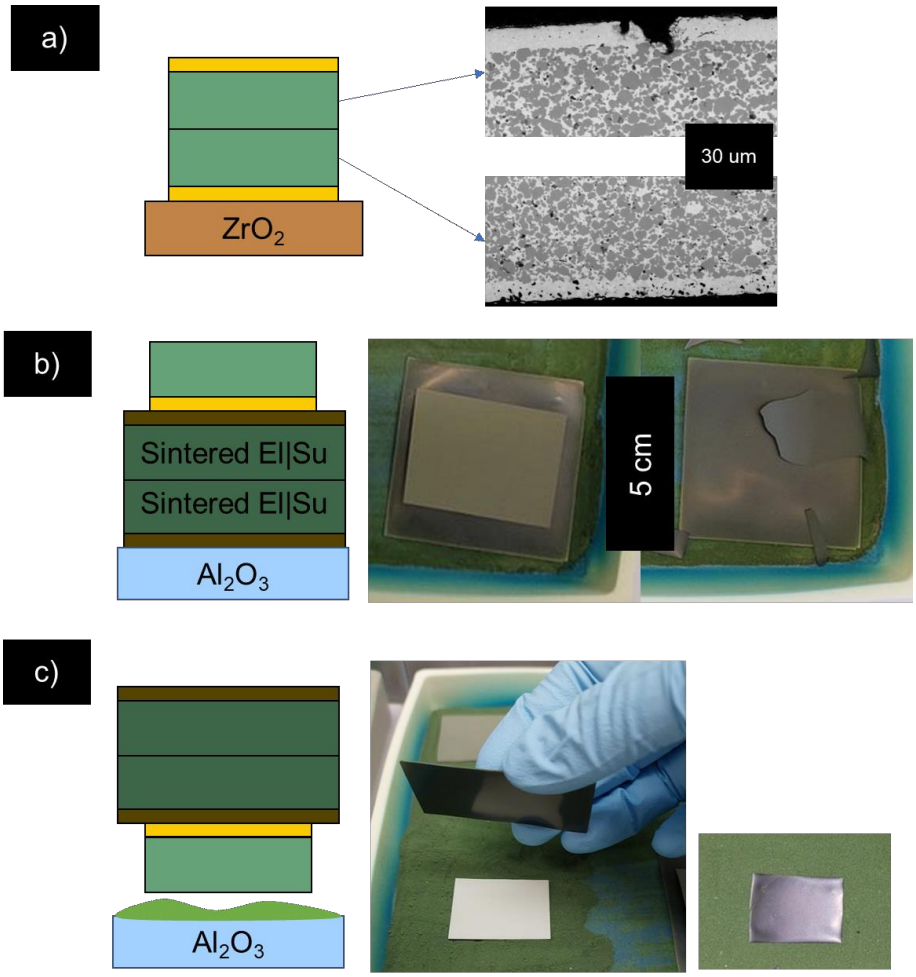

Figure 12-7: Sintered(El|Su+Su|El) samples: a) sintered on ZrO_2, influence of contact to setter plate or air on electrolyte microstructure, in contact with setter plate densification is inhibited by constrained sintering, on the top side the electrolyte densified well but experienced cracking; b) usage of symmetric assembly as setter plate failed; c) usage of symmetric assembly as weight showed promise.

Additional Considerations BZCY/NiO Powder Bed

a) 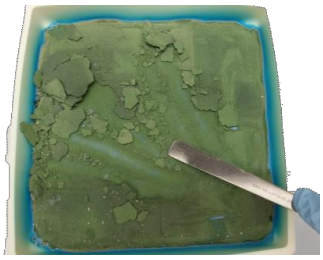 b) 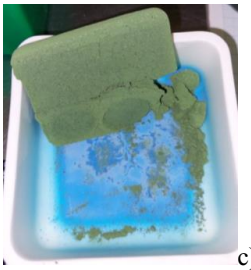 c) 

Figure 12-8: Consolidation of BZCY/NiO sacrificial powder after heat-treatment. Grinding and sieving this powder for reuse is a significant safety hazard and most likely unacceptable for use in industry. a) standard procedure after every furnace run; b) fully consolidated powder bed after compaction prior sintering to even out the surface: c) limited usability of the powder bed. Coarse powder has different results then fine powder, requiring a milling and sieving step to reuse the powder again.

Band / Volume 705
Drivers of spatiotemporal variability of European terrestrial ecosystem processes
C. Poppe Téran (2026), 254 pp
ISBN: 978-3-95806-905-3

Band / Volume 706
Characterization of Nitrogen Reduction Reaction Catalysts for the electrochemical Ammonia Synthesis
D. Sachse (2026), xi, 235, 6 pp
ISBN: 978-3-95806-907-7

Band / Volume 707
Autonomous Image Analysis to Accelerate the Discovery and Integration of Energy Materials
A. Colliard Granero (2026), xiv, 156 pp
ISBN: 978-3-95806-910-7 (Print)
ISBN: 978-3-95806-911-4 (E-Book)

Band / Volume 708
Effect of Soil Mechanical Properties, Root Tip Geometry, and Mucilage on Penetration Restistance to Root Growth
R. K. Janakiram (2026), xxviii, 98 pp
ISBN: 978-3-95806-914-5 (Print)
ISBN: 978-3-95806-915-2 (E-Book)

Band / Volume 709
European Energy Transition – Germany in the Heart of Europe
T. Klütz, P. Dunkel, T. Busch, J. Linssen, D. Stolten (2026), V, 54 pp
ISBN: 978-3-95806-916-9 (Print)
ISBN: 978-3-95806-917-6 (E-Book)

Band / Volume 710
Development of High-Efficiency Perovskite/Silicon Tandem Solar Cells
Q. Yang (2026), 264 pp
ISBN: 978-3-95806-920-6 (Print)
ISBN: 978-3-95806-921-3 (E-Book)

Band / Volume 711
No-Regret-Maßnahmen der integrierten Netzplanung mit Fokus auf Wasserstoff
T. G. Busch (2026), xx, 325 pp
ISBN: 978-3-95806-922-0 (Print)
ISBN: 978-3-95806-923-7 (E-Book)

Band / Volume 712
Data-Driven Modeling for Digital Representations in Energy Systems
M. C. Zimmer (2026), xv, 166 pp
ISBN: 978-3-95806-926-8 (Print)
ISBN: 978-3-95806-927-5 (E-Book)

Band / Volume 713
Towards integrated PV applications: development of lightweight silicon heterojunction solar modules and their damp-heat and UV stability
K. Zhang (2026), iii, 179 pp
ISBN: 978-3-95806-928-2 (Print)
ISBN: 978-3-95806-929-9 (E-Book)

Band / Volume 714
Zinc-Based Catalysts for the Electrochemical CO_2 Reduction
I. Stamatelos (2026), vii, 136 pp
ISBN: 978-3-95806-932-9 (Print)
ISBN: 978-3-95806-933-6 (E-Book)

Band / Volume 715
Charakterisierung innovativer keramischer Materialien für Elektrolysezellen
L. P. Wehner (2026), xiv, 110 pp
ISBN: 978-3-95806-936-7 (Print)
ISBN: 978-3-95806-937-4 (E-Book)

Band / Volume 716
Process Optimization and Scale-Up for $Ba(Zr,Ce,Y)O_{3-\delta}$-Based Proton-Conducting Electrolysis Half-Cells
L.-A. Schäfer (2026), iv, 141 pp
ISBN: 978-3-95806-940-4 (Print)
ISBN: 978-3-95806-941-1 (E-Book)

Weitere ***Schriften des Verlags im Forschungszentrum Jülich*** unter
http://wwwzb1.fz-juelich.de/verlagextern1/index.asp

Energie & Umwelt / Energy & Environment
Band / Volume 716
ISBN 978-3-95806-941-1

Mitglied der Helmholtz-Gemeinschaft

JÜLICH
Forschungszentrum